

2005

# Myocardial Perfusion Imaging With Rb-82 PET

George Nittil Francis  
*Virginia Commonwealth University*

Follow this and additional works at: <http://scholarscompass.vcu.edu/etd>

 Part of the [Biomedical Engineering and Bioengineering Commons](#)

© The Author

---

Downloaded from

<http://scholarscompass.vcu.edu/etd/717>

This Thesis is brought to you for free and open access by the Graduate School at VCU Scholars Compass. It has been accepted for inclusion in Theses and Dissertations by an authorized administrator of VCU Scholars Compass. For more information, please contact [libcompass@vcu.edu](mailto:libcompass@vcu.edu).

© George Nittil Francis

All Rights Reserved

MYOCARDIAL PERFUSION IMAGING WITH RB-82 PET

A Thesis submitted in partial fulfillment of the requirements for the degree of Master of Science at Virginia Commonwealth University.

By

GEORGE NITTIL FRANCIS  
Bachelor of Arts in Computer Science, 2003  
Rutgers, The State University of New Jersey, Newark, NJ

Director: KAREN A. KURDZIEL, MD  
ASSISTANT PROFESSOR, DEPARTMENT OF RADIOLOGY  
MEDICAL DIRECTOR, VCUMC MOLECULAR IMAGING CENTER

Virginia Commonwealth University  
Richmond, Virginia  
December 2005

## **Acknowledgement**

I want to express my sincere gratitude to my thesis director, Dr. Karen A. Kurdziel, for her steadfast guidance and, dissemination of knowledge and expertise, during the course of this project.

The completion of this project was due in large part to assistance and contributions from my thesis co-director, Dr. Joseph D. Kalen and the entire staff of Department of Nuclear Medicine. My special acknowledgements to Wendy Bullock (PACS Application Specialist) and James McCumiskey (Lead PET/CT Technologist) for their patience and technical assistance throughout this project.

I would also like to thank my committee members from Department of Biomedical Engineering, including Dr. Ding-Yu Fei for keeping me on track to graduate and Dr. Martin L. Lenhardt for his constant encouragement.

I wish to sincerely thank my parents who provided much needed encouragement, support and enthusiasm. They have made countless sacrifices during the past two years so that I could realize this dream and without their support it would not have been possible.

This project was funded by Bracco Diagnostics Inc, Princeton, NJ. Dr. Karen A. Kurdziel was the principal investigator of the project. I want to thank Bracco Diagnostics and Dr. Kurdziel for the financial assistance provided.

Most of all, I would like to thank God for giving me the patience, wisdom and the perseverance to complete this project.

## Table of Contents

	Page
Acknowledgements.....	ii
List of Tables .....	ix
List of Figures .....	x
Abstract.....	xiii
Chapter	
1 INTRODUCTION .....	1
1.1 Myocardial Perfusion Imaging (MPI) .....	1
1.2 PET vs. SPECT .....	5
1.3 Rubidium-82 PET for Myocardial Perfusion Imaging.....	9
1.4 Assessment of Myocardial Function .....	11
1.5 Problem Statement .....	11
1.6 Scope of the Thesis.....	13
2 POSITRON EMISSION TOMOGRAPHY (PET) BACKGROUND.....	15
2.1 Positron Physics .....	16
2.2 Positron Annihilation .....	16
2.3 Coincidence Detection .....	17
2.3.1 Photoelectric Effect .....	20
2.3.2 Compton Scattering.....	21

2.3.3 Event Types in Coincidence Detection .....	21
2.4 PET Detector and Scanner Designs.....	23
2.4.1 Block Detectors .....	23
2.4.2 Dedicated PET Systems .....	25
2.5 Data Acquisition for PET .....	25
2.5.1 Two-Dimensional Data Acquisition.....	25
2.5.2 Three-Dimensional Data Acquisition.....	27
2.6 Data Corrections and Quantitative Aspects of PET .....	28
2.6.1 Scatter .....	28
2.6.2 Correction for Scattered Radiation.....	29
2.6.3 Attenuation .....	30
2.6.4 Attenuation Correction.....	30
2.6.5 Dead Time .....	31
2.6.6 Dead Time Corrections .....	31
2.6.7 Noise.....	32
2.6.8 Spatial Resolution.....	33
2.7 Image Reconstruction.....	33
2.8 SPECT .....	36
2.9 PET vs. SPECT Revisited .....	38

3	OPTIMAL GATED IMAGE ACQUISITION START TIME FOR	
	<sup>82</sup> Rb PET .....	43
3.1	Introduction .....	43
3.2	Methods and Materials .....	44
3.2.1	GE Discovery LS PET/CT scanner .....	44
3.2.2	Cardiogen-82 ( <sup>82</sup> Rb Generator).....	47
3.2.3	<sup>82</sup> Rb PET Patient Data Acquisition Procedure .....	49
3.2.4	<sup>82</sup> Rb PET Patient Data Processing.....	50
3.2.4.1	Image Reconstruction.....	50
3.2.4.2	Quantitative Perfusion SPECT (QPS).....	52
3.2.4.3	Measured Time Activity Curves .....	54
3.2.4.4	Infusion Time Activity Curves.....	61
3.2.5	<sup>82</sup> Rb PET Patient Data Analysis.....	62
3.2.6	Statistical Analysis .....	63
3.3	Results .....	64
3.3.1	Overall Correlation of Infusion Time and Splitting Time.....	64
3.3.2	Hemodynamic Findings .....	65
3.4	Discussion .....	66

4	COMPARISON OF $^{82}\text{Rb}$ GATED PET LVEF USING QGS WITH $^{99\text{m}}\text{Tc}$ FIRST PASS RADIONUCLIDE ANGIOGRAPHY LVEF .....	67
4.1	Introduction .....	67
4.2	Methods and Materials .....	68
4.2.1	Patient Studies .....	68
4.2.2	First Pass Radionuclide Angiography (FPRNA).....	68
4.2.3	Data Analysis .....	71
4.2.3.1	First Pass Data Processing.....	71
4.2.3.2	Quantitative Gated SPECT (QGS).....	72
4.2.4	Statistical Analysis .....	73
4.3	Results .....	74
4.3.1	Overall Correlation of QGS LVEF and FPRNA LVEF.....	74
4.3.2	Rest and Post-Stress QGS LVEF .....	75
4.3.3	Reproducibility of Measured Data .....	76
4.4	Discussion .....	78
4.5	Conclusion.....	79
5	DETERMINATION OF POST FILETERING PARAMETERS FOR ACCURATE DEFECT SIZE DETERMINATION IN A CARDIAC PHANTOM USING $^{99\text{m}}\text{Tc}$ , $^{18}\text{F}$ , AND $^{124}\text{I}$ .....	81
5.1	Introduction .....	81



5.2 Methods and Materials .....	82
5.2.1 Siemens E.CAM Dual-Head Variable Angle Gamma Camera System .....	83
5.2.2 Cardiac Static Phantom Study .....	84
5.2.2.1 SPECT Phantom Data Acquisition (Non-Gated) .....	86
5.2.2.2 PET Data Acquisition (Non-Gated) .....	88
5.2.3 Data Analysis .....	89
5.2.4 REGION_GROW Procedure in IDL .....	90
5.2.5 Maximum Pixel Value Threshold of an Image in IDL .....	91
5.2.6 Butterworth Filter .....	92
5.2.7 Statistical Analysis .....	92
5.3 Results .....	92
5.3.1 Relationship between SPECT and PET Measurements and Percent Maximum Pixel Threshold Values .....	95
5.4 Discussion .....	95
5.5 Conclusion .....	98
References .....	99
Appendices .....	106
A IDL Code to Sort DICOM PET Data, Extract Image Statistics and Write to an External Text File .....	106

B	Steps for First Pass Radionuclide Angiography Data Processing .....	111
C	Steps for Quantitative Gated SPECT (QGS 3.0) Data Analysis of $^{82}\text{Rb}$ Gated- PET Data for estimation of Left Ventricular Ejection Fraction.....	115
D	IDL Code to Estimate Percent Defect Size of Cardiac Phantom PET Data ..	117
Vita.....		122

## List of Tables

	Page
Table 2.1: Properties of commonly used PET radioisotopes.....	16
Table 3.1: Correlation of various parameters in infusion time and splitting time. ....	64
Table 3.2: Hemodynamic findings.....	65
Table 4.1: Comparison of LVEF measured from first pass radionuclide angiography (FPRNA) and quantitative electrocardiographic-gated SPECT (QGS).....	75
Table 4.2: Reproducibility of data measured from first pass radionuclide angiography (FPRNA) and quantitative electrocardiographic-gated SPECT (QGS).....	76
Table 5.1: Comparison of $^{82}\text{Rb}$ Patient Defect Size at 45% threshold before and after application of optimal filtering parameters.....	94
Table 5.2: Comparison of $^{124}\text{I}$ and $^{99\text{m}}\text{Tc}$ defect sizes at thresholds ranging from 30% to 75% after application of respective optimal filtering parameters.....	95

## List of Figures

	Page
Figure 1: Electron–positron annihilation. ....	17
Figure 2: Coincidence event detected in ring PET scanner .....	19
Figure 3: Variation of point source response function with position P in SPECT and in PET .....	20
Figure 4: Event types in coincidence detection .....	22
Figure 5: A block detector. ....	24
Figure 6: Multi-ring PET acquisition modes .....	26
Figure 7: Scattered Events .....	28
Figure 8: Left ventricular myocardium in short axis, vertical long axis and horizontal long axis views.....	38
Figure 9: Evidence of anterior wall ischemia on a SPECT <sup>99m</sup> Tc sestamibi study.....	40
Figure 10: Normal <sup>82</sup> Rb PET study images .....	41
Figure 11: GE PET/CT Scanner .....	45
Figure 12: Cardiogen-82 ( <sup>82</sup> Rb Generator).....	48
Figure 13: Dynamic PET data acquisition procedure description .....	51
Figure 14: Quantitative display output for the Cedars-Sinai Quantitative Perfusion SPECT program.....	53
Figure 15: Cardiac PET dynamic rest images with ROI.....	55

Figure 16: Cardiac PET dynamic stress images .....	55
Figure 17: Measured time activity curves – Patient A.....	57
Figure 18: Measured time activity curves – Patient B.....	58
Figure 19: Measured time activity curves – Patient C.....	59
Figure 20: Measured time activity curves – Patient D.....	60
Figure 21: Measured time activity curves – 1 <sup>st</sup> four minutes during vasodilator-induced stress.....	61
Figure 22: Infusion Time Activity Curves – Dynamic Rest and Dynamic Stress.....	62
Figure 23: Diastole and systole.....	69
Figure 24: Images from QGS of end-diastolic and end-systolic phases showing epicardial and endocardial borders of left ventricle .....	73
Figure 25: Correlation of rest FPRNA LVEF vs. rest QGS LVEF and rest FPRNA LVEF vs. stress QGS LVEF .....	74
Figure 26: Scatter plots of QGS and FPRNA data .....	77
Figure 27: Anterior and upper views of elliptical lung-spine body phantom .....	84
Figure 28: Cardiac defect insert.....	85
Figure 29: Siemens gamma camera, e.cam.....	87
Figure 30: Butterworth Cutoff vs. Defect size plot for <sup>124</sup> I.....	93
Figure 31: <sup>82</sup> Rb dynamic PET data before and after application of optimal filtering parameters .....	94

Figure 32: First Pass Radionuclide Angiography processing screenshot .....114

Figure 33: Screenshot of QGS analyzed results of gated  $^{82}\text{Rb}$  PET data .....116

# Abstract

## MYOCARDIAL PERFUSION IMAGING WITH RB-82 PET

By George N. Francis, MS

A Thesis submitted in partial fulfillment of the requirements for the degree of Master of Science at Virginia Commonwealth University.

Virginia Commonwealth University, 2005

Major Director: Karen A. Kurdziel, MD  
Assistant Professor, Department of Radiology  
Medical Director, VCUMC Molecular Imaging Center

Myocardial perfusion imaging (MPI) is an effective technique used to study the left ventricular ejection function (LVEF), myocardial perfusion, wall motion, and wall thickening. Positron emission tomography (PET) and single photon emission computed tomography (SPECT) are two modalities that can be used to quantify the left global and regional perfusion at rest and stress. While PET and SPECT rely on similar principles to produce images, important differences in instrumentation and experimental applications are dictated by inherent differences in their respective physics of radioactive decay. With a sensitivity > 90% in combination with a high specificity, PET is today the best available

nuclear imaging technique for the diagnosis of coronary artery disease (CAD). The short half-life of the perfusion tracers in combination with highly sophisticated hard- and software enables rapid PET studies with high patient throughput.

Rubidium-82 ( $^{82}\text{Rb}$ ) is a PET perfusion imaging agent that has a short half-life of 76 seconds which enables multiple sequential data acquisitions in a short duration of time. It also reduces the number of false-positive SPECT scans and artifacts from soft tissue attenuation due to the routine application of attenuation correction. However  $^{82}\text{Rb}$  PET imaging is under-utilized clinically due to difficulty optimizing the imaging parameters.

The major challenge of  $^{82}\text{Rb}$  imaging is determining when to begin the image acquisition post infusion, as imaging too early results in images with high background (low contrast), and imaging too late results in noisy images due to low count statistics.  $^{82}\text{Rb}$  rest/stress dynamic and gated data from 16 patients were available for analysis. The FWHM of the  $^{82}\text{Rb}$  infusion, LV cavity and LV myocardial uptake in time activity curves were generated and compared to isolate the dominant parameter in determining image quality. The measured and actual infusion-time correlated only at rest ( $r = 0.93$ ,  $P = 0.006$ ). Splitting-time at rest and stress correlated ( $r = 0.74$ ,  $P = 0.09$ ). But the study was not able to identify a single dominant parameter that would determine the image quality due to the unpredictable nature of hemodynamics during the vasodilatory induced cardiovascular stress.

First pass radionuclide angiography (FPRNA) is the gold standard for quantification of ejection fraction. We examined the quantification of the ejection function (LVEF) to determine whether the gated  $^{82}\text{Rb}$  PET data, using quantitative gated SPECT



(QGS), would accurately predict changes in the chamber volume and correlated the results with those obtained from FPRNA technique. There was a good correlation between the resting FPRNA data and resting gated  $^{82}\text{Rb}$  QGS data ( $r = 0.81$ ,  $P = 0.0005$ ) showing that this method can be applied to  $^{82}\text{Rb}$  PET.

$^{99\text{m}}\text{Tc}$  SPECT was considered the gold standard for this study, as it is the most widely used technique for myocardial perfusion imaging. The under-perfused area of the myocardium is defined as *defect*.  $^{99\text{m}}\text{Tc}$  agents,  $^{18}\text{F}$ -FDG, and  $^{82}\text{Rb}$  can all be used for cardiac imaging <sup>1-7</sup>. However, count rates, energy and camera differences can yield image differences that are independent of the actual biological distribution. We examined whether PET with an  $^{82}\text{Rb}$ -labeled tracer would provide information on defect size similar to that provided by  $^{99\text{m}}\text{Tc}$  SPECT, using a cardiac phantom in which the true defect size is known. Since  $^{82}\text{Rb}$  has such a short half-life (76 seconds), filling and imaging a phantom was going to be a great challenge. Hence  $^{124}\text{I}$ , which is a high-energy radioisotope like  $^{82}\text{Rb}$ , was used in this phantom study as a surrogate for  $^{82}\text{Rb}$ . Static cardiac phantom studies with  $^{99\text{m}}\text{Tc}$ ,  $^{18}\text{F}$  and  $^{124}\text{I}$  (surrogate for  $^{82}\text{Rb}$ ) were conducted. The percent defect sizes were measured and compared with the true defect size. Our results demonstrated that at 45% threshold, the measured defect size was representative of true defect size for  $^{99\text{m}}\text{Tc}$  SPECT data. Using this threshold as the standard, we smoothed the  $^{18}\text{F}$  and  $^{124}\text{I}$  PET data until the measured defect size for PET was representative of the true defect size. An optimal filter cutoff frequency (Butterworth filter, cutoff = 0.80 cycles/pixel, order=5 at 45% threshold for  $^{124}\text{I}$  or  $^{82}\text{Rb}$ ) was found for the PET data within the range of values studied, and this frequency was higher than the clinical norm for SPECT data. Our results also illustrated

that the measured SPECT defect size varied greatly depending on the thresholds used to define a defect, whereas measure PET defect size was relatively constant over the range of cutoffs tested<sup>7</sup>. The optimal cutoff may depend on defect size, patient variability, and noise level. When assessing myocardial defect size, physical properties need to be taken into consideration, particularly when comparing images obtained using different nuclides (i.e. <sup>82</sup>Rb or <sup>99m</sup>Tc agent perfusion and <sup>18</sup>F FDG viability).

## CHAPTER 1 Introduction

### 1.1 Myocardial perfusion imaging (MPI)

Myocardial perfusion imaging is a widely used noninvasive imaging modality for the diagnosis and management of coronary artery disease (CAD). In patients with known CAD, it is used to determine functional significance of known lesions to predict the success of revascularization. This modality permits evaluation of the perfused myocardium and functional assessment through electrocardiogram (ECG)-gating of the perfusion images. The two most commonly used isotopes for myocardial perfusion imaging are thallium-201 ( $^{201}\text{Tl}$ ) and technetium-99m ( $^{99\text{m}}\text{Tc}$ ).

$^{201}\text{Tl}$  is generated by a cyclotron and then transported as a finished product to the location where it is used, which is feasible because it has a half life of 73 hours. The isotope decays by a reasonably complex scheme, but most of the photons have an energy of about 80 keV, which is a relatively low energy.  $^{99\text{m}}\text{Tc}$  is bound to other compounds for the purposes of myocardial perfusion imaging. It is formed on site by elution from a molybdenum-99 generator.  $^{99\text{m}}\text{Tc}$  is a meta-stable compound which is constantly formed from molybdenum-99 within the generator.  $^{99\text{m}}\text{Tc}$  has a half life of about six hours, and emits photons with 140 keV energy. This energy is higher than the emissions of thallium.

The differences in physical properties between  $^{201}\text{Tl}$  and  $^{99\text{m}}\text{Tc}$  are relevant to the choice of radiopharmaceutical, which will be discussed later<sup>8</sup>.

Both  $^{201}\text{Tl}$  and  $^{99\text{m}}\text{Tc}$  radiopharmaceuticals are imaged using single photon emission computed tomography (SPECT). Single photon imaging uses radioisotopes that decay by gamma-ray emission. For the tomographic mode of single photon imaging (SPECT), data are collected from many angles around the patient. This allows cross-sectional images of the radionuclide to be reconstructed. The resulting image represents the biodistribution of the injected radiotracer. Most SPECT radiotracers have a photon energy ranging from 70 to 300keV that are detected by a thin sodium iodide (NaI) crystal only after passing through a lead collimator to ensure proper directional information.

Regardless of the radiopharmaceutical used, SPECT imaging is performed at rest and during stress to produce images of myocardial regional uptake that reflect changes in relative regional myocardial blood flow. During maximal exercise or vasodilator stress, myocardial blood flow is typically increased three- to fivefold compared to rest<sup>8</sup>. In the presence of a significant coronary stenosis, myocardial perfusion will not increase appropriately in the territory supplied by the artery with the stenosis, creating heterogeneous uptake. In patients who are unable to exercise, either one of the two coronary vasodilators, adenosine or dipyridamole, may be used to increase blood flow<sup>8</sup>.

$^{201}\text{Tl}$  is a potassium analogue that is taken up by viable myocardial cells in direct proportion to coronary blood flow. The initial thallium injection is performed at peak stress, when hypoperfused myocardium will have less uptake than myocardium with normal perfusion. Over the next few hours "redistribution" of thallium occurs as a result of

a fairly complex process. Thallium will wash out of the myocardium at a rate dependent on local myocardial perfusion. At the same time, thallium will be redelivered to the myocardium from a large reservoir in the blood pool. The distribution of  $^{201}\text{Tl}$  in the myocardium is not static but changes as a function of time. This phenomenon is referred to as redistribution<sup>9</sup>. The final result of this process is that a region of ischemic but viable myocardium which initially has less than normal uptake will become equal to normal regions over time. This "redistribution" is then detected on subsequent imaging. In contrast, areas of infarction or fibrosis will have reduced uptake initially that does not change over time.

Both  $^{201}\text{Tl}$  and  $^{99\text{m}}\text{Tc}$  based perfusion agents are widely available. Despite the established value of  $^{201}\text{Tl}$ , the physical properties of the agent have been considered suboptimal for scintillation camera imaging. The long half-life and biodistribution limits the amount of  $^{201}\text{Tl}$  chloride that can be administered to 3-5mCi.

Several  $^{99\text{m}}\text{Tc}$ -labeled agents have been developed to circumvent this problem.  $^{99\text{m}}\text{Tc}$  sestamibi and tetrofosmin are both useful as perfusion agents. Through a different mechanism of action than  $^{201}\text{Tl}$  chloride, these  $^{99\text{m}}\text{Tc}$  agents accumulate and remain in perfused myocardium (ie. no significant redistribution). To assess relative perfusion changes following stress, either a 2-day protocol or a low dose (resting)/high dose (stress) must be performed.

The potential advantages of these agents are<sup>9</sup>:

- Their optimal photon energy (140 keV) improves image resolution.
- Their shorter physical half-life decreasing the total radiation dose to the patient and allows injection of a higher (10 times) dose, which improves image quality.
- Higher counting statistics allows for gating of perfusion images, which yields regional and global left ventricular function measurements.
- It is also possible to perform first-pass ventricular function studies, in which a high photon flux is required to evaluate cardiac function during only a few heart beats.

In general, the better image quality, faster imaging protocols and ventricular function assessment that is achieved with  $^{99m}\text{Tc}$  perfusion agents are the most important considerations, and account for the popularity of these agents in most nuclear cardiology laboratories.

$^{82}\text{Rb}$  is a positron emitting radioisotope that, like thallium, is a potassium analog. It is produced from a commercially available, FDA approved strontium-82 containing generator, which must be replenished 13 times a year. Its short half-life allows rapid back to back repeated acquisitions every 10 minutes. The  $^{82}\text{Rb}$  generator is computer controlled and delivers a measured bolus of activity when activated. The short half-life of  $^{82}\text{Rb}$ , however, imposes a limit on the available imaging time for each injection, and a limit on the obtainable image counts, thus requiring a high sensitivity multicrystal PET scanner, which is able, at the same time, to handle the high amount of activity (50-60 mCi) injected

without running into deadtime problems<sup>10</sup>. Modern multicrystal PET camera designs allow high sensitivity of detection, as well as negligible losses from dead-time<sup>11</sup>. Early on  $^{82}\text{Rb}$  PET imaging was limited to a few PET centers due to financial costs<sup>12</sup>. Technological advances in the PET machine and reimbursement of PET by the Health Care Finance Administration made it much more affordable.

The cameras used to image positrons are distinctly different than those which detect single photon emitting radiopharmaceuticals. As described below, PET imaging can permit shorter imaging times and absolute quantitation. PET attenuation correction reduces the number of artifacts caused by soft tissue attenuation in SPECT imaging.

Soft tissue attenuation is a major limitation of SPECT imaging with either  $^{201}\text{Tl}$  or  $^{99\text{m}}\text{Tc}$ , although it is more pronounced with the former, because of its lower energy emission. Although systems for attenuation correction are now available on several commercial camera systems, they have not yet proven to be of clear benefit. Further developments in this regard are anticipated.

## **1.2 PET vs. SPECT**

Before explaining the benefits of rubidium-82 as a myocardial perfusion, a brief comparison between the two imaging techniques, positron emission tomography and single photon emission computed tomography, is discussed. Positron emission tomography (PET) makes use of the radioisotopes that decay by positron emission. The emitted positron has a very short lifetime and, following annihilation with an electron, simultaneously produces two gamma rays that subsequently are detected by the camera. Like SPECT imaging, tomographic images are formed by collecting data from many angles around the patient,

resulting in volumetric PET images. In contrast to SPECT imaging, PET imaging takes advantage of the fact that the photons are emitted at 180° angle and utilizes “coincidence detection” (electronic collimation) in place of physical collimation. This allows for substantially more photons being detected (less are lost to the collimators), resulting in better imaging statistics. Additionally, the image biodistribution of the radiotracer (emission scan) is routinely acquired along with a map of the tissue attenuation, and the final images are corrected for the effects of soft tissue attenuation. The resultant PET images have fewer artifacts from soft tissue attenuation and permits absolute quantitation. In other words, PET is an advanced imaging technique that allows non-invasive measurement of absolute concentrations of positron-emitting radiotracers with high spatial and temporal resolution. PET imaging with perfusion tracers such as rubidium-82 ( $^{82}\text{Rb}$ ) or nitrogen-13 ( $^{13}\text{N}$ ) ammonia, has a higher diagnostic accuracy when compared with other the noninvasive tests for the detection of coronary artery disease (CAD), and it can be used to evaluate serial changes in perfusion reserve<sup>13</sup>.

The short half-life of the perfusion tracers such as  $^{82}\text{Rb}$ , in combination with highly sophisticated hardware and software enables PET studies to be acquired relatively quickly with high patient throughput. PET perfusion imaging has a higher diagnostic accuracy than SPECT<sup>14</sup>. PET allows for quantitative assessment of the myocardial perfusion reserve which can detect the magnitude and competence of collaterals in regions with occluded epicardial collaterals. Absolute quantitation of myocardial flow reserve can also help identify multivessel “balanced” ischemia that is often not detected by SPECT imaging.



Hence, the assessment of myocardial perfusion/function using positron emission tomography (PET) is rapidly advancing.

While PET and SPECT rely on similar principles to produce images, important differences in instrumentation and experimental applications are dictated by inherent differences in their respective physics of radioactive decay. One intrinsic limitation of PET derives from the nature of positron decay and the principle of coincidence detection. PET specifically recognizes the site of positron annihilation and not the site of radioactive decay. The distance separating the two events, decay and annihilation, depends on the average kinetic energy of the positron as it leaves the nucleus, and varies according to the specific isotope involved<sup>15</sup>. Moreover, if the positron is not entirely at rest at the point of annihilation, photons will be emitted at an angle slightly different than  $180^\circ$  (non-collinearity). Both, remote positron annihilation and photon non-collinearity place a theoretical limit on the achievable spatial resolution of PET, which is dependent on the positron emission energy<sup>16</sup>.

Instead of coincidence detection, SPECT uses a technique called *collimation*<sup>17</sup>. A collimator is a lead block containing many tiny holes that is interposed between the subject and the radiation detector. The holes are long and narrow so as to permit only photons of essentially parallel trajectory to pass through the collimator and reach the detector. In comparison to parallel photons,  $\gamma$  rays, that deviate slightly are absorbed by the lead and go undetected. Hence, collimation is less efficient than coincidence detection, as the majority of photons are filtered out<sup>18</sup>.

Attenuation is the loss of true events due to scatter and absorption. The effects of soft tissue attenuation in PET are substantially different from those in SPECT. Both the annihilation photons must leave the body relatively un-attenuated for the event to be detected in PET. Hence, the probability of the event being attenuated is higher in PET than SPECT imaging. The most obvious effect of attenuation is the photons not reaching the camera resulting in apparent photon defects in the resultant images. Image uniformity is a very important property of PET imaging for cardiac imaging. Coincidence detection allows more effective correction for non-uniform attenuation than for SPECT imaging<sup>19-21</sup>. Non-uniform attenuation in the chest results in multiple different patterns of SPECT images attenuation, depending on body habitus and the heart position<sup>22-24</sup>. Current attenuation correction hardware and software algorithms for SPECT imaging have come a long way in improved effectiveness but offer only a partial correction of the problem, and sometimes result in greater error<sup>19-21, 25</sup>. Hence the SPECT attenuation correction methods are not widely used<sup>25</sup>. Furthermore, most SPECT cardiac acquisition is performed over 180° to 270° over the chest, which results in additional spatial distortion and non-uniformity<sup>26, 27</sup>. A real perfusion defect may be exaggerated in size and severity. On the other hand, a real perfusion defect can be hidden within an area of apparent attenuation. Attenuation correction gives an exact correction in PET, as opposed to an approximate one in SPECT, but the magnitude of the correction factors required in PET is far greater than in SPECT due to the need to correct for 2 photons.

Myocardial perfusion PET is particularly useful in reducing the number of false-positive SPECT scans due to the routine application of attenuation correction. The higher

sensitivity of PET can also be useful in the evaluation of coronary vascular reserve in view of negative SPECT results. MacIntyre et al assessed outcome in patients with true-positive PET scans and false-negative  $^{201}\text{Tl}$  SPECT scans and found that PET was more accurate than SPECT in predicting successful revascularization <sup>28</sup>. Patterson et al showed that perfusion PET is the most cost-effective diagnostic procedure in patients with a low to intermediate likelihood of coronary artery disease at pre-testing <sup>29</sup>. Gated perfusion PET provides additional information regarding left ventricular regional and global function similar to gated perfusion SPECT <sup>14, 30</sup>

### **1.3 Rubidium-82 PET for Myocardial Perfusion Imaging**

The main advantages of  $^{82}\text{Rb}$  PET over  $^{201}\text{Tl}$  and  $^{99\text{m}}\text{Tc}$  SPECT can be listed as the following:

- Short half-life (76 s) of  $^{82}\text{Rb}$  allows multiple sequential data acquisitions in a short duration of time,
- Reduces the number of false-positive SPECT scans due to the routine application of attenuation correction,
- Attenuation correction also allows for absolute quantitation.

Despite these advantages,  $^{82}\text{Rb}$  PET imaging is limited by its 76s half-life, and generator elution method which provides a 40-60mCi infusion over 15-60seconds, imaging the myocardium becomes challenging with the prolonged infusion resulting in high “background” activity in the left ventricular cavity, making it difficult to discern the myocardial wall in the earlier dynamic images. The 76s half life further complicates issues making it difficult to acquire an adequate number of counts (ie. while waiting for the

background to clear, the myocardial counts are decaying away.  $^{82}\text{Rb}$  emits a relatively high energy positron, which can travel several millimeters prior to annihilation. As PET images the resultant annihilation photons, the actual location of the positron emission is not known. While PET camera has a spatial resolution of  $\sim 4\text{-}6\text{mm}$ , the addition of the uncertainty of not knowing exactly where the positron was emitted from reduces the overall images resolution in  $^{82}\text{Rb}$  PET imaging.

For these reason, using standard reconstruction and filtering methods, the resultant images quality of  $^{82}\text{Rb}$  myocardial perfusion imaging is not much better than that of SPECT; however due to the attenuation correction, the images have high diagnostic accuracy.

There have been several studies done in order to compare perfusion imaging with PET and SPECT in the assessment of CAD. Stewart et al found  $^{82}\text{Rb}$  PET to be superior to  $^{201}\text{Tl}$  SPECT in terms of specificity (84% versus 53%) and predictive accuracy (85% versus 79%)<sup>14,31</sup>. In a similar study, PET was found to be more accurate than SPECT, with a higher sensitivity (95% versus 79%), specificity (82% versus 76%), and predictive accuracy (92% versus 78%)<sup>1</sup>. Tamaki et al compared exercise  $^{201}\text{Tl}$ - SPECT and dipyridamole  $^{13}\text{NH}_3$  PET in 48 patients with coronary artery disease<sup>32</sup>. The authors reported a sensitivity of 88% for PET and 81% for SPECT in the detection of stenoses greater than 50%<sup>32</sup>. In detection of coronary collaterals using dipyridamole PET myocardial perfusion imaging,  $^{82}\text{Rb}$  had 90% sensitivity, 88% specificity and 90% accuracy ( $p < 0.0001$ )<sup>33</sup>.

#### **1.4 Assessment of Myocardial Function**

The ability to acquire cardiac images in conjunction with electrocardiogram (ECG) gating permits simultaneous assessment of cardiac perfusion and function.

$^{201}\text{Tl}$  gated SPECT studies are frequently non-diagnostic due to low counts and low energy which leads to poor image quality and variability in representing true wall thickening and regional wall motion. However, both  $^{99\text{m}}\text{Tc}$  sestamibi/tetrofosmin SPECT and  $^{82}\text{Rb}$  PET can be used for gated studies due to their higher photon flux.

#### **1.5 Problem Statement**

The major challenge of  $^{82}\text{Rb}$  imaging is determining when to begin the image acquisition post infusion. As the infusion time is ~30- 60 seconds, depending on the age of the generator, and the half-life is only 76 seconds, the infusion/imaging protocol is critical as imaging too early results in images with high background (low contrast), and imaging too late results in noisy images due to low count statistics. The centers that currently use  $^{82}\text{Rb}$  PET use generalized parameters, but most admit to having to individually tailor protocols to produce diagnostic quality images.

Evaluation of the dynamic images may enable a standardized gated  $^{82}\text{Rb}$  PET imaging protocol to be developed. Routine gating can allow for assessment of regional wall motion and regional wall thickening and, left ventricular ejection fraction (LVEF) calculation from the changes in left ventricle volume throughout the cardiac cycle. Currently, in clinical practice, these parameters are routinely determined during nuclear scintigraphy by gated SPECT perfusion imaging or First-Pass radionuclide angiography (FPRNA), techniques which are discussed in details in Chapter 4.

The clinical protocol implemented at Virginia Commonwealth University Health System (VCUHS) is to acquire dynamic  $^{82}\text{Rb}$  PET images at rest using 40 mCi of  $^{82}\text{Rb}$ , imaging in 30sec intervals for 6 minutes. The images are reconstructed and reviewed to determine the first image frame without significant blood pool activity in the ventricular cavity, and the time is recorded. A summed rest perfusion image is created by summing the images from that point to the end, hence eliminating early images with higher background counts. As the GE PET/CT scanner cannot simultaneously acquire a dynamic/gated image, a separate gated acquisition is performed using 40 mCi of  $^{82}\text{Rb}$  (8 frames per cardiac cycle), beginning data acquisition at the time determined from the previous resting dynamic study. The patient then receives a 3-minute dipyridamole (DIP) infusion and the above mentioned dynamic and gated imaging protocol is repeated while patient is in vasodilatory induced cardiovascular stress.

The current protocol has its limitations. The patient has to undergo 4  $^{82}\text{Rb}$  injections. If the optimal time to begin imaging were known, only the 2 gated studies would need to be performed; thus reducing the total radiation exposure and imaging time. Moreover, in the current protocol, the determination of background clearance is subjective and time consuming and can lead to variability in image quality. The bottom-line is that the optimal time post injection to begin the gated acquisition, so the composite image will routinely produce a diagnostic image, is not known. The fact that generator aging results in prolonged infusion times later in the month may play a role in the inability to accurately identify a single time point at which to begin the gated image.

Regarding the resulting gated images, while software packages like quantitative gated SPECT (QGS), has been shown to be useful in the routine calculation of LVEF and volumetric parameters using SPECT agents. Given the differences in imaging technology and disintegration energies, the capability of QGS to provide similar results with the  $^{82}\text{Rb}$  PET data has yet to be determined. For these same reasons, the optimal reconstruction/filtering parameters of  $^{82}\text{Rb}$  PET myocardial imaging has not been evaluated to determine whether the measured percent defect actually represents the true percent size of the myocardial defect.

## **1.6 Scope of the Thesis**

The goal is to determine the parameters that most effect the optimal time post injection to begin the gated acquisition, so the composite image (summation of the gated frames) will routinely produce a diagnostic image. Due to differences in imaging technology, this study will investigate the correlation between  $^{99\text{m}}\text{Tc}$  first pass radionuclide angiography (FPRNA) LVEF and volumetric parameters and those obtained from QGS analysis of  $^{82}\text{Rb}$  gated PET data. It will also determine the optimal filtering parameters that allow  $^{82}\text{Rb}$  PET imaging to represent the true size of a perfusion defect.

The overall objective of this study was to optimize and standardize an  $^{82}\text{Rb}$  PET imaging protocol that would be applicable to other centers with little or no adjustment needed.

Since this project revolves around PET, it is necessary to understand the physics, characteristics, advantages and limitations of this modality. Chapter 2 covers the basic principles and background of PET in details. It also describes the PET detectors, scanner

designs, 2-D and 3-D data acquisitions for the readers to understand the difference and advantages of each method. At the end of the chapter, a brief discussion regarding the principles of SPECT modality is done to further enhance the significance of PET in the readers' mind. Chapter 3 covers the work done towards understanding and analyzing the current  $^{82}\text{Rb}$  PET imaging protocol at VCUHS. In addition, the possibility of developing a standardized gated  $^{82}\text{Rb}$  PET imaging protocol where the optimal time post infusion to begin the acquisition is already known or can be predicted, is explored. Chapter 4 covers the theory, results and discussions of the comparison of  $^{82}\text{Rb}$  gated PET LVEF using QGS with  $^{99\text{m}}\text{Tc}$  First Pass Radionuclide Angiography (FPRNA) left ventricular ejection fraction (LVEF). Chapter 5 covers the final objective, which was to investigate whether PET with an  $^{82}\text{Rb}$ -labeled tracer would provide information on defect size similar to that provided by  $^{99\text{m}}\text{Tc}$  SPECT, using a cardiac phantom in which the true defect size was known.



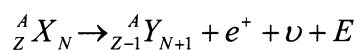
## **CHAPTER 2 Positron Emission Tomography (PET) Background**

Positron emission tomography (PET) is a medical imaging technology capable of imaging the biology of disorders at the molecular level often before anatomical changes are visible. Simply stated, PET scans are digital images that can, in many cases, identify and provide prognostic information about many forms of cancer, heart disease, and brain disorders such as Alzheimer's, Parkinson's, and epilepsy.

A PET scan is very different from an ultrasound, X-ray, MRI, or CT, which detect changes in the body structure or anatomy, such as a lesion (for example, a sizeable tumor) or musculoskeletal injury. A PET scan can distinguish between benign and malignant disorders (or between alive and dead tissue), unlike other imaging technologies which merely confirm the presence of a mass. A PET scan can detect abnormalities in cellular activity generally before there is any anatomical change. A PET scan can, in many cases, identify diseases earlier and with higher specificity than ultrasound, X-rays, CT, or MRI. PET can also help physicians monitor the treatment of disease. For example, chemotherapy leads to changes in cellular activity and that is observable by PET long before structural changes can be measured by ultrasound, X-rays, CT, or MRI. Hence, a PET scan gives physicians another tool to evaluate treatments, perhaps even leading to a modification in treatment, before an evaluation could be made using other imaging technologies.

## 2.1 Positron Physics

PET imaging relies on the nature of the positron and positron decay. When a nucleus undergoes decay, the result is a new nuclide with 1 fewer protons and 1 more neutron, as well as the emission of a positron and a neutrino:



The radioisotopes that decay via positron emission are proton-rich and move closer to the line of stability while giving off a positive charge. The PET radioisotopes used commonly in medicine are shown in Table 2.1. Most of these positron-emitting isotopes have relatively short half-lives. The half-life ( $T_{1/2}$ ) of a radionuclide is the time required for it to decay to 50% of its initial activity level <sup>34</sup>.

Table 2.1: Properties of commonly used PET Radioisotopes

Nuclide	Half-life	Maximum positron energy (MeV)	Production method
<sup>11</sup> C	20.3 min	0.96	Cyclotron
<sup>13</sup> N	9.97 min	1.19	Cyclotron
<sup>15</sup> O	2.03 min	1.70	Cyclotron
<sup>18</sup> F	109.8 min	0.64	Cyclotron
<sup>82</sup> Rb	1.16 min	3.35	Generator (from <sup>82</sup> Sr)
<sup>124</sup> I	4.18 days	1.5	Cyclotron

## 2.2 Positron Annihilation

When a positron undergoes mutual annihilation with a negative electron, their rest masses are converted into a pair of annihilation photons. In the annihilation process, the initial energy is from the electron and positron masses, since they are moving relatively slowly at the time of interaction and the final energy is the combined energies of the photons which have no mass. The photons have identical energies (511 keV) and are

emitted simultaneously, in  $180^\circ$  opposing directions as shown in Figure 1, usually within a few tenths of mm to a few mm of the location of where the positron was emitted, depending on the energy and the range of positrons (Figure 1).

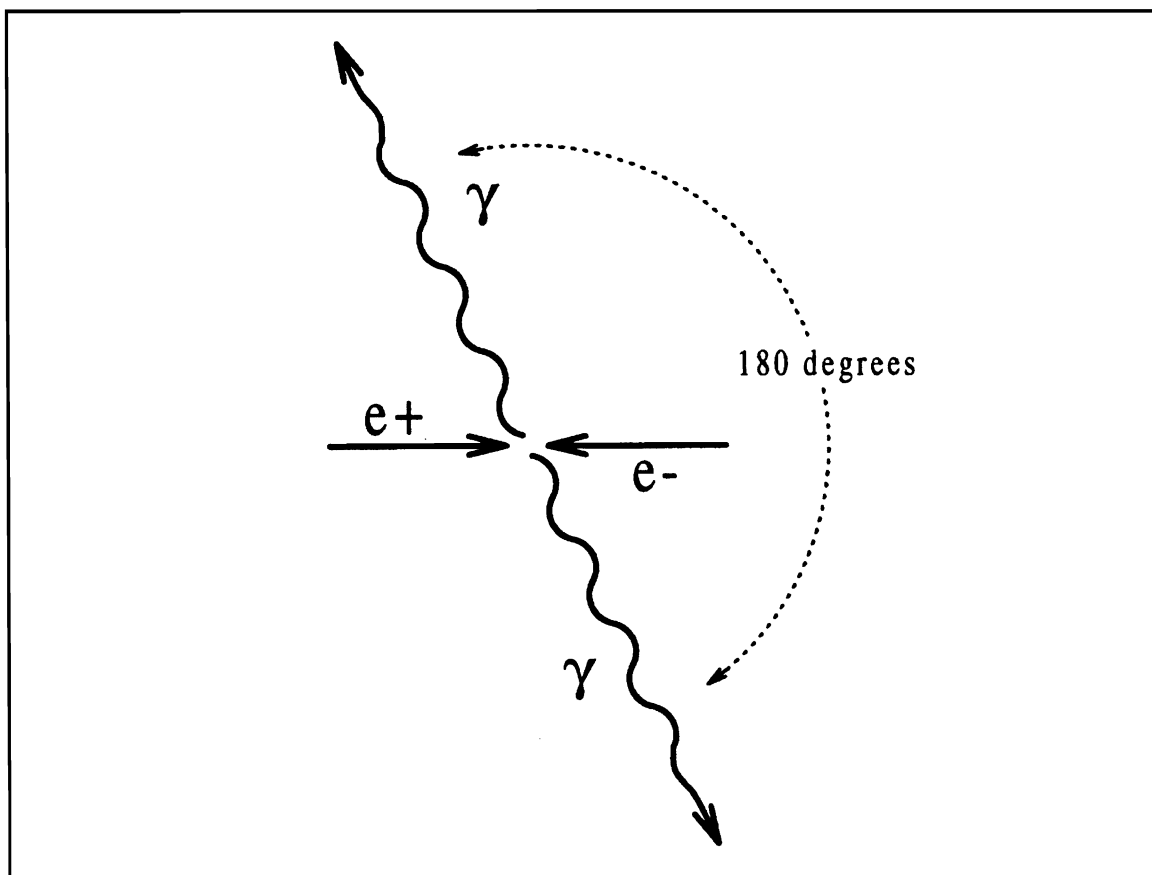
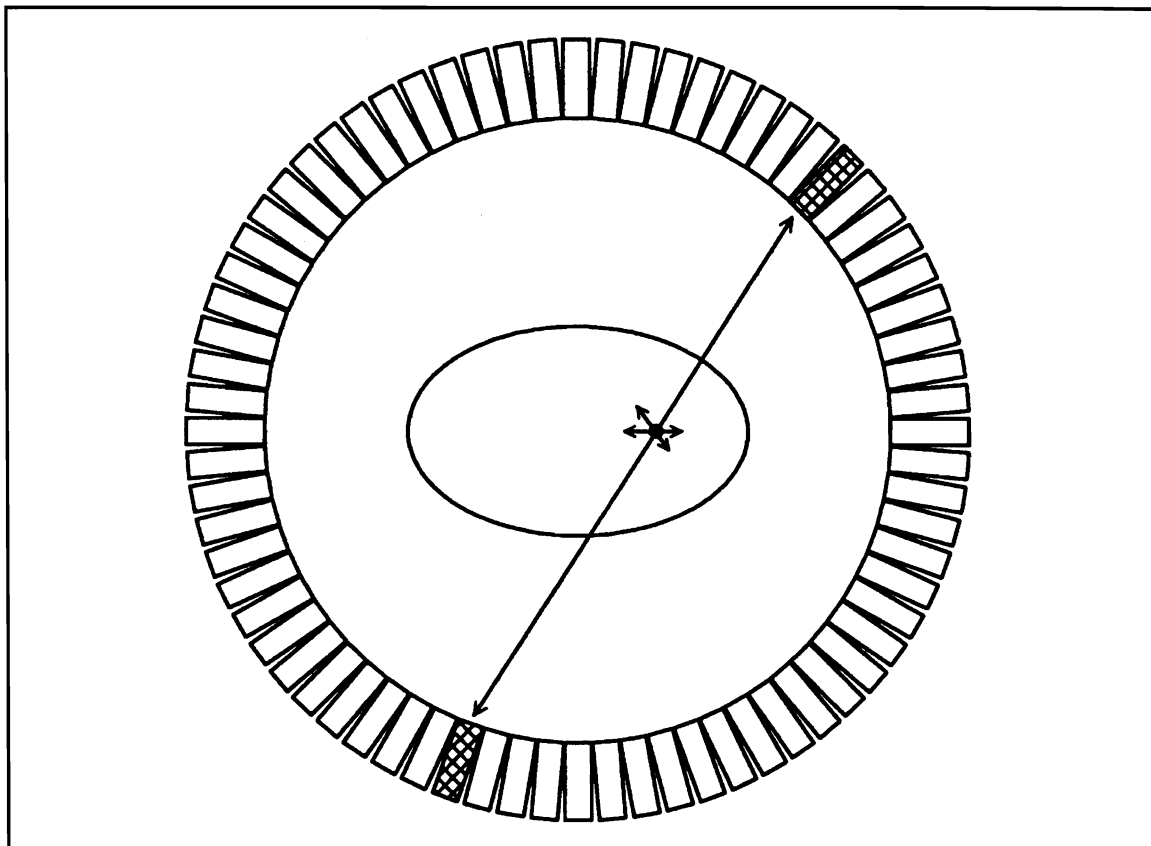


Figure 1. Diagram of electron–positron annihilation, producing two 511 keV photons leaving in opposite directions. Images courtesy of Timothy G. Turkington from Department of Radiology, Duke University Medical Center, Durham, North Carolina (Introduction to PET Instrumentation - J Nucl Med Technol 2001 29: 4-11)

### 2.3 Coincidence Detection

When a positron emission occurs in a patient who is within a ring of radiation detectors as shown in Figure 2, the positron moves a short distance in a random direction, slowing down until it annihilates with an electron. The annihilation yields two 511-keV

photons, which are emitted in nearly opposite direction. Although most of the annihilation photons will not be detected, some will remain in the plane of the detector ring, and 2 of the detectors will be hit, yielding electronic signals. The near-simultaneous detection of the two annihilation photons, referred to as a “coincidence”, allows PET to localize their origin along a line between the two detectors, without the use of absorptive collimators. This is known as *electronic collimation*. Improved sensitivity and improved uniformity of the *point source response function* (psrf) are the two major advantages of electronic collimation over physical collimation. A physical collimator prevents photons which are not normal or nearly normal to the collimator face from falling on the detector in order to gain directional information. However in electronic collimation, these photons may be detected and used as signals. This results in a significant gain in sensitivity (typically by a factor of 10 or more for 2D mode PET compared to SPECT). The path between 2 detectors is referred to as a line of response (LOR). The number of coincidence events occurring between detectors indicates how much radioactivity there was on the LOR between the detectors<sup>35</sup> (Figure 2).



**Figure 2. Coincidence event detected in ring PET scanner. Images courtesy of Timothy G. Turkington from Department of Radiology, Duke University Medical Center, Durham, North Carolina (Introduction to PET Instrumentation - J Nucl Med Technol 2001 29: 4-11)**

Over the course of a PET scan, the system counts the number of times each pair of detectors is hit in coincidence. For a ring with  $n$  detectors, there are  $n(n-1)/2$  ways to pair up the detectors, so a great deal of information is recorded<sup>36</sup>.

The full-width at half-maximum (FWHM) of the psrf, in SPECT, increases with increasing distance of the source from the collimator (Figure 3) results in variable resolution in the reconstructed images. In PET, as discussed earlier, a coincidence event may be detected if the direction of the annihilation photons is constrained to lie along a LOR joining both detector faces. If the annihilation photons are strictly anti-parallel, the

psrf varies in a similar way to that shown in (Figure 3b). Due to the slight uncertainty in the direction of the annihilation photons, this constraint is relaxed a bit and in practice, the psrf changes slightly in the central third of the FOV <sup>37</sup>. This directly results in the resolution of reconstructed PET images to be more uniform than that for SPECT images.

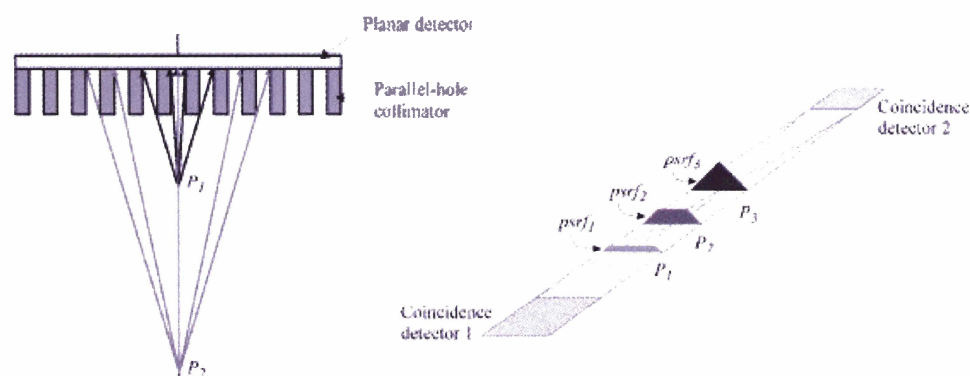


**Figure 3. Variation of point source response function (psrf) with position P in SPECT and in PET. . Image derived from "Aspects of Optimization and Quantification in Three-Dimensional Positron Emission Tomography", a thesis submitted to the University of London by RD Badawi in 1998.**

The two major photon interactions resulting from the positron annihilation are photoelectric effect and Compton scattering. The energy of the gamma photons in PET (511 keV) is too low for the pair production to occur. These basic processes are the same for any type of electromagnetic radiation and therefore occur in other medical imaging modalities such as traditional X-ray and CT.

### 2.3.1 Photoelectric Effect

The *photoelectric effect* is a process in which an atom totally absorbs the energy of an incident photon. The photon disappears and the energy absorbed is used to eject an orbital electron from the atom causing it to produce an ion pair. The ejected electron is

called a *photoelectron*<sup>34</sup>. The photoelectric effect has the highest probability with lower energy photons and nuclei having high atomic numbers.

### 2.3.2 Compton Scattering

*Compton scattering* is a “collision” between a photon and a loosely bound outer shell orbital electron of an atom. In Compton scattering, because the incident photon energy greatly exceeds the binding energy of the electron to the atom, the interaction looks like a collision between the photon and a “free” electron<sup>34</sup>. When only a portion of the electromagnetic radiation is transferred to an electron, an ion pair is produced while a less energetic photon, having been “scattered”, continues in an alternate direction. The energy of the photon after interaction is given by the following equation:

$$E' = \frac{E_0}{1 + (E_0 \div m_0c^2)(1 - \cos\theta)}$$

Where E is the energy of the incident photon,  $m_0c^2$  is the mass of the electron at rest,  $E'$  is the energy of the scattered photon and  $\theta$  is the scattering angle. The equation implies that quite large deflections can occur with quite small energy loss.

### 2.3.3 Event Types in Coincidence Detection

Coincidence detection events fall into 3 categories: true, random and scattered (Figure 4).

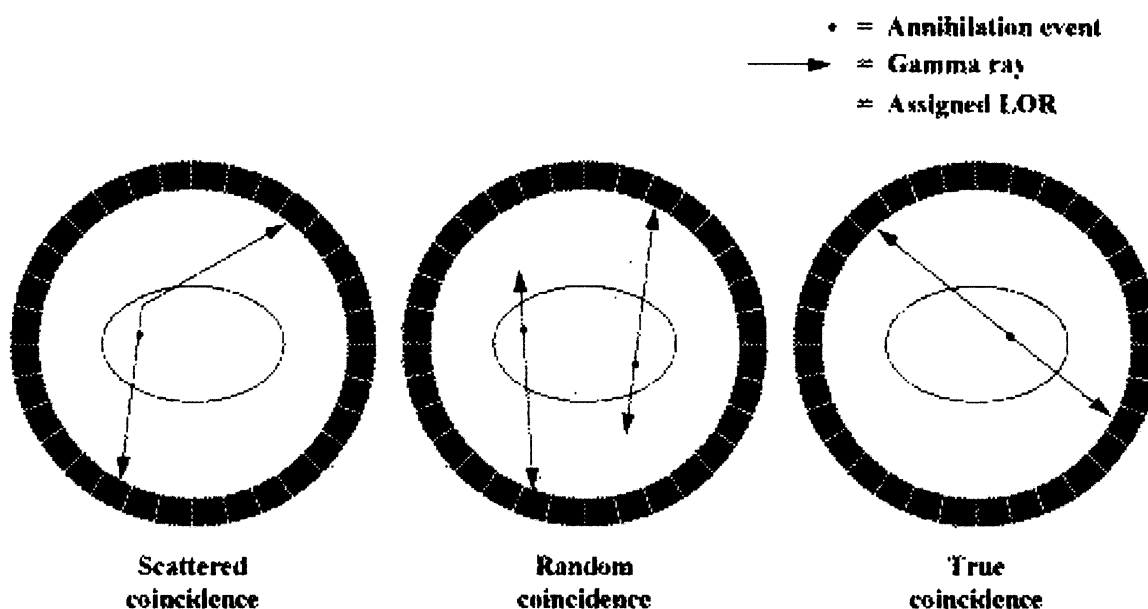


**Figure 4. True coincidence event (right), scattered coincidence event (left), and random or accidental coincidence (center). Scattered and accidental coincidences yield incorrect positional information and contribute a relatively uniform background to the image that results in a loss of contrast. Image derived from "Aspects of Optimization and Quantification in Three-Dimensional Positron Emission Tomography", a thesis submitted to the University of London by RD Badawi in 1998.**

True Coincidence means that the coincidence event recorded arose from a pair of photons produced from the same annihilation event and that the annihilation event occurs somewhere within the coincidence “line of response” (LOR) between the detectors.

Scatter coincidences occur when one (or both) of the photons from an annihilation event outside the sensitive volume of the true coincidence events undergoes scattering and is detected in a detector other than the one that would be appropriate for a true coincidence. Scattered coincidences add a background to the true coincidence distribution which changes slowly with position, decreasing contrast and causing the isotope concentrations to be overestimated. They also add statistical noise to the signal.

Random coincidences (also called accidental coincidences) occur when annihilation photons from two unrelated positron annihilation events are detected in two different



detectors, within the coincidence timing window, and recorded as a single coincidence event. As with the scattered events, the number of random coincidences is fairly uniform across the FOV, and will cause isotope concentrations to be overestimated if not corrected for. Random coincidences also add statistical noise to the data.

## **2.4 PET Detector and Scanner Designs**

As mentioned earlier, detection systems are a key component of any imaging system, and an understanding of their properties is important for establishing appropriate operating criteria or designing schemes for obtaining quantitative information. Detection efficiency is an important parameter in PET scanner sensitivity and performance. Sodium iodide detectors have been used for PET scanners. However sodium iodide, in general, is not the detector material of choice for PET imaging due to the relatively high energy of 511-keV annihilation photons. Hence, most PET scanners use denser higher-Z scintillation detectors arranged in rings. These systems provide high detection efficiency and allow the simultaneous collection of data for all projection angles with a completely stationary set of detectors.

### **2.4.1 Block Detectors**

Early PET systems used individual detector units consisting of a piece of scintillator coupled to a *photomultiplier tube* (PMT). The *block detector*, designed in the mid 1980s by Casey and Nutt, allows small detector elements to be used (improving spatial resolution) while reducing the number of PMT required to read them out (controlling cost) (Figure 5). A large piece of scintillators segmented into an array of many elements by making partial cuts through the crystal with a fine saw. The array of crystals is read out by

four individual PMTs. The depth of the saw cuts is determined empirically to control the light distribution to the four PMTs in fairly linear fashion.

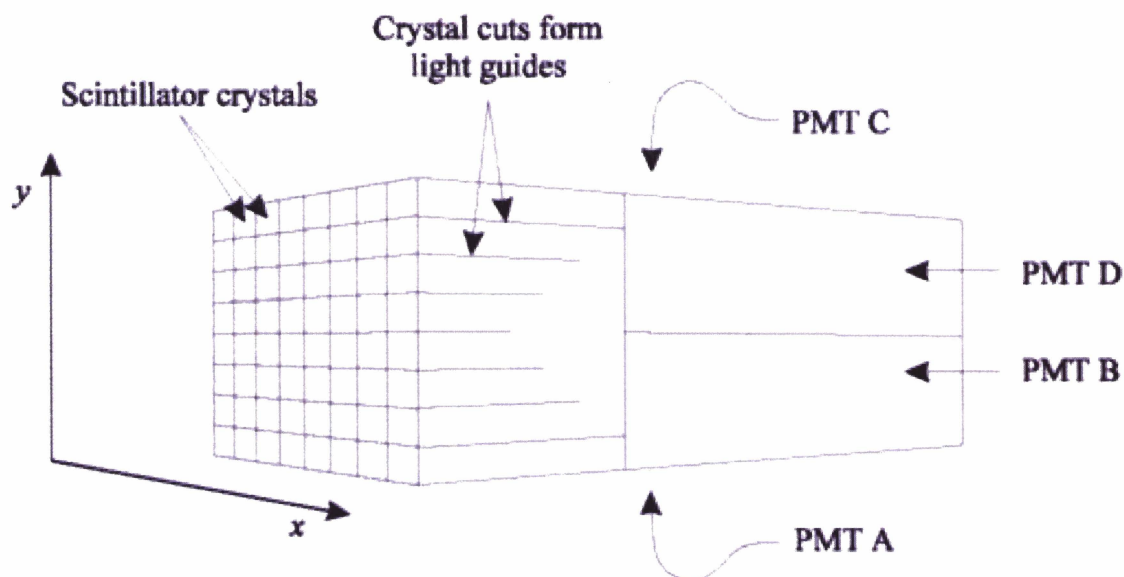


Figure 5. A Block Detector. Image derived from "Aspects of Optimization and Quantification in Three-Dimensional Positron Emission Tomography", a thesis submitted to the University of London by RD Badawi in 1998.

Information on the segment of crystal in which the annihilation photon was detected can be calculated by combining the signals from a four-PMT array as follows:

$$X = \frac{(A + B) - (C + D)}{(A + B + C + D)}$$

$$Y = \frac{(A + C) - (B + D)}{(A + B + C + D)}$$

Where A, B, C and D are the signals from different PMTs, and X and Y signals are then used to determine the sub element of the array in which the annihilation photon was detected. The major advantage of the block detector is that it enables many detector

elements to be decoded using only four PMTs which dramatically lowers the cost per detector element while providing high spatial resolution<sup>34, 38</sup>.

#### **2.4.2 Dedicated PET Systems**

There are various approaches of using the block detectors in clinical PET systems. Systems that use a stationary ring or polygon of array of block detectors, with the detectors operating in multi-coincidence mode, can acquire data for all projection angles simultaneously. There are other systems that use only a few opposing banks of detectors, which must be rotated to get full tomographic information.

### **2.5 Data Acquisition for PET**

#### **2.5.1 Two-Dimensional Data Acquisition**

Initially, most PET scanners are designed with axial collimators or septa between each ring of detectors. As shown in the following figure at left (Figure 6), the septa only detect the photons that are emitted parallel to the plane of detector ring. This is known as *2-D data acquisition*.

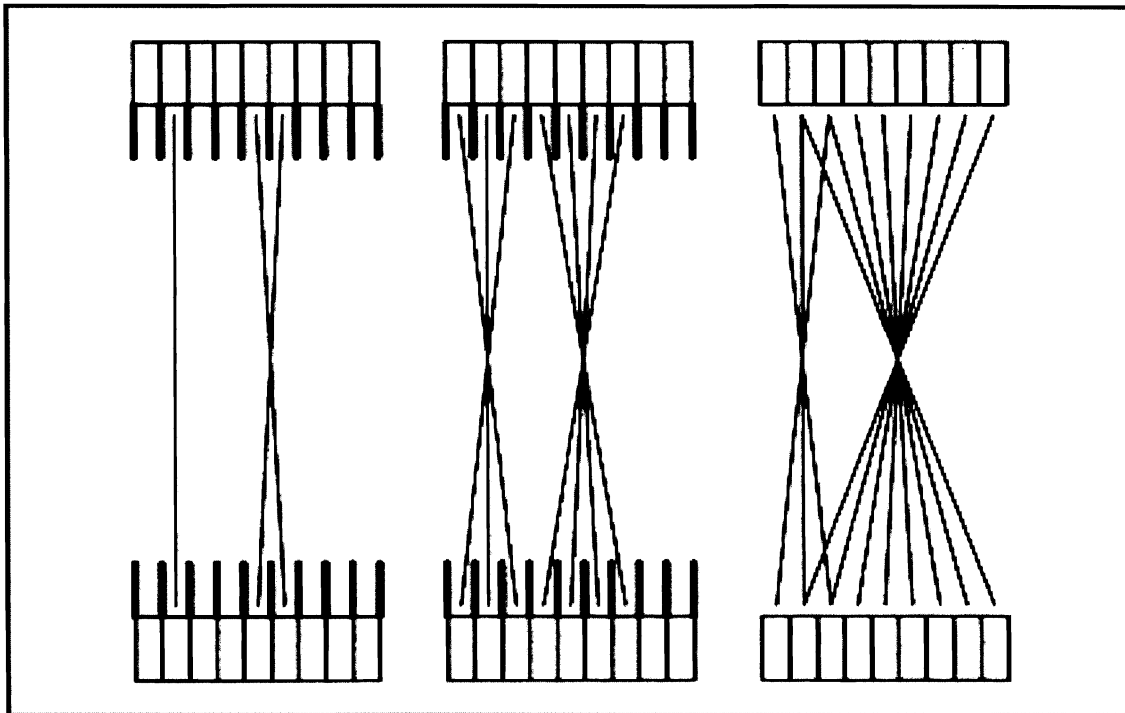


**Figure 6. Multiring PET acquisition modes. At left are examples of simple 2D direct and cross planes. In the middle are extended 2D direct and cross planes for increased efficiency. At right is full 3D acceptance. The acceptance is greater for radiation in the middle of the axial FOV than for radiation near the end. Images courtesy of Timothy G. Turkington from Department of Radiology, Duke University Medical Center, Durham, North Carolina (Introduction to PET Instrumentation - J Nucl Med Technol 2001 29: 4-11)**

The septa provide efficient rejection of scattered annihilation photons in the body and also reduce the single-channel counting rate, which lowers the random coincidence rate and minimizes dead time losses.

2D projection data are analogous to the data obtained with a rotating gamma camera with a parallel hole collimator used for SPECT imaging due to the fact that each crystal ring collects data from a single slice (oblique lines of response are not allowed because of the septa). With no modification of the lengths of septa, the PET scanners also can acquire data from the immediately adjacent rings as shown in the leftmost figure. At the center of the scanner, *cross planes*, as they are called, fall exactly halfway between the

direct planes that are defined by individual crystal rings. Cross planes have twice the sensitivity and counting rates as the direct planes due to the fact that cross planes receive data from two different lines of response. Cross-plane data are reconstructed in the same manner (filtered back projection or iterative approaches) as the direct plane data.

The number of cross planes can be increased by including crystal ring differences of  $\pm 2$ ,  $\pm 3$ , and so forth (center figure above). This will increase the sensitivity at the cost of spatial resolution loss in the axial direction, because of the superposition of data that come from axially disparate locations.

### **2.5.2 Three-Dimensional Data Acquisition**

In *3-D acquisition mode*, the septa are removed, and data are obtained for all possible lines of response as shown in the right-hand side of Figure 7. The sensitivity improves eightfold but the number of scattered photons and the single-channel counting rates also are increased. In 3-D mode, it is important to place the structure of interest as close to the center of the axial FOV as possible because the axial sensitivity profile for 3-D acquisition is determined geometrically and is a triangular function, peaked at the center of the FOV.

3-D PET data reconstruction is much more complicated because they cannot be sorted into a set of independent 2-D slices. Hence, 3-D reconstruction algorithms (Fourier-based and Iterative methods) must be used. The computation times are roughly an order of magnitude longer than for 2-D reconstructions because they involve back projections and computations in 3-D rather than 2-D.

## 2.6 Data Corrections and Quantitative Aspects of PET

There are several physical factors that degrade the quality of images produced by a PET scanner.

### 2.6.1 Scatter

Two different scatter possibilities have been shown in the figure below (Figure 7). The in-plane scatter event, as shown on the left-hand side of the figure, occurs when one photon from annihilation leaves the body unscattered and the other photon scatters before leaving the body. According to the hit detectors, the source of radiation appears to be outside the body. The associated lower energy threshold of the energy window and the energy resolution of detectors determine the degree to which scattered events are accepted.

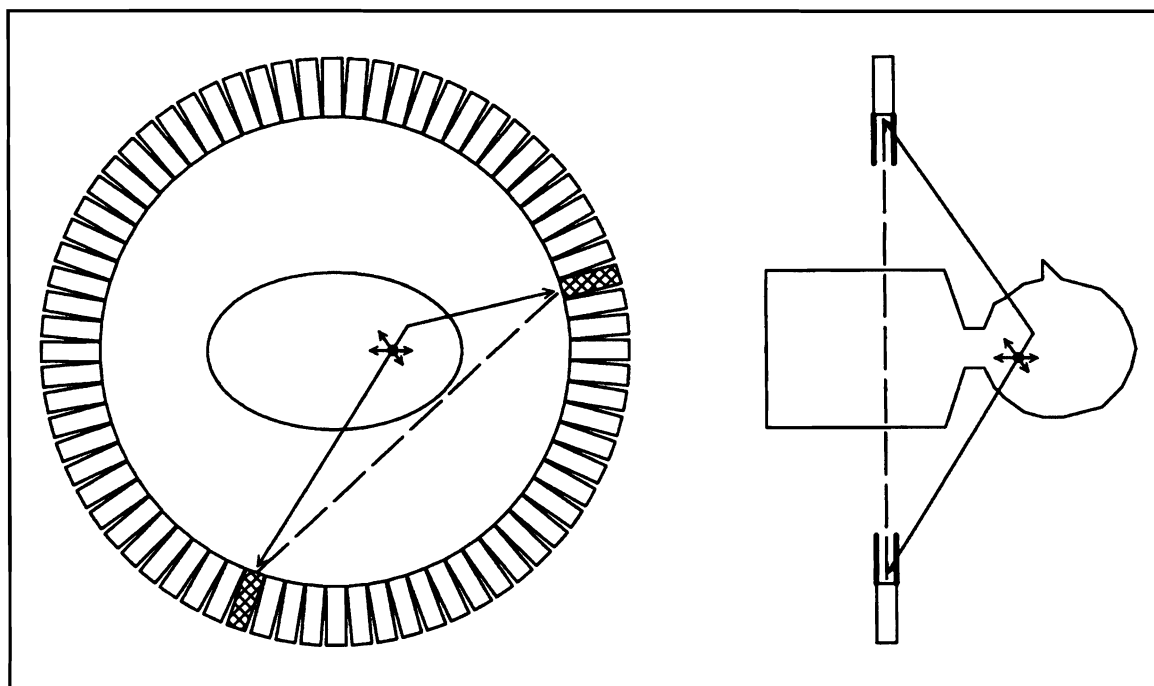


**Figure 7. Scattered Events. Left: In-plane scatter, Right: Out-of-plane scatter, rejected by septa. Images courtesy of Timothy G. Turkington from Department of Radiology, Duke University Medical Center, Durham, North Carolina (Introduction to PET Instrumentation - J Nucl Med Technol 2001 29: 4-11)**

Another scatter possibility, as shown on the right-hand side of the figure, is out-of-plane scatter. In this case, the positron emission is outside the plane of the detector ring. One of the annihilation photons is directed towards the ring, while the other photon is initially directed away from the detectors but eventually scattered back. Quite opposite to the previous possibility, radiation outside the detector ring appears to be in the plane of the detectors. The solution for most out-of-plane scatter is to use shields that block radiation originating outside the field of view (FOV) of the ring. Flat, ring-shaped lead or tungsten septa are used not only to reduce the number of scattered events collected, but also to minimize other effects of radiation originating outside the FOV, namely, dead-time and random events.

### **2.6.2 Correction for Scattered Radiation**

There are two main approaches currently used for scatter correction in PET. The first approach uses information from the original scatter-contaminated image and transmission image to derive the correction. The transmission image reflects the attenuation coefficient of the tissue. Using these two images and computer modeling with some simplifying assumptions, it is possible to derive an estimate of the underlying distribution of scattered events which is then subtracted from projection profiles and the reconstruction is repeated with the scatter-corrected data.

A second method for scatter correction is based on an examination of projection profiles immediately outside the object. After correcting for random coincidences, the only events that should fall into these projection elements are those that are mispositioned due to scatter. Data from the tails of the projection profiles can be extrapolated using simple

smoothly varying functions (Gaussian or cosine) across the entire projection. The extrapolated distribution is then subtracted from the projections prior to image reconstruction.

### **2.6.3 Attenuation**

Attenuation is the loss of true events due to scatter and absorption. PET attenuation effects differ significantly from SPECT attenuation effects. In PET, both the photons have to leave the body unattenuated for the event to be detected. Hence the probability of an event to be attenuated is higher in PET than in SPECT, even though the PET energy is much higher than the typical SPECT energy. Attenuation causes overall loss of counts which in turn results in increased noise and inaccurate quantitation of radioactivity distributions. Attenuation can introduce non-uniformities into the reconstructed images. For example, the radiation emitted from the middle of the body is more likely to be attenuated than the radiation emitted near the edge. The resulting images will therefore, show artificially depleted radioactivity deeper in the body. The outer contour of the body shows an artificially high amount of radioactivity because the radiation emitted tangentially to the outer body contour is not attenuated<sup>35,36</sup>.

### **2.6.4 Attenuation Correction**

There are two general approaches to correct attenuation: calculated correction and measured correction. A calculated attenuation correction assumes that the outer body contour can be known and that; within this contour the attenuation properties are constant<sup>39</sup>.



A measured attenuation correction is done by performing an additional scan. This transmission scan uses a radioactive source and the same detectors used for emission scans to measure the attenuation of the body along all the LOR. The most accurate attenuation correction methods are based on measured transmission scans acquired before, during, or after the emission scan<sup>39</sup>. In this study, the measured attenuation correction was implemented during the PET data reconstruction in form of a CT scan prior to actual PET scan.

### **2.6.5 Dead Time**

Every radiation counting system exhibits a characteristic *dead time* that is related to the time required to process individual detected events<sup>39</sup>. As the rate of photons hitting a detector increases, the probability of missing a photon due to detector dead time increases. This problem hampers the coincidence detection as both photons must be detected. Dead-time losses are minimized by systems with many independent detectors, faster scintillators and processing electronics.

### **2.6.6 Dead Time Corrections**

Most PET scanners use empirical dead time models in which the observed count rate as a function of radioactivity concentration is measure for a range of object sizes and at different thresholds. The resulting data are then fit with paralyzable or nonparalyzable dead time models. Some systems apply a global dead time correction factor for the system, whereas others apply corrections to individual pairs of detector modules.

### 2.6.7 Noise

Image noise can be problematic when dealing with low-count images such as those obtained in nuclear cardiology. The proper usage of filtering can significantly enhance image quality by optimally suppressing noise. Image noise can be decreased with more counts which can be obtained by scanning longer, injecting more radiotracer, or improving the scanner efficiency for detecting emitted radiation.

The level of background plays an important role in the noise quality of data. The counts measured along a particular LOR during a PET scan include true events, random events,  $R$ , and scattered events:  $P = T + S + R$ .

The true events,  $T$ , are obtained by removing the scatter,  $S$ , and random events from the total counts measured during the scan,  $P$ :  $T = P - S - R$ .

The number of true events  $T$  (after corrections) is not an adequate indicator of subsequent image quality. For instance, a study that collected 1 million counts with no background (no scatter and random events) will yield much better images than a study with 1.5 million counts which has 0.5 million counts of background, even after background correction. Actually, the image quality will be similar to those obtained from a 0.7 million-count no-background-acquisition. The effect of background on noise quality is calculated with the noise equivalent count (NEC) formula:

$$\text{NEC} = \frac{T}{T - S - 2R}$$

### 2.6.8 Spatial Resolution

Spatial resolution refers to the number of pixels utilized in construction of an image. Images having higher spatial resolution are composed with greater number of pixels than those of lower spatial resolution. Spatial resolution is an important factor in PET image quality. There are several factors which impact the spatial resolution obtainable from a scanner:

1. Detectors: The spatial resolution of coincidence detection with discrete elements is determined primarily by the size of the individual detector elements. The smaller the detectors are, the better the spatial resolution. However, the issue of depth of interaction puts a limit on the resolution, regardless of the detector size.
2. Positron Path: The spatial resolution of an Annihilation Coincidence Detection (ACD) system is degraded from the value derived from simple geometry by two factors relating to the basic physics of positron emission and annihilation. The first is the finite range of positron travel before it annihilates, based on its initial energy.
3. Non-Colinearity: A second factor involving the physics of positrons is that the annihilation photons almost never are emitted at exactly 180-degree directions from each other. This effect is due to small residual momentum of positron when it reaches the end of its range and is known as *non-colinearity*.

### 2.7 Image Reconstruction

The raw PET data can be reconstructed into cross-sectional images with the same algorithms as SPECT and x-ray CT. After all corrections (e.g. for scatter and attenuation) have been applied to data acquired in a PET camera, the number of counts assigned to an

LOR joining a pair of crystals is proportional to a line integral of the activity along that LOR. Parallel sets of such line integrals are known as projections. There are several ways of reconstruction of images from projections. Transaxial images are created from projection images by some method of tomographic reconstruction. Significant differences, in quality of reconstruction, can be obtained by using different techniques and reconstruction parameters. For 2D reconstruction, the most commonly used algorithm is the analytical method called *Filtered Back-Projection* (FBP). This typically involves the application of a ramp filter which cancels the erroneous activity values created throughout the reconstructed image by simple back-projection, leaving activity distributions only at the true positions<sup>40</sup>. If the projection images were noise free and infinite in number, the ramp filter would give perfect reconstruction of the transaxial slices. Because, however, the numbers of projection images are limited, noise is present throughout the reconstructed image at all frequencies. The ramp filter will amplify the high frequencies and produce an extremely noisy reconstructed image, much worse than is usually seen in planar images. As a result, it is almost always necessary to apply a constraining or smoothing filter to the ramp filter to impose an upper limit, or cut-off, on the frequencies passed through to back-projection, to avoid this excessive amplification of noise at the upper frequencies. Increasing the cut-off retains more high frequencies, which make the image noisier but maintains spatial resolution. Reducing the cut-off removes more low frequencies which makes the image smoother but degrades spatial resolution<sup>40, 41</sup>. This cut-off frequency is usually determined in relation to the Nyquist frequency. This is the highest spatial

frequency that the matrix can accurately sample and retaining frequencies higher than this provides no additional information in the image.

The Nyquist frequency is the inverse of twice the pixel size. In practice, suppression of frequencies above half the Nyquist frequency does not seem to significantly impair spatial resolution. Suppression of lower frequencies does however degrade resolution. A number of filters are available, but all have one thing in common; a smooth transition at the cut-off point, because a sharp cut-off at the upper frequency limit would produce artifacts in the reconstructed image.

The difference amongst the filters is the manner in which they allow the various frequencies in the projection images to pass through to reconstruction. A smooth filter begins to roll-off early and decreases slowly. It should be used with acquisitions which contain low counts,  $<2 \times 10^6$  in total, and investigations which demand a lower spatial resolution. A sharp filter is one which rolls-off late and decreases rapidly. It should be used with acquisition which contain high counts,  $>3 \times 10^6$  in total, and investigations that demand a higher spatial resolution<sup>40, 42</sup>.

The choice of filter function is crucial for determining both the noise and spatial resolution in the final image, the optimum filter being one which smoothes enough to suppress noise but not enough to cause significant degradation in spatial resolution. Over smoothing can obscure genuine abnormalities, while under-smoothing can complicate interpretation of the images because of excessive noise. When acquired count density is lower, statistical uncertainties will be relatively higher, and image noise can be reduced by

suppressing more of higher frequencies. Moreover, where the acquired count density is higher, less smoothing is needed.

Default values are usually established on the basis of research studies but it may be considered better to alter these in certain circumstances. However, such adjustments can easily result in image artifacts and therefore should be resisted unless experimental evaluation, perhaps using phantom data, has been undertaken<sup>40, 43</sup>. Cardiac phantom data were used to determine the “adjustments” required for the smoothing/filtering parameters in order to interpret the cardiac phantom PET data which is mentioned later (chapter 5) in this paper.

## **2.8 SPECT**

Single Photon Emission Computed Tomography (SPECT) is a routine procedure in most nuclear medicine departments today. There are radio-isotopes available that emit gamma rays directly upon decaying. A single photon is emitted which is detected by a special tomograph, commonly referred to as a *gamma camera*. Modern SPECT devices are usually based on the use of a rotating gamma camera. The camera has 5 basic layers:

- a) Collimator which only allows the gamma rays which are perpendicular to the plane of the camera to enter.
- b) Scintillation Detector which is used to detect the gamma photon. Sodium Iodide (NaI) detector crystal is generally used in gamma cameras.
- c) Photomultiplier Tubes (PMT) which are attached to the back of the crystal. The face of the PMT has a photocathode which, when stimulated by light photons, ejects electrons. The PMT detects and amplifies the electrons that are produced by

the photocathode. For an average of 7 to 10 photons incident on the photocathode, only 1 electron is generated. This electron from the cathode is focused on a dynode which absorbs this electron and re-emits many more electrons. This process is repeated over and over again in an array of dynodes. At the base of the PMT is an anode which attracts the final cluster of electrons and converts them into an electrical pulse.

- d) The Position logic circuits receive the electrical impulses from the PMTs in the summing matrix circuit (SMC). This allows the position circuits to determine the exact position of the scintillation event in the detector crystal.
- e) Data Analysis Computer, which receives and processes the incoming projection data into a readable image of the 3D spatial distribution of activity within the patient.

SPECT acquisition is performed by rotating or stepping the gamma camera around the patient while acquiring data into the digital matrix of a computer at all angles sampled. The most frequent use of SPECT is for studies of myocardial perfusion for assessing coronary artery disease (CAD) and heart muscle damage following infarction. The following figure shows the image volume which has been resliced into three different orientations as indicated by the schematics on the top of each image column (Figure 8). It is common to perform cardiac perfusion studies both under resting conditions and also following a “stress” to the heart created by exercise or by the injection of a drug that causes vasodilation. These are called rest/stress studies.

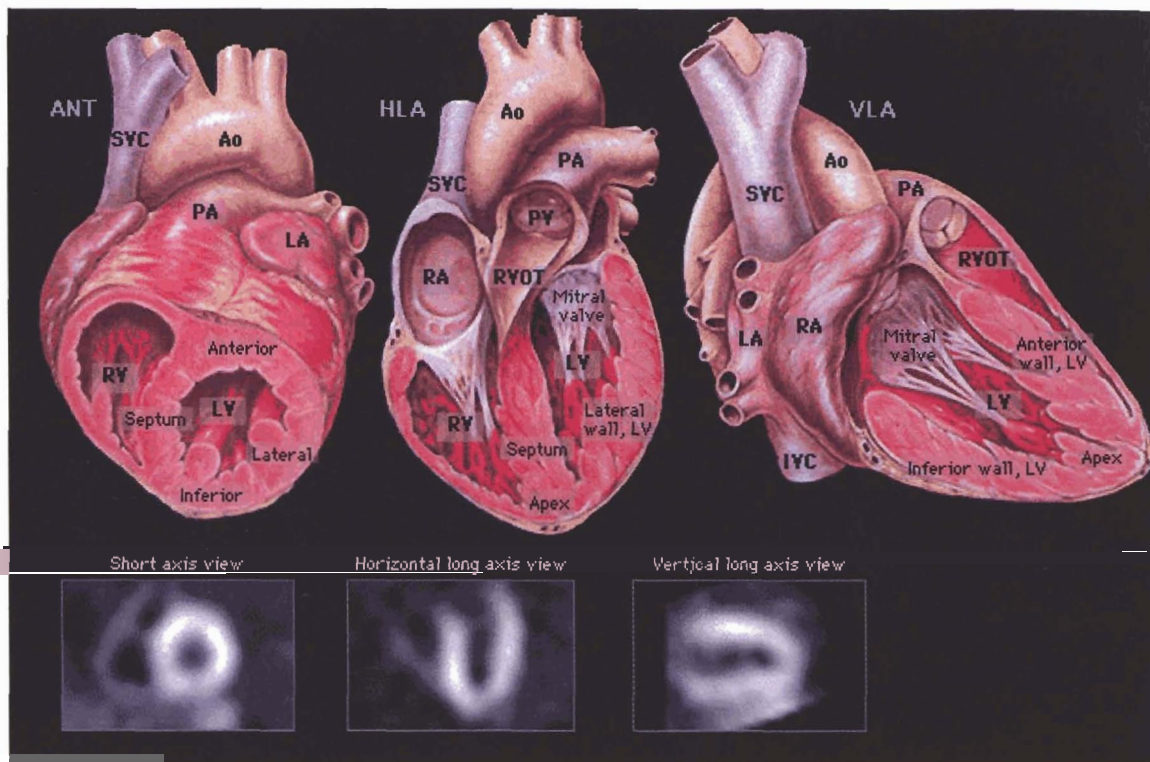


**Figure 8.** Nuclear myocardial perfusion tomograms using the radioactive compound technetium-99m sestamibi are shown compared to illustrations of the heart from similar views. Note that most of the myocardial wall activity arises from the left ventricular myocardium since it is considerably thicker (11 mm) than the right ventricular free wall (3 mm). The short axis tomogram shows the left ventricular myocardium as a donut shape while the vertical long axis and horizontal long axis tomograms display the myocardial wall as U-shaped structures. Image courtesy: <http://info.med.yale.edu>

## 2.9. PET vs. SPECT Revisited

Both SPECT and PET utilize radionuclide tracer techniques that produce images of the in vivo radionuclide distribution using measurements made with an external detector system. CT produces images anatomical information whereas both SPECT and PET provide organ function information. The functional information depicted in SPECT and PET images are dependent on the radiopharmaceutical employed for that particular study<sup>44</sup>. While SPECT allows for the noninvasive evaluation of myocardial blood flow by extractable tracers, the PET, on the other hand, allows for the noninvasive analysis of



regional blood flow, function and metabolism using physiological substrates prepared with positron-emitting isotopes of such elements as carbon and oxygen. The PET isotopes have half-lives that are considerably shorter than those used in SPECT and typically must be produced in close proximity to the scanner. Most medically important positron-emitting isotopes are produced using a cyclotron, and such a requirement is also a major limitation of PET implementation.  $^{82}\text{Rb}$  is an exception, which is produced using a generator in a similar manner as  $^{99\text{m}}\text{Tc}$ .

There are several advantages of PET over SPECT, apart from what has been already discussed in chapter 1, section 1.2. As mentioned earlier, non-uniform attenuation of photons between their point of emission within the patient and their escape from the body give rise to characteristic artifacts which particularly cause problems in myocardial perfusion SPECT<sup>21, 44, 45</sup>. In PET, the back-to-back nature of the emissions means that they can be accurately corrected using a separate measurement (transmission scan) of tissue attenuation. This transmission scan uses data from an external photon source, which rotates about the patient and can be routinely performed as part of the PET scan. This ensures that the cardiac PET images are free from attenuation artifacts as long as issues like patient motion can be kept under control.

Attenuation correction in SPECT has not been as successful as PET due to the fact that in PET, the total attenuation factor is the same along any given LOR irrespective of where the annihilation event occurred, because both back-to-back photons have to escape the body in order to be detected<sup>44</sup>. However in SPECT, photons originating from different depths within the patient will experience different levels of attenuation depending on their

position relative to the surface of the patient. There are instances where the SPECT studies wrongfully indicate heart conditions which are proved wrong when a PET study is conducted on the same patient (Figure 9, Figure 10).

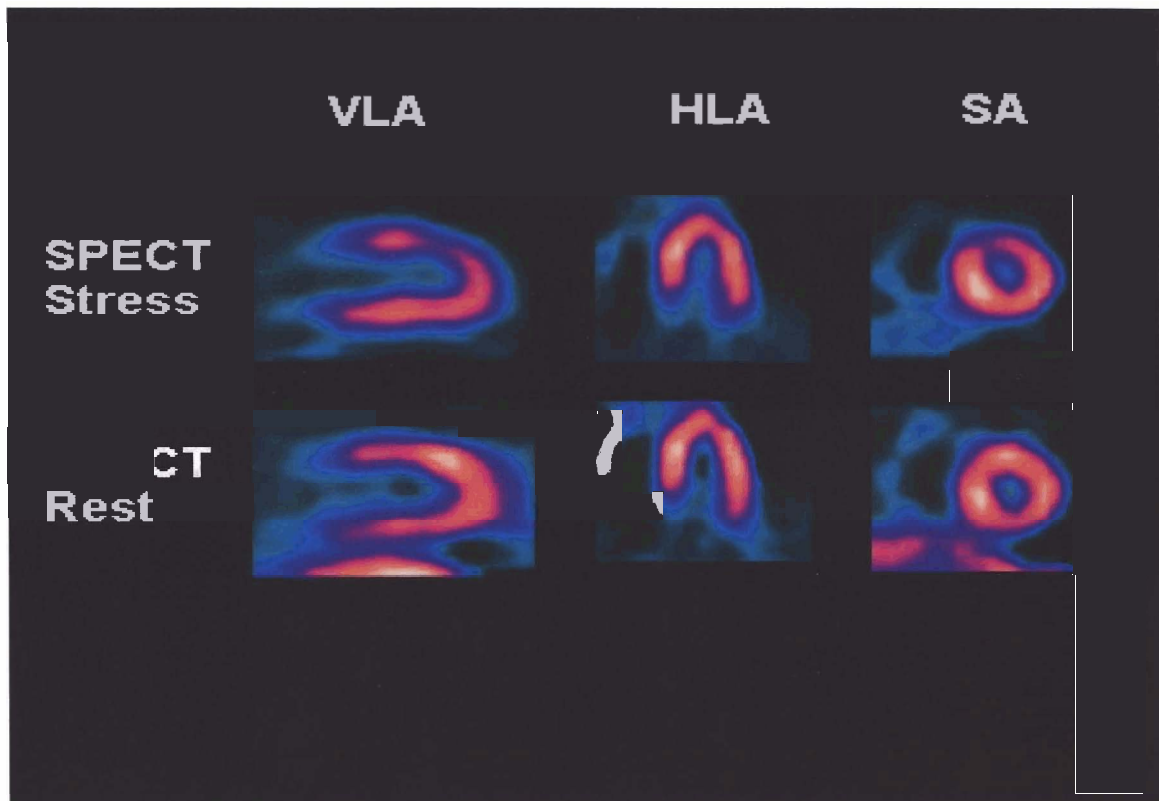


**Figure 9. Evidence of anterior wall ischemia on a SPECT Tc-99m sestamibi study in a 52 yr woman. Images courtesy of Dr. Josef Machac, Nuclear Medicine, The Mount Sinai School of Medicine of New York University, New York, NY, USA**

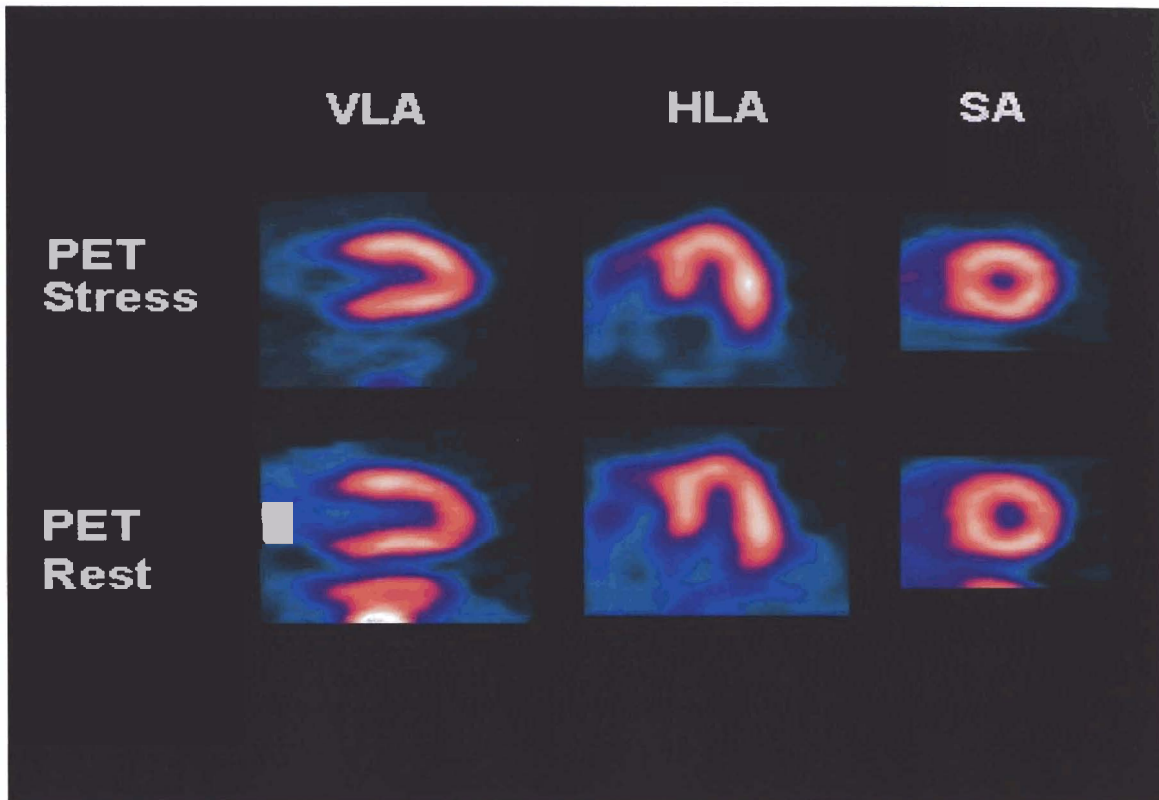


Figure 10. Normal Rb-82 PET study in the same patient. Images courtesy of Dr. Josef Machac, Nuclear Medicine, The Mount Sinai School of Medicine of New York University, New York, NY, USA

Since PET does not require a collimator like SPECT, the sensitivity is typically higher in PET. Higher sensitivity in PET also results in shorter acquisition periods which in turn enable many more counts to be acquired and eventually results in lesser noisy images. The SPECT cameras require time to rotate the detector heads about the patient whereas PET scanners are full-ring devices that simultaneously measure projections at all angles, which enable PET to image rapidly-changing processes, which, in turn, allow the possibility to quantify such things as myocardial perfusion in absolute as opposed to relative terms<sup>44</sup>.

The spatial resolution of PET is significantly better than that of SPECT (typically 5–7 mm with PET and 10–14 mm with SPECT). Furthermore, the resolution of SPECT detectors degrades rapidly with distance. This means that when the heart is viewed from one angle, the data can be recorded with much poorer resolution than from another leading to image distortion and nonuniformity. Although the spatial resolution of PET is generally better than SPECT, it is dependent on the distance traveled by the positron between its point of emission and annihilation in tissue. This distance is a function of the isotope concerned and is one of the reasons why  $^{82}\text{Rb}$  (PET myocardial blood flow tracer) images do not usually exhibit significantly higher resolution than corresponding SPECT images<sup>44</sup>.

The advantages discussed above imply that PET images are of higher quality than SPECT. In addition, most clinical PET scanners are full-ring devices that simultaneously measure projections at all angles, whereas SPECT cameras require time to rotate the detector heads about the patient. This is significant because it enables PET to image rapidly-changing processes, which, in turn, allows the possibility to quantify such things as myocardial perfusion in absolute as opposed to relative terms<sup>44</sup>.

## CHAPTER 3: Optimal Gated Image Acquisition Start Time for $^{82}\text{Rb}$ PET

### 3.1 Introduction

A major challenge of  $^{82}\text{Rb}$  PET imaging is determining when to begin the imaging in relation to the  $^{82}\text{Rb}$  tracer infusion. Many PET scanners are unable to simultaneously acquire data in gated and dynamic modes. So in order to acquire gated images (allowing for evaluation of wall motion and thickening); dynamic imaging can not be performed. As the infusion time is ~30- 60 seconds, depending on the age of the generator, and the short half-life, the infusion/imaging protocol is critical. Imaging too early results in images with high background (low contrast), and imaging too late results in noisy images due to low count statistics. The centers that currently use  $^{82}\text{Rb}$  PET use generalized parameters, but most centers end up having to individually tailor protocols to produce diagnostic images.

The current clinical protocol at VCUHS, as mentioned in chapter 1, involves a total of 4  $^{82}\text{Rb}$  studies (dynamic rest, gated rest, dynamic stress and gated stress study). During the dynamic studies 35 anatomic slices/time-point are acquired at 74 different time-points. The dynamically acquired images are reconstructed into 2590 images (35 slices  $\times$  74 time-points) and reviewed by the technologist to determine the first frame without significant blood pool activity in the ventricular cavity, and the time is recorded. A summed rest perfusion image (1 image = 35 slices) is created by summing all the images from that point

to the end. Then a separate gated acquisition is performed (8 frames per cardiac cycle), beginning data acquisition at the time determined from the previous resting dynamic study. Each frame has 35 slices and upon reconstruction, 280 images (8 frames  $\times$  35 slices) are obtained. This method facilitates acquisition of optimal gated images by eliminating the early images with higher background counts.

However, the optimal time post injection to begin the gated acquisition, so the composite image will routinely produce a diagnostic image, is not known. The start of data acquisition is commonly stated to occur at approximately 90–100 seconds after the infusion; however, to the best of our knowledge, the acquisition-starting time has not been systematically investigated.

Our goal was to evaluate the dynamic images in order to develop a standardized gated  $^{82}\text{Rb}$  PET imaging protocol where the optimal time post infusion to begin the gated acquisition is defined.

## **3.2 Methods and Materials**

### **3.2.1 GE Discovery LS PET/CT scanner**

This study involved the usage of the GE Discovery LS PET/CT (Figure 11) scanner (GE Medical Systems, Milwaukee, USA) which blends two essential and complementary imaging modalities into one scanner – positron emission tomography (PET) and computed tomography (CT). The PET scanner is a standard GE Advance Nxi scanner and it is combined with the GE Light Speed multi-slice CT system. The scanner can acquire 16 sub-millimeter slices in one rotation as fast as 0.5 sec scan speed. The PET scanner is placed behind the CT scanner and the table travel is extended to image the patient on each

machine in turn. The PET and CT images are registered by taking into account the distance between the two imaging planes. Two image sets are recorded in a single session and fused to form a single image that shows the anatomical location from CT along with the physiological/metabolic activity of the PET tracer administered. The CT provides high resolution, high contrast, and low noise, cross-sectional images which are not affected by the emission activity and can be obtained quickly using a fast helical scan. These CT images can be used in place of the PET rod source scan for attenuation correction of the PET emission activity. The CT images are viewed with the corresponding PET images to better localize the PET emission activity in the anatomical detail <sup>46</sup>.



**Figure 11. GE Discovery LS PET/CT camera**

The GE Advance PET scanner consists of one gantry containing 12,096 individual crystals arranged in 18 rings of 672 crystals each. The crystal type is bismuth germanate (BGO) (size: 4 mm transaxial, 8 mm axial and 30 mm radial). The inside diameter of the detector ring is 92.7 cm and the patient bore of the scanner is 59 cm. The 18 crystal rings form 35 two-dimensional imaging planes spaced by 4.25 mm. The scanner has a 15 cm

transaxial field of view and the coincidence window width is 12.5 nSec. The Advance Nxi is fitted with two high activity (10mCi maximum each)  $^{68}\text{Ge}$  ( $T_{1/2} = 273$  days) rod sources which can be used for transmission scanning and one normalization rod source (1.5mCi maximum). The system has tungsten septa 1 mm thick. The septa define the image planes in a two-dimensional scanning mode and are automatically retracted for three-dimensional scanning mode.

The Light Speed CT detector acquires sixteen 1.25 mm slices and is coupled to a four-slice data collection system, which can be configured for a range of simultaneous slice options from four 5 mm slices to four 1.25 mm slices. Fast patient scanning is achieved using four 5 mm slice acquisition and helical scanning with a pitch of 6, giving 30 mm of table travel per gantry rotation. The CT scanner can be used to acquire a projection image (scout view) which can be used to prescribe the axial scans.

The combination of the Advance Nxi and Light Speed CT is marketed as the Discovery LS. Patient attenuation can be measured with either the rod source or by using the CT scanner. The rod source scan measures the attenuation of the patient by counting the 511 keV gamma rays transmitted through the patient. The CT provides low noise images which are not affected by the emission activity and can be obtained quickly using a fast helical scan. The CT scale represents the body attenuation on an expanded scale which is calibrated to air and water. This CT scale is translated into an attenuation map for attenuation correction of the positron emission data <sup>47</sup>. Low dose CT scans have been shown to be adequate for the purpose of attenuation correction and localization of the PET emission activity <sup>48</sup>.



For two-dimensional imaging, the data are acquired and processed in one of two different modes according to the axial acceptance angle. The sinograms of direct planes acquired in the high-sensitivity mode include not only coincidence events from directly opposing crystals but also those from the two crossing planes of neighboring crystals. Whereas in the high-resolution mode, the direct slices include only events from directly opposing crystals. Moreover, sinograms for cross planes are similarly derived from events in four crossing planes for the high sensitivity mode, whereas only the two nearest crossing planes are utilized in the high-resolution mode. The standard acquisition mode in two-dimensional scanning is the high-sensitivity mode<sup>49</sup>.

The data maybe acquired as a static frame, a sequence of frames, or binned into dynamic frames using external gating. The minimum duration of a frame is 1 sec. Images can be reconstructed in 3 different sizes;  $64 \times 64$ ,  $128 \times 128$ , or  $256 \times 256$  pixel image. Image reconstruction for two-dimensional scanning uses an array processor for the filtered back-projection technique. Butterworth, Hanning and Shepp-Logan windows are available, as well as the ramp filter alone.

PET scanners have continued to improve since the initial development of a scanner that had a spatial resolution of approximately 2.5 cm and acquired a single image plane. The GE Advance Nxi PET scanner was put to test and results showed that the performance of the system was well suited for clinical research and applications<sup>49</sup>.

### **3.2.2 Cardiogen-82 (<sup>82</sup>Rb Generator)**

Absolute measurements of perfusion can also be made from the rate of tracer uptake using dynamic PET imaging<sup>50</sup>. To facilitate reproducible measurements, the tracer

should be introduced at a constant rate over a short period of time (30 s). Rubidium chloride  $^{82}\text{Rb}$  injection is a myocardial perfusion agent that is useful in distinguishing normal from abnormal myocardium in patients with suspected myocardial infarction.  $^{82}\text{Rb}$  is produced from an  $^{82}\text{Sr}/^{82}\text{Rb}$  generator and has a very short half-life (76 s). Therefore it requires direct intravenous infusion to the patient with an automated generator elution system <sup>51-53</sup>. The generator is an ion-exchange column of tin-oxide that binds the parent isotope  $^{82}\text{Sr}$  (25 day half-life) but not the daughter  $^{82}\text{Rb}$  resulting from  $^{82}\text{Sr}$  decay. Therefore  $^{82}\text{Rb}$  is eluted from the generator simply by flushing with 0.9% saline. In the generator column,  $^{82}\text{Rb}$  exists at equilibrium levels with  $^{82}\text{Sr}$  and regenerates within 10 minutes after elution, making this tracer convenient for rapid serial perfusion studies.

Cardiogen-82, which was used for our project, must be used with an infusion system specifically labeled for use with the generator (Cardiogen-82 Infusion System) and capable of accurate measurement and delivery of doses of rubidium chloride  $^{82}\text{Rb}$  injection not to exceed a single dose of 2220 MBq (60 mCi) at a rate of 50 mL/min (Figure 12).

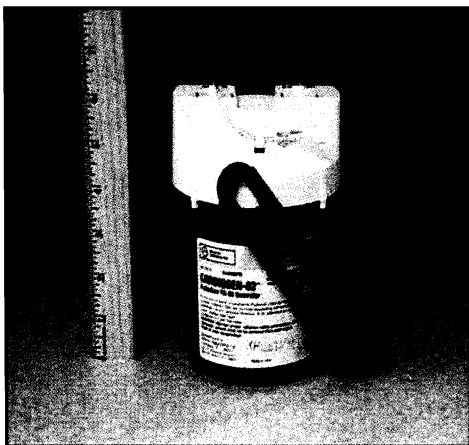


**Figure 12. CardioGen-82® (Rubidium (Rb-82) Generator).** Image Courtesy: Bracco Diagnostics USA ([www.bracco.com](http://www.bracco.com))

The infusion system is automated for the infusion and patient dose. The generator must be replaced every 28 days. The  $^{82}\text{Rb}$  dose is provided within 10 minutes. The infusion system permits accurate dosing with minimal operator interface, thus decreasing radiation exposure. It contains shielding vault for Cardiogen-82 generator and waste container. These performance characteristics reflect the conditions of use under which the drug development clinical trials were conducted <sup>54</sup>.

### **3.2.3 $^{82}\text{Rb}$ PET Patient Data Acquisition Procedure**

The patient data acquisition and processing procedure is divided into two different studies namely; a) Rest and Stress non-gated cardiac PET data acquisition and, b) Rest and Stress gated cardiac PET data acquisition.

The patient received an intravenous injection of  $^{82}\text{Rb}$  (mean =  $37 \pm 1.48$  mCi) through the Cardiogen-82 infusion system and a 2D emission acquisition of the chest was obtained. All dose evaluations and imaging acquisitions were performed with a PET/CT scanner (Discovery LS, GE Medical Systems, Milwaukee, WI, USA), which is able to acquire PET and CT data for the same patient in a single session. The PET scanner permits the simultaneous acquisition of 35 transaxial PET emission images with a slice thickness of 3.91mm (matrix size,  $128 \times 128$ ) over an axial field of view (FOV) of 15.3 cm.

First, a dynamic resting  $^{82}\text{Rb}$  acquisition was preformed. 74 frames were acquired in total with data acquired at 1 second per frame for the first 60 frames, 15 seconds per frame for the next 8 frames and 30 seconds per frame for the next 6 frames. A transmission scan was acquired for attenuation correction purposes. Short and long axis reconstructions were generated on the Octane workstation (Silicon

Graphics, Mountain View, CA), to determine the first frame without significant background activity and the time was recorded. At that point, the patient receives another intravenous injection of  $^{82}\text{Rb}$  (mean =  $37.4 \pm 0.14$  mCi) for the ECG rest-gated study. The data acquisition of the ECG-gated  $^{82}\text{Rb}$  PET image (8 frames per cardiac cycle) begins at the time recorded from the previous dynamic study.

Then the patient received a controlled IV infusion of dipyridamole, 0.56 mg/kg, with constant cardiac monitoring. Approximately 3 minutes after completing the dipyridamole infusion, the patient received  $^{82}\text{Rb}$  (mean =  $37.3 \pm 0.12$  mCi) followed by stress dynamic data acquisition. The optimal time point for accessing background clearance was determined as done for the rest study. A stress gated acquisition was then performed beginning at the predetermined time after beginning infusion.

### **3.2.4 $^{82}\text{Rb}$ PET Patient Data Processing**

#### **3.2.4.1 Image Reconstruction**

The acquired PET data were initially processed on an Octane workstation (Silicon Graphics, Mountain View, CA). Both dynamic rest and stress images, were reconstructed using OSEM iterative method (subsets = 28, iterations = 2). The FOV was set to 500 mm. The image data matrix was  $128 \times 128$ ; with a pixel size of 3.91 mm and a slice thickness of 3.91 mm. Attenuation correction was performed during image reconstruction. A total of 2590 (35 slices  $\times$  74 time points) images were generated during reconstruction (Figure 13). The dynamic rest and post-stress images were summed ( $128 \times 128$  matrices) using the GE image summation utility and named *summed rest* and *summed stress* respectively, for each patient. As mentioned in the last section, the reconstructed dynamic images were carefully

analyzed on the Octane workstation to determine the first frame without significant background activity and the time was recorded.

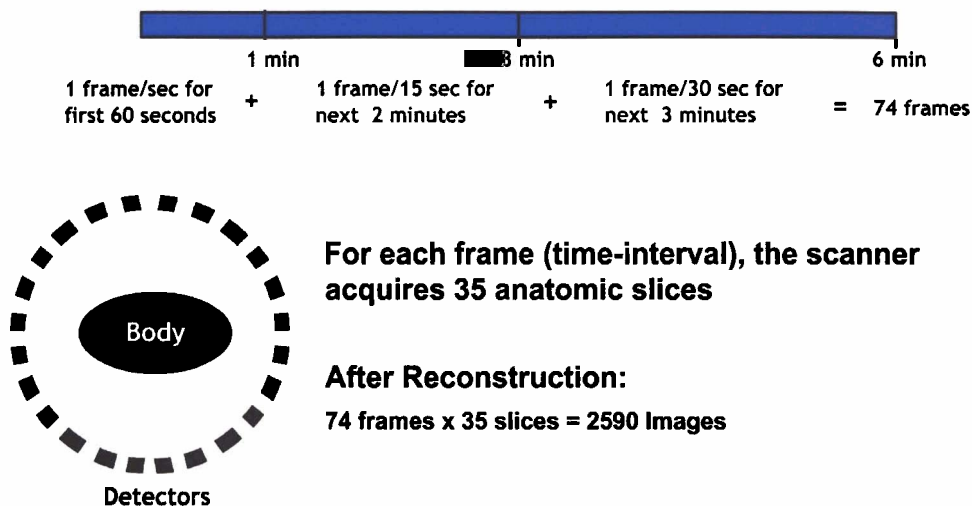


**Figure 13. Dynamic PET data acquisition procedure description**

Similarly, the gated rest and stress images ( $128 \times 128$  matrices) were reconstructed using OSEM iterative method (subsets = 28, iterations = 2). The FOV was set to 500 mm. Attenuation correction was performed during image reconstruction. A total of 280 (35 slices  $\times$  8 frames) images were generated during reconstruction.

The reconstructed data (gated rest and stress data) were transferred via network to the Siemens (e.soft workstation, Siemens Medical Solutions USA, Inc) computer for further analysis (Chapter 4, section 4.2.3.2). Gated images were processed using QGS 3.0 for cinematic display of myocardial wall motion/thickening and calculation of LV ejection fraction. The data processing in QGS has been explained in details in chapter 4 and

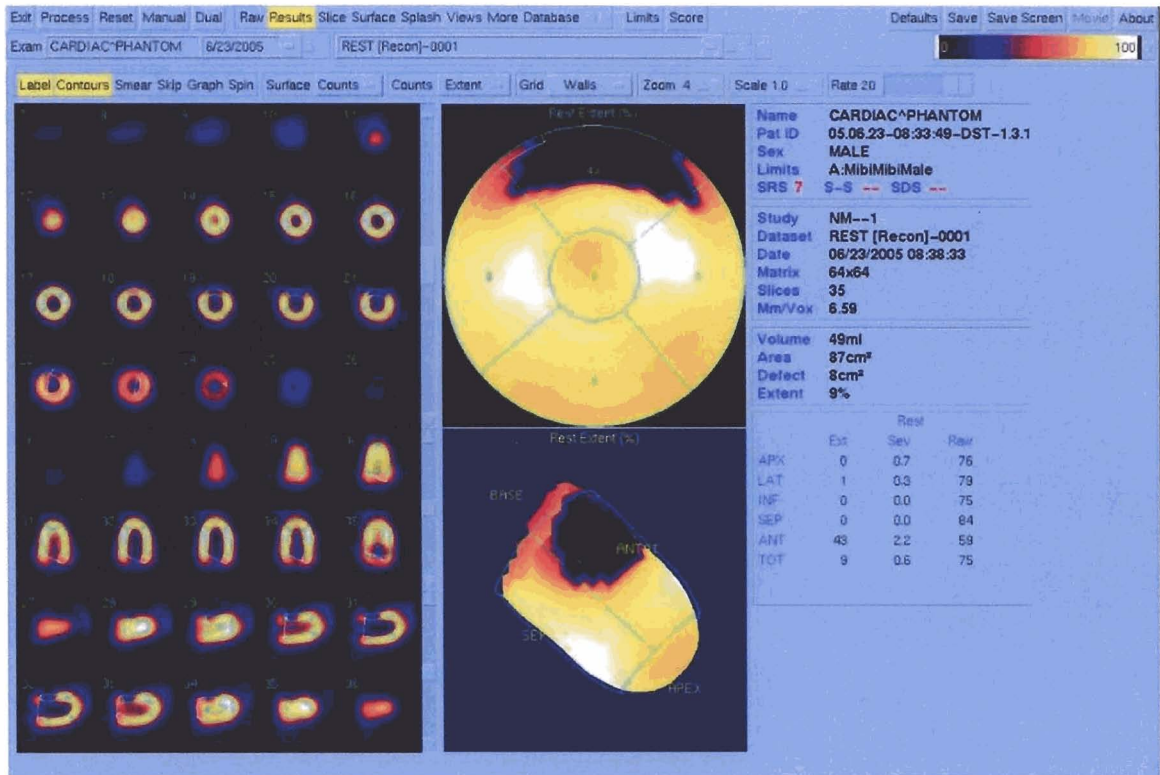


Figure 14. Quantitative display output for the Cedars-Sinai Quantitative Perfusion SPECT (QPS) program. The myocardial contours and percent abnormal for defect extent are presented.

The salient features of the algorithm are the following <sup>55</sup>:

- sampling of the myocardium based on an ellipsoidal model
- count profile between the endocardial and epicardial surfaces algorithm which is independent of myocardial shape, size and orientation, and establishes a standard 3-D point-to-point correspondence among sampled myocardial regions
- automatic generation of normal limit generation for any given patient population based upon data fractionally normalized to minimize hot spot artifacts

appendix C. Short and long axis tomographic images of the heart were computer generated using Quantitative Perfusion SPECT (QPS) 3.0 for the evaluation of myocardial perfusion.

#### **3.2.4.2 Quantitative Perfusion SPECT (QPS)**

QPS version 3.0 was used to analyze the non-gated (dynamic) data in this particular study (Figure 14). The Cedars Sinai Quantitative Perfusion SPECT program is an interactive standalone application for the automatic segmentation, quantification, analysis and display of static (non-gated) short axis myocardial perfusion SPECT data. QPS can automatically generate LV surfaces and valve plane, and also automatically generate optimal perfusion normal limits from a normal, a prospective and pilot patient population. Moreover, it provides 2-D display of stress and rest SPECT images in a single or dual-image mode. QPS automatically computes functional metrics including LV chamber volume and mid-myocardial surface area.

### **3.2.4.3 Measured Time Activity Curves**

The analysis of the data involved the usage of 3 software packages. WATSYN 5.4 and IDL (Interactive Data Language) 6.1, both products of Research Systems Inc. (RSI), were used to extract information from the DICOM data. This information was used to generate and interpret time activity curves (TAC) in Microsoft Excel 2003.

WATSYN is a fully integrated implementation platform for medical application development and the deployment is targeted at the mainstream medical industry. WATSYN 5.4 and IDL 6.1 were installed on a Windows XP Professional, Pentium 4 powered workstation. The summed dynamic images and the reconstructed data were exported from the PACS server. The dynamic summed images (rest and stress) were loaded into WATSYN, one series at a time for each patient, to review all the 35 slices. Three consecutive slices were selected which showed the least blood pool activity in the LV cavity. ROI (region of interest) were drawn over the upper and lower wall of the myocardium, inside the LV cavity, RV cavity, left and right lungs. The ROI information was saved as a '.sav' file to be applied on the reconstructed data later on in the study. Each patient had a total of 12 ROI files (6 each for the rest and stress study). After saving the ROI files, the dynamic reconstructed data for each patient was downloaded off the PACS server using WATSYN (Figure 15, Figure 16).



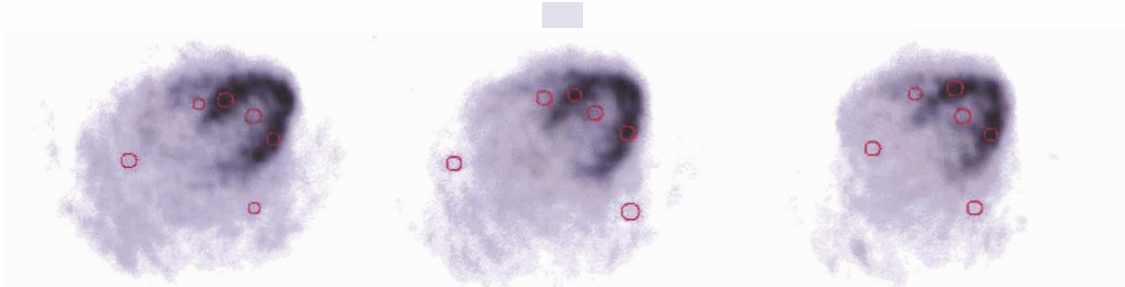


**Figure 15. Cardiac PET Dynamic Rest Images with ROIs; Frames 15, 16 and 17 out of 35 possible frames**



**Figure 16. Cardiac PET Dynamic Stress Images; Frames 15, 16 and 17 out of 35 possible frames.**

IDL 6.1 is the ideal software for data analysis, visualization, and cross-platform application development. Extensive image data manipulation capabilities and DICOM-support are the two key features that made this software perfect for our data analysis. An IDL code was developed (appendix A) to read and sort the reconstructed dynamic PET patient data (2590 slices). The saved ROI information for the 3 LV cavities in the summed images, were restored and applied on the reconstructed data and the maximum pixel information within the drawn ROI was written to an external text file. The same procedure was followed in order to retrieve the maximum pixel information for LV upper wall, LV lower wall, RV cavity, left and right lungs. The step-by-step description of the IDL code

developed for this study is available in Appendix A. The data processing procedure for the rest and stress studies were identical.

We used Microsoft Excel 2003 to export the maximum pixel information from the text files. The mean of the maximum pixel for each frame was calculated and used to determine the standard uptake value (SUV). The SUV is a way of quantifying radioactivity uptake on a PET scan. The SUV is calculated with a mathematical equation that divides the mean activity within a region of interest (in mCi/mL) by the injected dose per unit body volume, weight, or area (in mCi/kg) <sup>56</sup>. The measured time activity curve or TAC (time vs. SUV) was generated for each patient in resting and post-stress state (Figure 17, Figure 18, Figure 19, Figure 20).

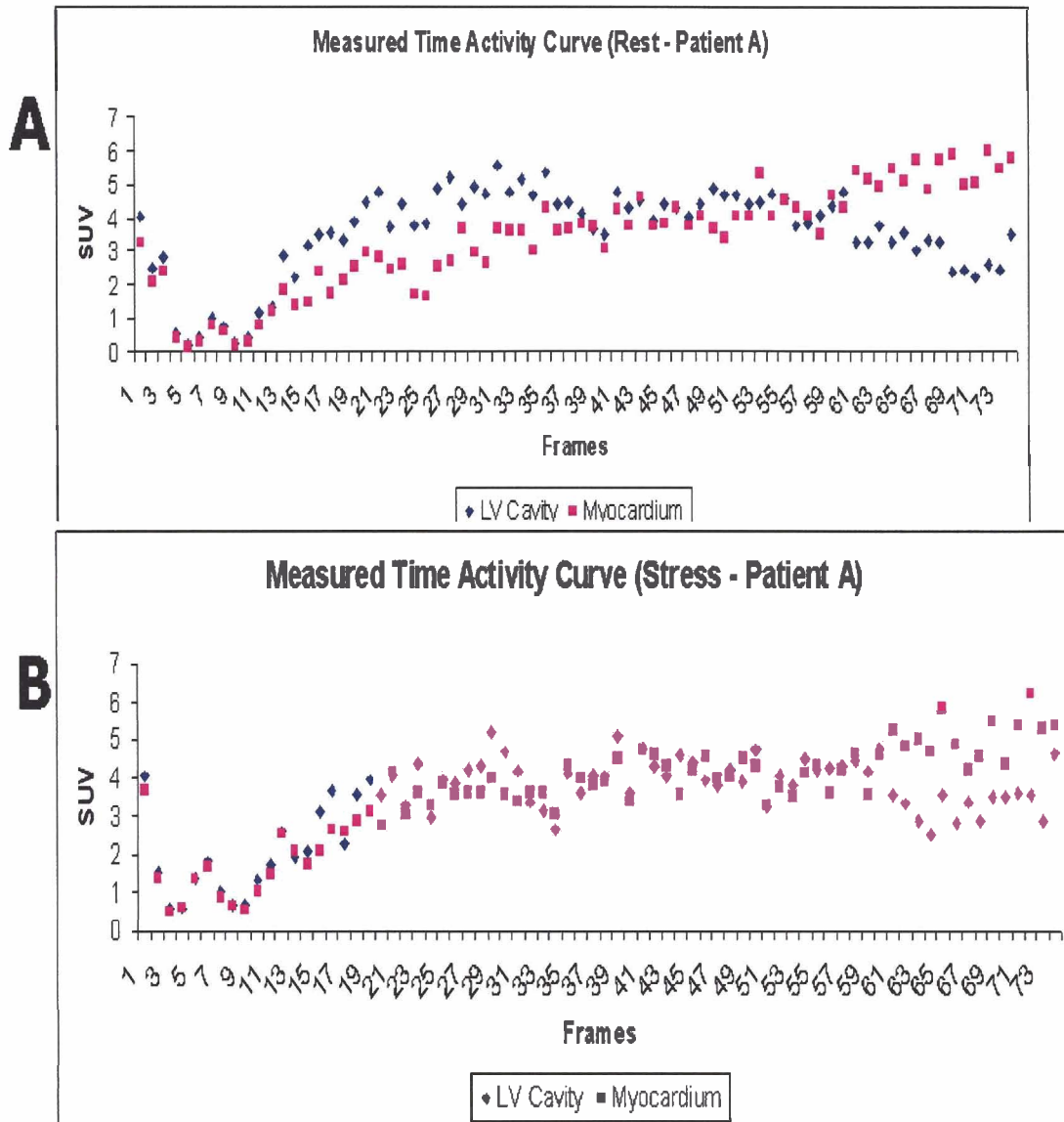
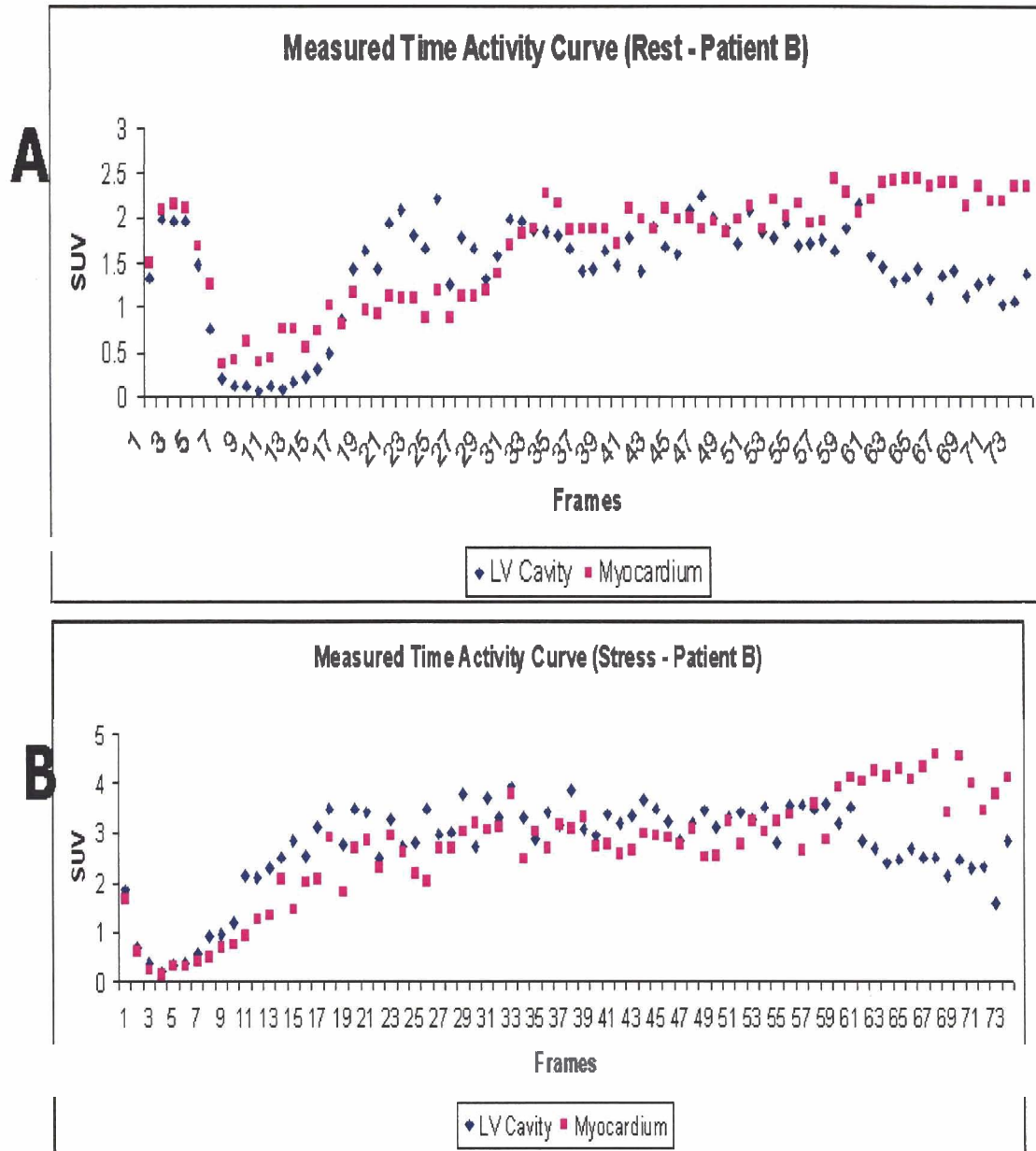


Figure 17. Measured Time Activity Curves - Patient A: Dynamic Rest Spilt Time = 60 seconds, Dynamic Stress Spilt Time = 60 seconds



**Figure 18. Measured Time Activity Curves - Patient B: Dynamic Rest Spilt Time = 60 seconds, Dynamic Stress Spilt Time = 75 seconds**

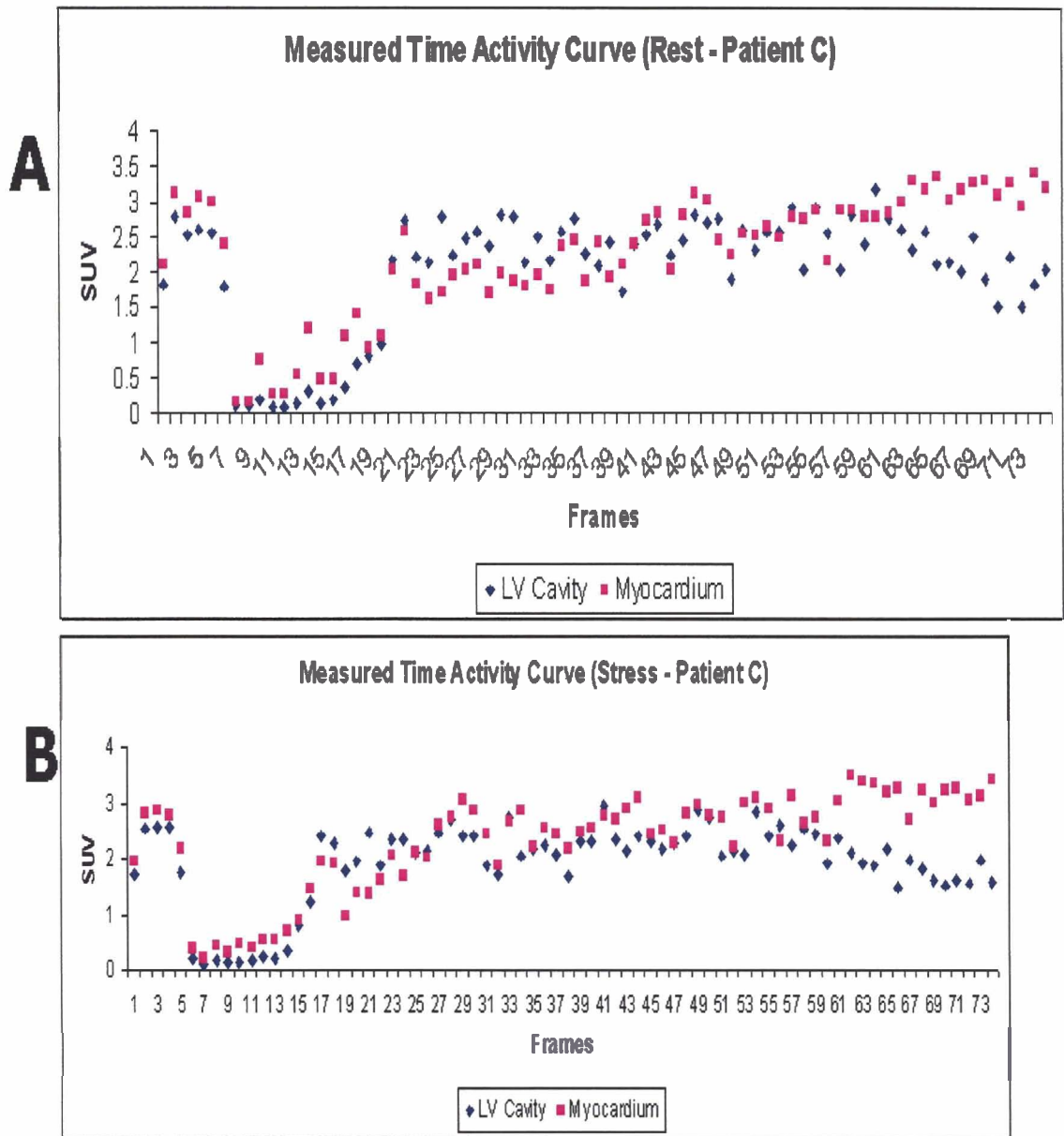
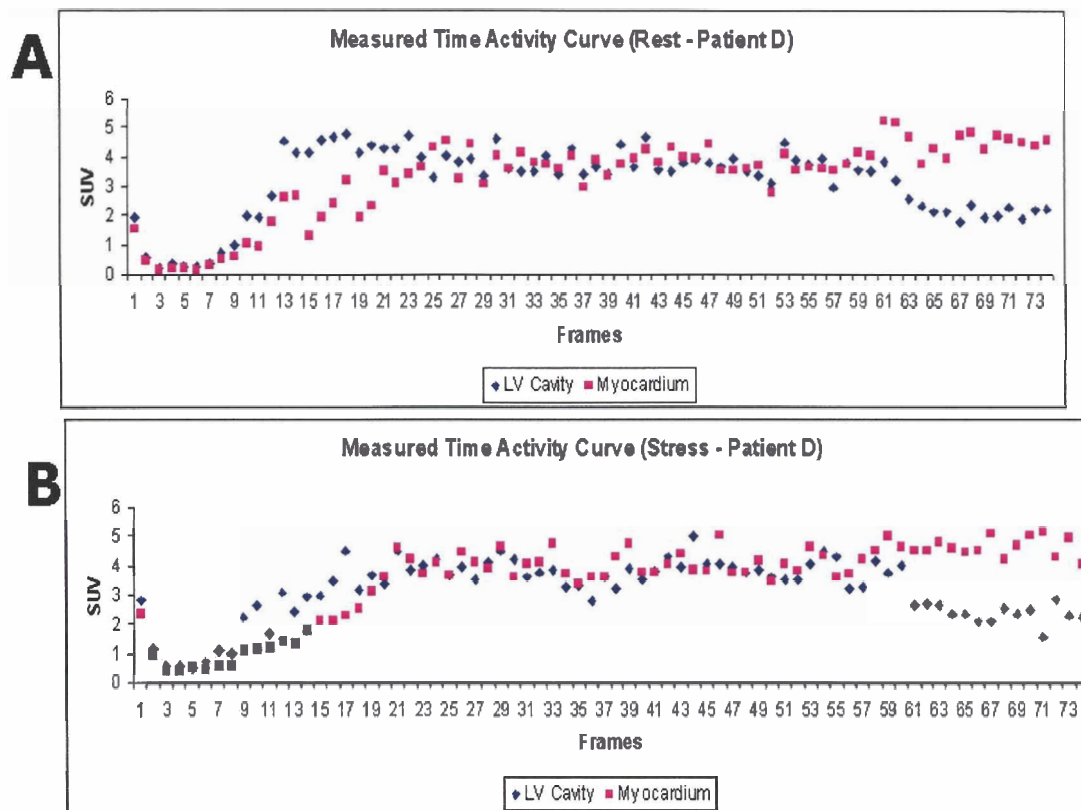
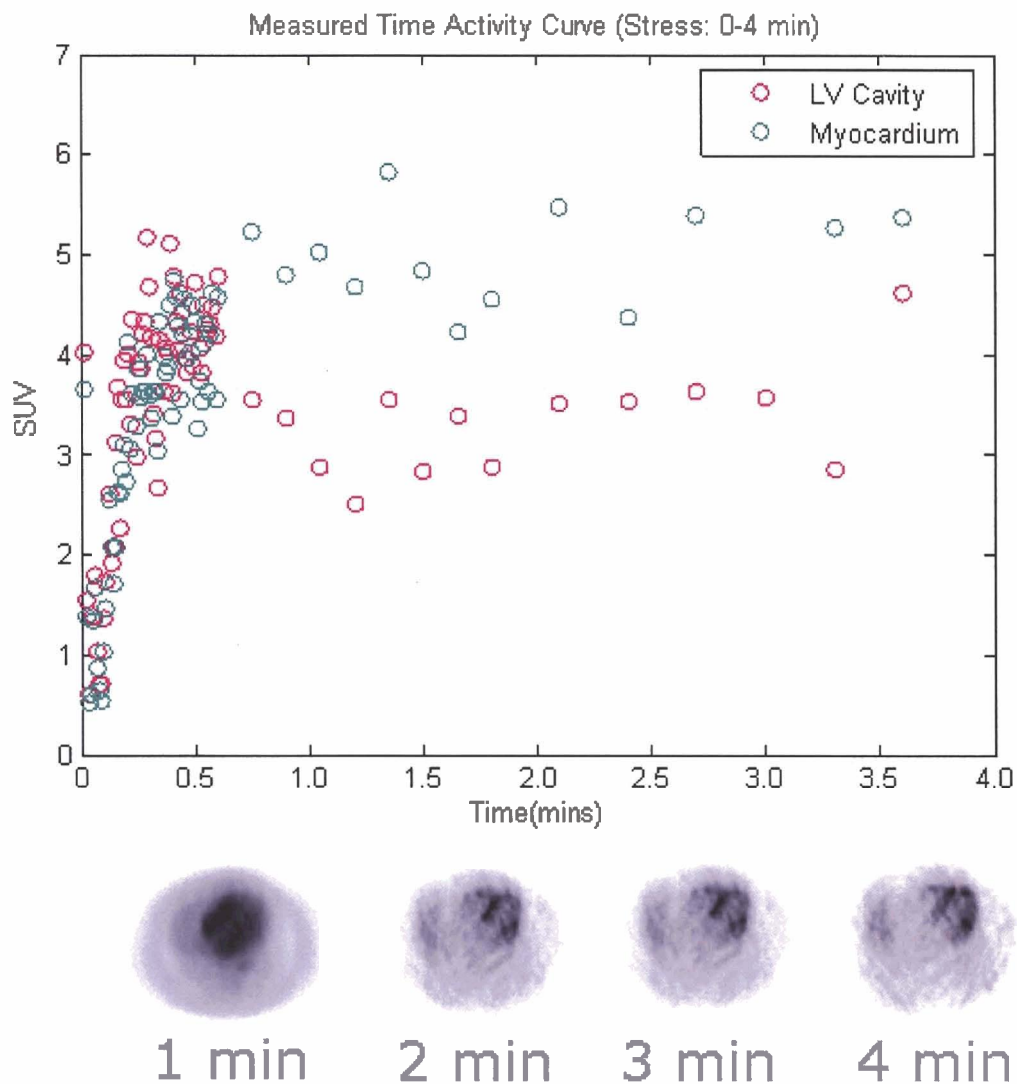


Figure 19. Measured Time Activity Curves - Patient C: Dynamic Rest Spilt Time = 75 seconds, Dynamic Stress Spilt Time = 60 seconds



**Figure 20. Measured Time Activity Curves - Patient D: Dynamic Rest Spilt Time = 75 seconds, Dynamic Stress Spilt Time = 60 seconds**

As mentioned in section 3.2.4.1, the first 60 frames were acquired at 1 sec/frame, the next 8 at 15 sec/frame and the last 6 at 30 sec/frame. The measured time activity curves shown below clearly demonstrate the activity in myocardium and LV cavity over the span of 74 frames or 6 minutes. It was observed that there was lot of background activity in both LV cavity and myocardium during the first minute of acquisition (Figure 21). Around 60-75 seconds into the acquisition, the blood pool activity in the LV cavity is cleared and the images start looking better. It was at this very instance that the activity curve of LV cavity and the myocardium split, as myocardium uptakes the activity. This trend was followed in both rest and stress studies for all the patients that were studied.



**Figure 21. Measured Time Activity Curves - 1st four minutes during vasodilator-induced stress.** After the 1st minute, the two curves split with the LV cavity curve going down and myocardium curve going up. The corresponding screenshots show the same frame (12) after 1 min, 2 min, 3 min and 4 min of data acquisition. The image at 1st minute is blurry due to high level of background activity. The image becomes clearer after the second minute.

#### 3.2.4.4. Infusion Time Activity Curves

The infusion cart prints out the activity uptake information at each second throughout the infusion period. The infusion time activity curves were generated for all the patients in both rest and stress studies (Figure 22).

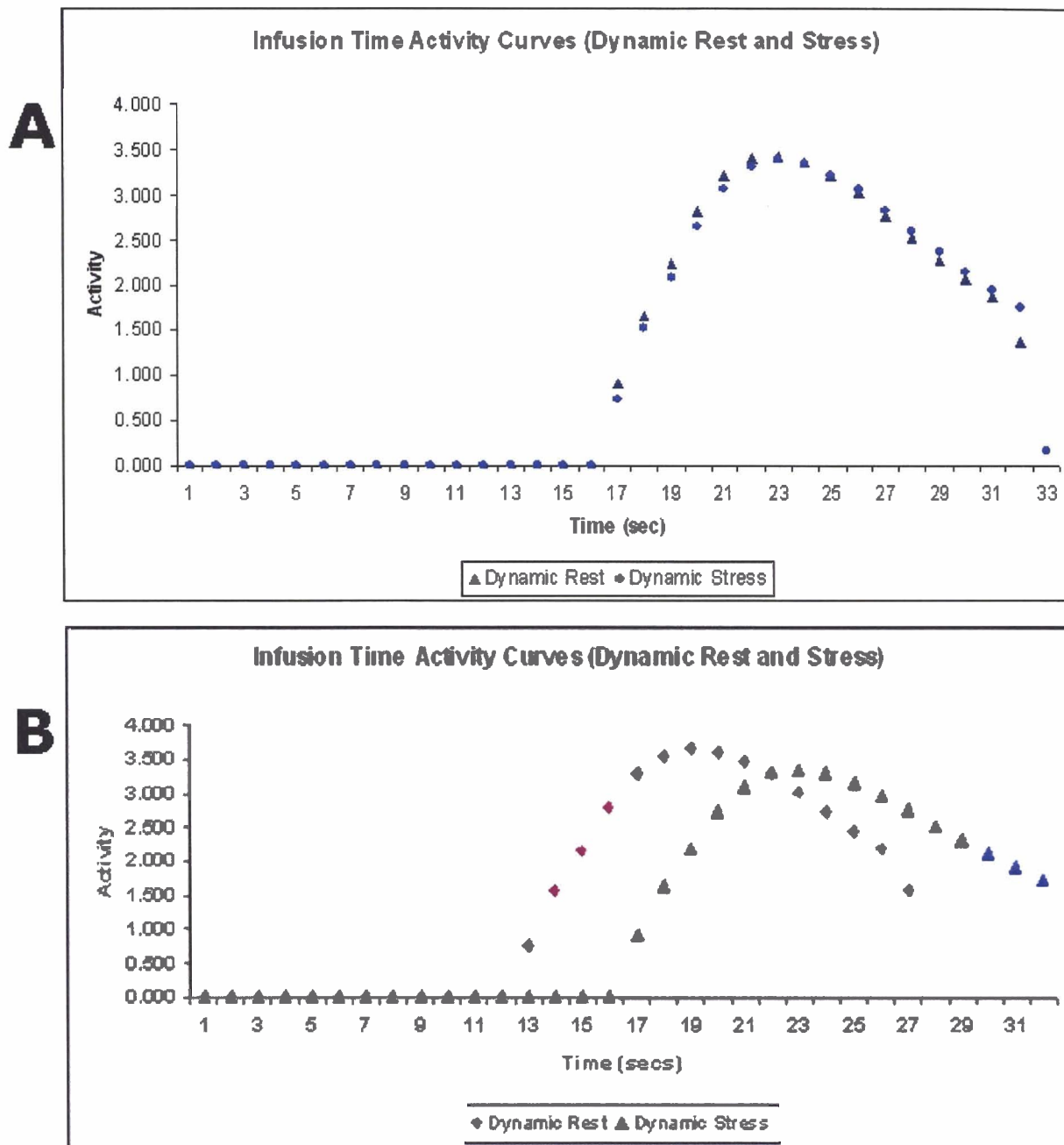


Figure 22. Infusion Time Activity Curves - Dynamic Rest and Dynamic Stress

### 3.2.5. $^{82}\text{Rb}$ PET Patient Data Analysis

The maximum activity in the LV cavity and the corresponding full width half maximum (FWHM) values are determined. Through visual inspection of the measured LV



cavity curve, a time point (in seconds) is determined when the activity in the blood in LV cavity clears, which can be identified by a clear split between the myocardium curve activity ( $\uparrow$ ) and the LV cavity activity ( $\downarrow$ ) curve which till this point were almost equal. This time point is called the *splitting time* (ST). Again, through visual inspection of the measured LV cavity curve, we determined two time points  $\leq$  FWHM, one *before splitting time* (BST) and one *after splitting time* (AST). The *Estimated Infusion Time* (EIT) was calculated as shown below:

$$EIT(\text{seconds}) = AST - BST$$

Similarly, through visual inspection of the infusion activity curves at rest and persantine-induced stress state, two time points  $\leq$  FWHM were determined, one *before peak activity* (BPA) and one *after peak activity* (APA). The *Actual Infusion Time* (AIT) was calculated as shown below:

$$AIT(\text{seconds}) = APA - BPA$$

All these parameters were correlated with each other to isolate the dominant parameter in determining image quality as discussed in section 3.3.1.

### 3.2.6. Statistical Analysis

Data are presented as mean value  $\pm$  1SD. Linear regression analysis and determination of the standard error of estimation (SEE) were used to compare the data. Paired Student *t* test was used to determine significant difference, defined as  $P < 0.05$ . All the statistical studies were performed in JMP software (SAS Institute Inc., NC, USA).

### 3.3. Results

The initial population included 17 (11 women, 6 men) patients. The mean age of the patients was  $63 \pm 10$  years (range, 48 to 79 years). Of these, the printouts from the infusion cart were not available for seven patients. So a comparison study was not possible for these patients. Stress PET study data for three patients were not available. Thus, the final patient population included in the present analysis consisted of 7 patients. 85 % of the total population had known history of CAD.

#### 3.3.1. Overall Correlation of Infusion Time and Splitting Time

The correlation (Table 3.1) of EIT with AIT in rest state in all  $n=6$  patients was excellent and positive ( $r = 0.93$ ,  $P = 0.006$ ). However, the correlation of EIT with AIT in stress state was very poor and negative ( $r = -0.63$ ,  $P = 0.184$ ). There was a good correlation between ST (rest) and ST (stress).

Table 3.1: Correlation of various parameters in Infusion Time and Splitting Time

<b>Time</b>	<b><i>r</i></b>	<b>SEE</b>	<b><i>P</i></b>
<b>EIT vs. AIT (Rest)</b>	0.93	14.35	0.006
<b>EIT vs. AIT (Stress)</b>	-0.63	27.97	0.184
<b>EIT (Rest) vs. EIT (Stress)</b>	0.01	41.24	0.986
<b>AIT (Rest) vs. AIT (Stress)</b>	0.76	0.72	0.086
<b>ST (Rest) vs. ST (Stress)</b>	0.74	6.61	0.097
<b>EIT vs. ST (Rest)</b>	0.67	30.57	0.145
<b>EIT vs. ST (Stress)</b>	-0.14	35.49	0.784
<b>AIT vs. ST (Rest)</b>	0.71	0.78	0.121
<b>AIT vs. ST (Stress)</b>	0.84	0.54	0.039

Variability in the measured infusion time was noted with each study (rest and stress). This variability was greatest in the stress studies, where the shortest and longest measured infusion times differed by as much as 87 seconds. Despite this variation, the

mean ST at stress was not shown to be statistically different ( $t = 1.38$ ,  $df = 6$ ,  $P = 0.23$ ) from the mean ST at rest (mean  $\pm$  SD,  $60\% \pm 0.82\%$  vs.  $64\% \pm 8.72\%$ ). There was no correlation between EIT (rest) and EIT (stress). The correlation between EIT and ST, and AIT and ST in rest state was fair where as in stress state the results varied drastically. As seen in Table 3.1, the results looked promising in the rest state where as the stress state results did not show a consistent trait.

### 3.3.2. Hemodynamic Findings

Table 3.1 lists heart rate and blood pressure at rest and during DIP-stress in the study. There was a decrease in the mean systolic blood pressure ( $-8.2\% \pm 9.1\%$ ) and the mean diastolic blood pressure ( $-15.9\% \pm 5.2\%$ ) for the patients during the DIP-induced stress state. However, the heart rate was higher during stress ( $36.9\% \pm 13\%$ ).

Table 3.2: Hemodynamic Findings

Patient	Rest			Stress		
	Systolic Pressure	Diastolic Pressure	Heart Rate	Systolic Pressure	Diastolic Pressure	Heart Rate
1	186	63	53	152	54	65
2	140	75	76	135	67	104
3	104	62	65	104	56	96
4	141	86	78	140	70	118
5	115	57	51	114	44	62
6	114	60	48	89	47	72
7	135	75	50	119	65	64

### 3.4. Discussion

The aim of the study was to evaluate the dynamic images in order to develop a standardized gated  $^{82}\text{Rb}$  PET imaging protocol where the optimal time post infusion to begin the gated acquisition is already known. If the optimal time to begin imaging were

known, only the 2 gated studies would need to be performed; thus reducing the total radiation exposure and imaging time.

Towards the end of the month, the generator takes longer than normal to infuse the bolus, which in turn delays/extends the process of bolus clearance. The infusion cart was programmed to cut down the total length of infusion to 30 seconds in order to determine whether it is the age of the generator or the patient's physical characteristics (patient weight, LVEF) that influences the image acquisition start time.

No singular pre-defined time to begin gated imaging was established based on these study results. This may be due to the inconsistency in the DIP-induced stress state results. As seen in the results above, EIT, AIT, and ST, correlated fairly well against each other in rest state. However, the correlation for the same parameters in stress-induced state was very poor and negative. One explanation for this drastic variability can be that, according to the norm, we started image acquisition during the peak affect of Persantine, which is 2 minutes after infusion. Unlike the resting state, the actual hemodynamics of the heart is unknown during this Persantine induced dilation, and it may be patient specific.

This study has couple of limitations. The low sample size ( $n = 7$ ) could have influenced the results. The fact that generator aging results in prolonged infusion times later in the month may play a role in the inability to accurately identify a single time point at which to begin the gated image. Another limitation is that the hemodynamic conditions and, by inference, myocardial blood flow might not have been the same the first 2 minutes of the dynamic image acquisition (i.e. the actual effects of Persantine on the hemodynamics at that time may have varied from patient to patient).

## **CHAPTER 4 Comparison of $^{82}\text{Rb}$ gated PET LVEF using QGS with $^{99\text{m}}\text{Tc}$ First Pass Radionuclide Angiography (FPRNA) LVEF**

### **4.1. Introduction**

Resting left ventricular ejection fraction (LVEF) is the most widely used clinical index for assessing the prognosis in patients with known or suspected coronary artery disease (CAD) <sup>57</sup>. There are different methods of automatic LVEF quantification which have been discussed in the past. For example, DePuey et al. used manual drawing of endocardial surfaces at 34% of the maximum count level and calculated LVEF using Simpson's rule<sup>58, 59</sup>. Nichols et al. eventually automated DePuey and colleagues' method for evaluating LVEF <sup>60</sup>. Electrocardiographically gated (ECG) SPECT, a primary diagnostic technique in CAD, allows myocardial perfusion imaging with subsequent analysis of regional wall motion, regional wall thickening, and calculation of LVEF <sup>61-63</sup>. Resting LVEF is routinely evaluated clinical on ECG gated SPECT myocardial perfusion imaging (MPI) studies with  $^{99\text{m}}\text{Tc}$  agents using a quantitative gated SPECT (QGS) program developed by Germano et al <sup>61</sup>. Previous reports have shown the gated SPECT LVEF to correlate with FPRNA<sup>64, 65</sup>. Gated  $^{82}\text{Rb}$  PET MPI also permits the evaluation of wall motion and thickening, and calculation of LVEF; however given the differences in acquisition hardware, attenuation correction and radionuclide energy, it cannot be assumed that the QGS results for  $^{82}\text{Rb}$  would be the same as those obtained with  $^{99\text{m}}\text{Tc}$  MPI<sup>44, 66</sup>. To

evaluate this, we obtained a resting FPRNA, resting and post dipyridimole (DIP) stress gated  $^{82}\text{Rb}$  MPIs on 17 patients presenting for evaluation of possible myocardium at ischemic risk. Using QGS program, we obtained LVEF, End Diastolic Volume (EDV) and End Systolic Volume (ESV) on the rest and post DIP stress MPI images and compared those to results obtained from FPRNA technique.

## **4.2 Methods and Materials**

### **4.2.1 Patient Studies**

The initial population included 17 (11 women, 6 men) patients. The mean age of the patients was  $63 \pm 10$  years (range, 48 to 79 years). Of these, a resting first pass radionuclide angiogram (FPRNA) study was not performed in three patients in whom right antecubital IV access was not possible. The raw gated PET study data for one patient was not available. Thus, the final patient population included in the present analysis consisted of 13 patients.

### **4.2.2 First Pass Radionuclide Angiography (FPRNA)**

Researchers use an imaging technique called radionuclide angiography (RNA) to assess the heart's pumping capability by measurement of ejection fraction (EF) and cardiac wall motion. Inadequate blood-flow in the coronary arteries, prior damage to the heart muscle, or heart failure are some of the conditions that can produce impaired function. As mentioned earlier, LVEF is a good clinical indicator of left ventricular systolic function. Conceptually, estimation is made of the volume of blood in the ventricle at the end of diastole (on left) and the volume of blood remaining in the ventricle at the end of systole (on right) (Figure 23). A bolus of radiotracer is injected into the patient, and the transit of

bolus through the chambers of the heart is imaged. The FPRNA studies were performed during the injections of  $^{99m}\text{Tc}$  DTPA using a multi-crystal gamma camera (SIM-400).

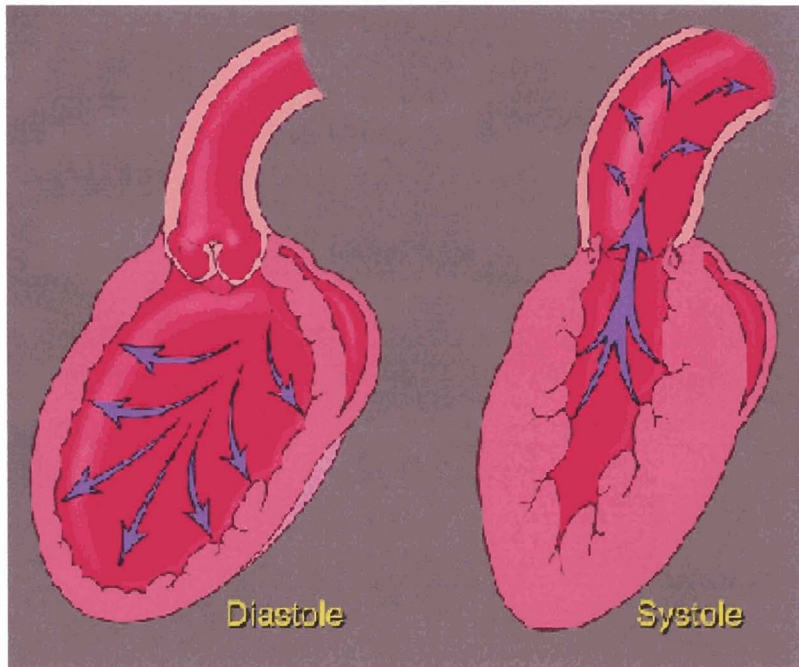


**Figure 23.** Left: Diastole is when a chamber of heart (atria or ventricle) is relaxing (expanding in size) and, Right: Systole is when heart (atria or ventricle) is contracting to pump the blood out. Images courtesy of Robert J. Luchi, MD, Baylor College of Medicine (<http://www.hcoa.org/hcoacme/chf-cme/chf00048.htm>)

The SIM-400 is a device for digitally imaging gamma radiation in the energy range of 30 to 300 keV and for analyzing, displaying and recording data at rates of up to 100 images per second. The SIM-400 is specialized for both invasive and non-invasive nuclear cardiology and has software to perform first pass tests at rest and during stress, gated equilibrium studies, myocardial perfusion imaging and myocardial blood flow studies. The SIM-400 system consists of a mobile multicrystal NaI (TI) detector attached by a fiber optic link to a Macintosh computer. The detector head is essentially the “camera” of the

SIM-400 system. When the face of the detector head is positioned close to a patient's chest, the detector detects the gamma rays which emanate from the injected radionuclide and sends the raw data to the frame processor. The detector head is comprised of:

- Lead collimator(s),
- Sodium iodide (NaI) crystal cut into 400 detection elements,
- 115 photomultiplier tubes (PMTs) with corresponding PMT modules and a PMT interface board, and
- Detector electronics.

An external cable transmits data and high voltage between the detector head and the frame processor. A 0.25-inch lead shield surrounds all but the face of the detector to ensure that the only radiation entering the detector is through the collimator holes. This shielding is sufficient to stop at least 95% of all gamma cameras up to 300 keV which is more than adequate for the emissions by the commonly used radionuclide.

All the patients underwent FPRNA in fasting state. In FPRNA, the radioactive agent is injected rapidly into a vein in the arm as a bolus and images are collected only during the first transit of the bolus through the cardiopulmonary system. Patients had an IV placed. If venous access was possible in the right antecubical fossa, then the patient received an IV bolus injection of  $^{99m}\text{Tc}$  DTPA (mean = 21.8 mCi) and underwent a FPRNA test only at rest for this study. The administration must be very rapid, and the



FWHM of the bolus in the superior vena cava, should be <1 s and, if possible, <0.5 s. The anterior projection images were obtained in the upright position at rest. Data acquisition consists of a continuous stream of images from the detector (the duration of each image in this study was 25 milliseconds for 1500 frames)<sup>67, 68</sup>. The frame duration should be varied to suit the heart rate, but a standard 25 ms is usually used unless the heart rate is very high, >150 min<sup>-1</sup>, or the diastolic function is of particular interest, in which case, a duration of 10-20 × 10<sup>-3</sup> s should be used. Using special software, SIM 400 v 4.3.4.PPC, the Macintosh analyzes, displays, and stores acquired study data.

### 4.2.3 Data Analysis

#### 4.2.3.1 First Pass Data Processing:

First-pass provides ejection fraction of either ventricle by application of the equation:

$$EF = \frac{\text{ED counts} - \text{ES counts}}{\text{ED counts} - \text{BKG counts}}$$

where ED is end diastole, ES is end systole, and BKG is background.

For this calculation, relative volumes are defined by the count densities within the ventricular regions of interest. Absolute left ventricular volumes can be defined from first pass studies by outlining the left ventricle and performing geometric calculations. During the first-pass studies, isotopic labeling of the cardiac-chamber blood occurs sequentially. Hence, labeling of the right ventricle is temporally separated from that of the left ventricle. Since the right ventricular and left ventricular blood-pool labeling is temporally separated, the time-activity curve has two distinct areas of maximal oscillation.

As mentioned earlier, the acquired data were computer processed, for cinematic display of LV wall motion and calculation of cardiac functional parameters, by Macintosh-based software called SIM 400 v 4.3.4.PPC. The software is wholly controlled by inputs received from the function keys (F1, F2,.....,F12) on the keyboard. The mouse input is only required to manually draw ROIs. The step-by-step description of the whole procedure is mentioned in appendix B.

#### **4.2.3.2 Quantitative Gated SPECT (QGS)**

QGS was developed for the analysis of gated SPECT images and assesses LVEF, wall motion and wall thickening<sup>61,69-71</sup>. QGS has been used in routine clinical practice, for the past decade, to assess myocardial perfusion and calculate ventricular function<sup>71</sup>. The QGS software, which was developed by Germano et al. at the Cedars Sinai Medical Center, displays 2-D and 3-D Gated Myocardial Perfusion data, and allows automated computer calculation of Left Ventricular Volumes and Left Ventricular Ejection Fraction (LVEF)<sup>61</sup>. In brief, QGS segments the myocardium based on LV short-axis images. Endocardial and epicardial surfaces are determined based on count profiles which are fitted to asymmetric Gaussian curves. Using myocardial size, shape and location criteria, surface points can be determined even in regions without apparent radioactivity uptake. These calculations are performed for each measured gate resulting in a determination of the myocardial surfaces as a function of the cardiac-cycle. The largest and smallest LV volumes are defined as *end-diastole* and *end-systole* from which the LVEF is calculated (Figure 24)<sup>66</sup>. We applied this program to gated PET data without any changes or preprocessing, except for translation of the data (DICOM PET modality) to the required

input format (DICOM Nuclear Medicine modality). The step-by-step description of the whole procedure is mentioned in appendix C.

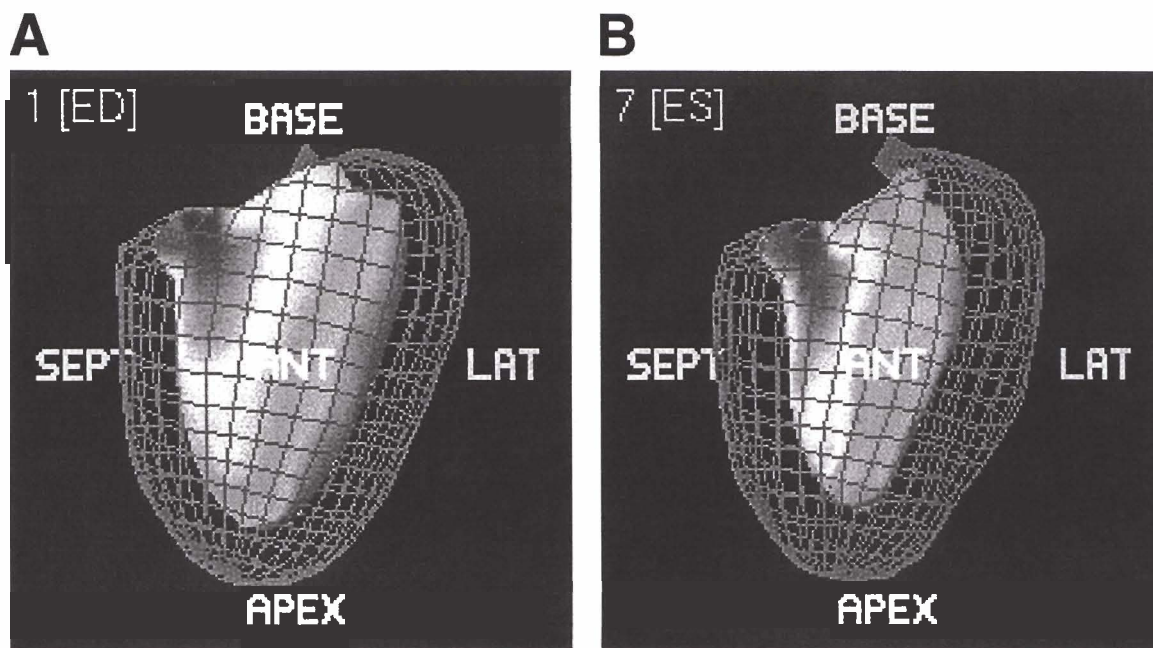


**Figure 24.** Images from QGS of end-diastolic (A) and end-systolic (B) phases showing epicardial and endocardial borders of the left ventricle. SEPT = septal; LAT = lateral. Images courtesy of Slart, R. H. J. A. et al. from Department of Nuclear medicine, Groningen University Medical Center, Groningen, The Netherlands.

The QGS software package also has a “constrain mode,” which restricts the search volume (contours) of the algorithm and excludes extra-cardiac activity. This alternate mode is used when the automatic left ventricular contour-detection appears visually to be incorrect (i.e. includes adjacent extracardiac activity).

#### 4.2.4 Statistical Analysis

Data are presented as mean value  $\pm$  1SD. An LVEF value of 45% or more was considered normal. Linear regression analysis and determination of the standard error of

estimation (SEE) were used to compare the data. Paired Student *t* test was used to determine significant difference, defined as  $P < 0.05$ .

### 4.3 Results

Complete data sets from 11 women (65 %) and 6 men (35%) were available for analysis. There were 11 patients (65%) with known CAD. With perfusion imaging, 4 patients (24%) had normal results and 11 patients (65%) had either complete or partial reversibility of stress perfusion defects.

#### 4.3.1 Overall Correlation of QGS LVEF and FPRNA LVEF

The correlation of LVEF (Figure 25) determined by means of FPRNA with Rest QGS in all  $n=13$  patients was good and positive ( $r = 0.81$ ,  $P = 0.0008$ ). The mean LVEF obtained by QGS was lower than that obtained by means of FPRNA (mean  $\pm$  SD,  $51\% \pm 13.00\%$  vs.  $61\% \pm 9.57\%$ ,  $P = 0.0005$ ).

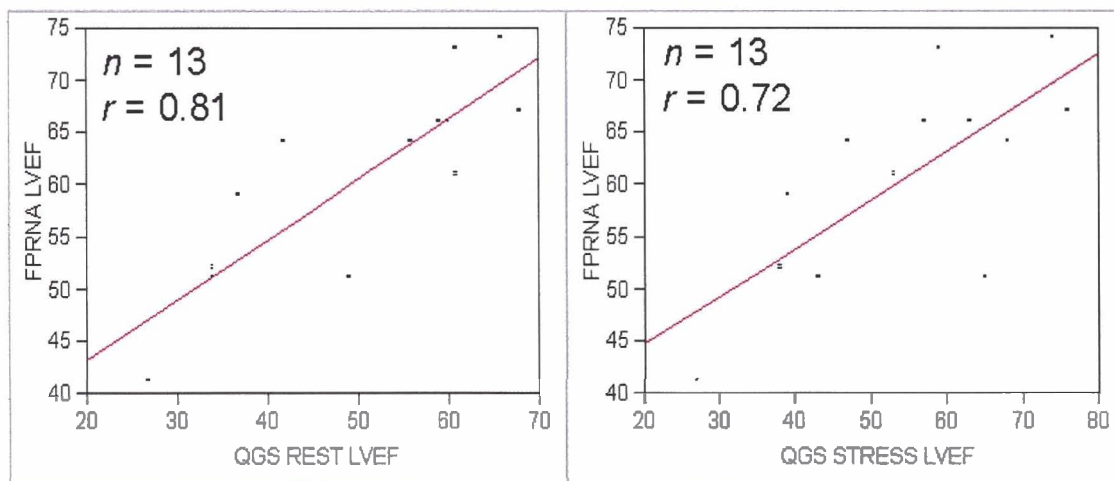


**Figure 25.** Correlation between rest FPRNA LVEF and rest QGS LVEF in 13 patient studies (A) and correlation between rest FPRNA LVEF and stress QGS LVEF in 13 patient studies (B).

The correlation of LVEF determined by means of FPRNA with post stress QGS was slightly lower ( $r = 0.72$ ,  $P = 0.005$ ). The mean LVEF obtained by QGS post stress was significantly lower than that obtained by means of FPRNA ( $55\% \pm 14.98\%$  vs.  $61\% \pm 9.57\%$ ,  $P < 0.05$ ). The summary of the data obtained is as shown below:

Table 4.1: Comparison of LVEF Measured from First-Pass Radionuclide Angiography (FPRNA) and Quantitative Electrocardiographic-Gated SPECT (QGS)

<b>Summary</b>	<b>n</b>	<b>Mean</b>	<b>SD</b>	<b>95 % CI</b>	
<b>First Pass LVEF</b>	13	60.69	9.57	52.81	64.58
<b>QGS Rest LVEF</b>	16	51.50	13.83	44.12	58.87
<b>QGS Stress LVEF</b>	13	54.53	14.98	47.24	61.75

#### 4.3.2 Rest and Post-Stress QGS LVEF

The overall correlation between QGS LVEF derived from post-stress and rest studies in the same patient was excellent ( $n=16$ ,  $r=0.92$ ,  $P<0.0001$ ). We were not able to detect a statistical difference between the mean QGS rest ( $55\% \pm 14.98\%$ ) and post-stress LVEF ( $51\% \pm 13.00\%$ ) values ( $t = -2.08$ ,  $df = 15$ ,  $p\text{-value} = 0.06$ ). After applying the correction equation previously shown to describe the relationship between FPRNA and QGS SPECT data in patient studies acquired with high dose injection, no significant difference ( $t=1.18$ ,  $df = 11$ ,  $p=0.26$ ) between the mean QGS resting PET values and the mean FPRNA LVEF values was detected<sup>64</sup>. The correction equation is shown below:

$$y = 0.87x + 2.55$$

where,  $y = \text{QGS LVEF (rest)}$  and  $x = \text{FPRNA LVEF (rest)}$ <sup>64</sup>.

### 4.3.3 Reproducibility of Measured Data

We checked the interobserver reproducibility of the data from FPRNA and QGS (Figure 26) in all patients. EDV and ESV values were given in ml and LVEF values were given in percentage format. EDV, ESV and LVEF obtained with FPRNA showed a good correlation between two independent observers ( $r = 0.89$ ,  $r = 0.76$ ,  $r = 0.88$  respectively). The EDV, ESV and LVEF obtained with QGS also showed a strong correlation between two independent observers ( $r = 0.97$ ,  $r = 0.96$  and  $r = 0.74$  respectively).

Table 4.2: Reproducibility of Data Measured from First-Pass Radionuclide Angiography (FPRNA) and Quantitative Electrocardiographic-Gated SPECT (QGS)

	Scatter plots			
	<i>r</i>	Regression equation	SEE	<i>P</i>
FPRNA EDV				
Interobserver	0.89	$y = -21.04 + 1.20x$	21.53	<0.0001
FPRNA ESV				
Interobserver	0.76	$y = 17.40 + 0.69x$	19.39	0.002
FPRNA LVEF				
Interobserver	0.88	$y = 10.1 + 0.87x$	4.80	<0.0001
QGS EDV				
Interobserver	0.97	$y = 10.08 + 0.85x$	10.00	<0.0001
QGS ESV				
Interobserver	0.96	$y = 1.78 + 0.89x$	8.83	< 0.0001
QGS LVEF				
Interobserver	0.74	$y = 18.55 + 0.67x$	9.00	0.0015

EDV = end-diastolic volume; ESV = end-systolic volume; LVEF = left ventricular ejection fraction

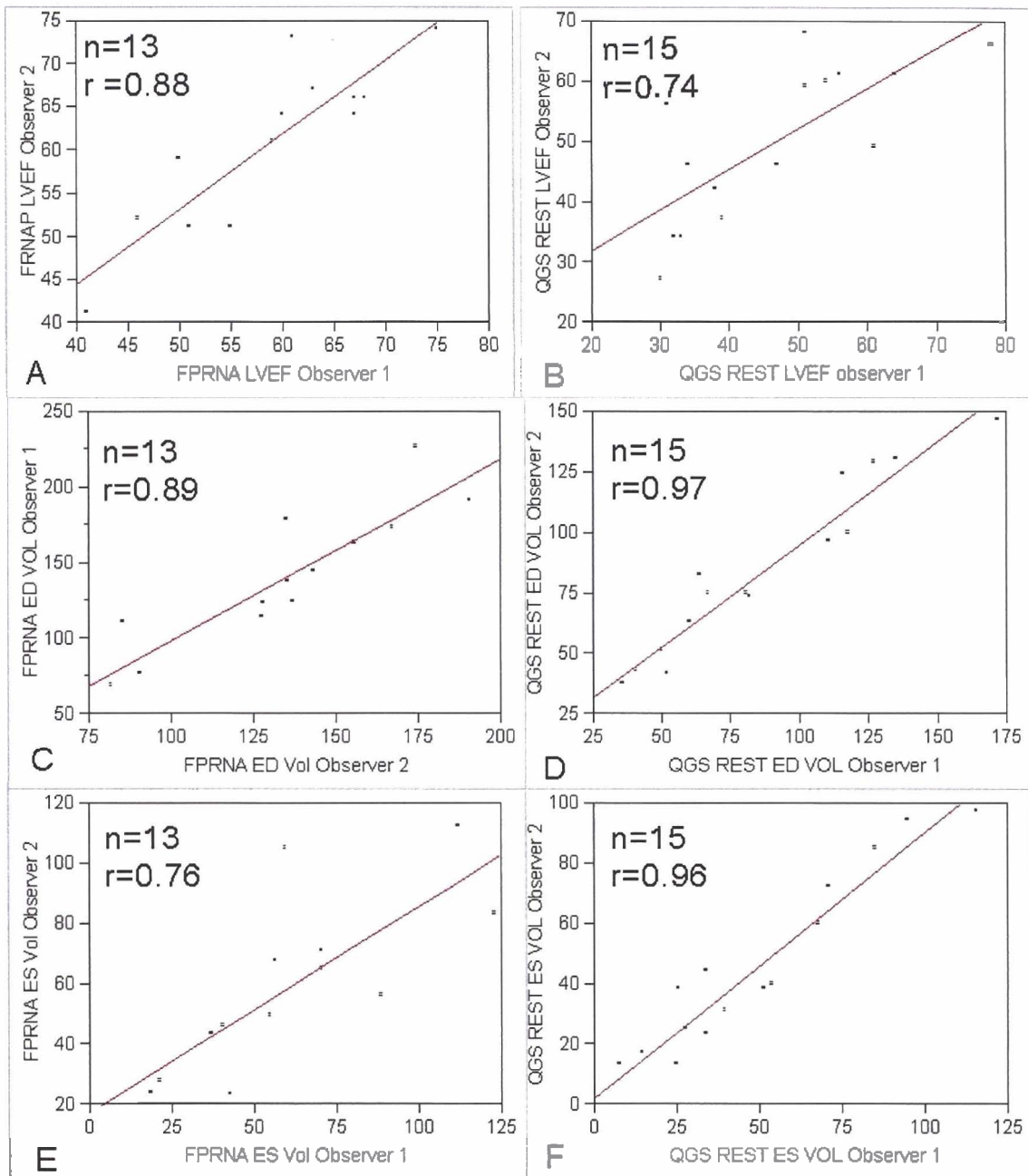


**Figure 26. Comparison of left ventricular ejection fraction (LVEF) (A,B), end-diastolic volume (EDV) (C,D) and end-systolic volume (ESV) (E,F) between two observers. Left panels show scatter plots for FPRNA data and right panels show scatter plots for QGS data.**

## Discussion

LV function and perfusion can be assessed either by FPRNA method or by ECG-gated acquisition of myocardial images. FPRNA was used as a gold standard for LVEF in this study which included a relatively small unselected group of patients ( $n=17$ ) with a wide range of LVEF values and perfusion defects. The patients underwent studies of good technical quality based on standard protocol. Similar to the previous clinical study where QGS SPECT-derived LVEF was compared with rest FPRNA<sup>64</sup>, the overall correlation between resting PET QGS and FPRNA LVEF was good ( $r = 0.81$ ,  $p < 0.001$ ,  $SEE=5.86\%$ ). There was a slightly lower correlation between stress PET QGS and FPRNA LVEFs ( $r=0.72$ ,  $p < 0.005$ ,  $SEE = 6.88\%$ ).

In an earlier study<sup>65</sup>, it was observed that the reproducibility of first-pass generated EDV, ESV and LVEF values were not as good as those generated by QGS. It was concluded that QGS reproducibility was better than FPRNA because FPRNA has limitations that include manual region of interest (ROI) drawing and uncertainty regarding the valve plane location whereas the QGS program is fully automated<sup>65</sup>. Although the FPRNA processing is well standardized, the software is not fully automated as mentioned above. Due to errors or inconsistencies in the selection of background activity, the selection of included beats, and the delineation of valve plane, variability in calculated LVEF may occur<sup>64</sup>. Hence, the FPRNA generated-LVEF values determined by an experienced technologist (observer 1), who took these technical aspects into consideration, were used in this study to minimize level of variability in the calculated LVEF.



In a previous study, the correlation of interobserver (observer 1 vs. observer 2) LVEF reproducibility of QGS data were better than FPRNA (0.99 vs. 0.91)<sup>64</sup>. In our study, 42% of the cases had extracardiac activity and the ‘automated mode’ of the QGS software failed to identify the appropriate cardiac contour in all those cases. Hence, the boundaries were manually adjusted and ‘constrain mode’ was used in these 7 cases. Due to the low number of samples  $n=17$ , we were unable to separate these cases from the total sample size. It is probably due to this very reason that the correlation of interobserver LVEF reproducibility of QGS PET data was lower than FPRNA (0.74 vs. 0.88). High cardiac activity significantly affected the accuracy of QGS as a means of determining LVEF. The QGS algorithm is based on myocardial contour detection<sup>72</sup>. All the functional parameters are determined on the basis of the detected edges/myocardial contours. Achtert et al demonstrated, in phantom studies, a significant underestimation of LVEF with the constrained mode of the QGS software in images with high extra cardiac activity<sup>64, 73</sup>. Underestimation of LVEF values could have affected the correlations in our study. Since the scattered photons degrade the image quality and contaminate the LV contour, scatter correction might, in the future, improve the accuracy of edge detection with QGS<sup>64, 74, 75</sup>.

Another possible limitation of our study is that all the studies were acquired with 8-frames per R-R interval. Limited temporal resolution has also been shown to cause underestimation of LVEF<sup>62, 64</sup>.

#### **4.5 Conclusion**

QGS-derived LVEF from <sup>82</sup>Rb gated PET data may be useful in assessing functional parameters (myocardial perfusion) despite the difference in radionuclide energy

and camera technology. However there appear to be limitations to the technique similar to the gated SPECT data. LVEF may be slightly underestimated in comparison with FPRNA, and high extracardiac activity of the LV significantly affects the accuracy of the QGS PET LVEF.

## **CHAPTER 5 Determination of Post Filtering Parameters for Accurate Defect Size Determination in a Cardiac Phantom using $^{99m}\text{Tc}$ , $^{18}\text{F}$ , and $^{124}\text{I}$**

### **5.1 Introduction**

For distinguishing viable from scarred myocardium in patients with severe coronary artery disease and left ventricular dysfunction in whom coronary revascularization is under consideration,  $^{18}\text{F}$ -FDG PET is an accurate, noninvasive diagnostic technique<sup>7</sup>.  $^{18}\text{F}$  is the most commonly used radioisotope at the VCUHS PET center. Studies have already been done to prove that the improved contrast resolution of PET improves sensitivity and specificity and a more confident identification of defects when compared to SPECT studies<sup>1</sup>.  $^{82}\text{Rb}$  PET myocardial perfusion imaging provides improved specificity compared with  $^{201}\text{Tl}$  SPECT for identifying coronary artery disease, most likely due to the higher photon energy (Table 2.1) of  $^{82}\text{Rb}$  and attenuation correction provided by PET<sup>2</sup>.  $^{99m}\text{Tc}$  agents,  $^{18}\text{F}$ -FDG, and  $^{82}\text{Rb}$  can all be used for cardiac imaging<sup>1-7</sup>. However, count rates, energy and camera differences can yield image differences that are independent of the actual biological distribution.

The aim of the study was to investigate whether PET with an  $^{82}\text{Rb}$ -labeled tracer would provide information on defect size similar to that provided by  $^{99m}\text{Tc}$  SPECT, using a cardiac phantom in which the true defect size is known. The under-perfused section of the heart is known as a *defect*. Since  $^{82}\text{Rb}$  has such a short half-life (76 seconds), filling and

imaging a phantom would be a great challenge. Hence  $^{124}\text{I}$ , which is a high-energy radioisotope like  $^{82}\text{Rb}$  (table 2.1), was used in this comparison study as a surrogate for  $^{82}\text{Rb}$ . Static cardiac phantom data acquisitions were performed with and without defects using  $^{99\text{m}}\text{Tc}$ ,  $^{18}\text{F}$ -FDG and  $^{124}\text{I}$ -labeled tracers.  $^{99\text{m}}\text{Tc}$  SPECT was considered as the gold standard for this study, as it is the most widely used technique for myocardial perfusion imaging. The image quality obtained by  $^{99\text{m}}\text{Tc}$  myocardial perfusion imaging is satisfactory for clinical diagnosis. So the clinically implemented filtering (Butterworth filter, cutoff = 0.55, order=7) and data processing (QGS, QPS workflows) parameters for  $^{99\text{m}}\text{Tc}$  SPECT were kept constant. The  $^{99\text{m}}\text{Tc}$  percent defect size was measured using various thresholds of the maximum volume pixel using IDL (appendix D) and compared with the true defect size. The threshold at which the measured defect size matched the true defect size for the  $^{99\text{m}}\text{Tc}$  data was obtained. The  $^{18}\text{F}$  and  $^{124}\text{I}$  data were smoothed until the defect size approached the true defect size at the threshold determined earlier for  $^{99\text{m}}\text{Tc}$  data. Smoothing the  $^{18}\text{F}$  and  $^{124}\text{I}$  PET data would compromise the advantage of higher image resolution/quality over  $^{99\text{m}}\text{Tc}$  SPECT data. The aim was not to get better imaging quality but to take advantage of the dependable attenuation correction feature in PET modality. As mentioned in chapter 1, attenuation correction in PET results in much more accurate clinical diagnosis by reducing the number of false-positive SPECT scans.

## **5.2 Methods and Materials**

This study involved the usage of the GE Discovery LS PET/CT scanner (GE Medical Systems, Milwaukee, USA), which has been described in details in Chapter 3, for the  $^{18}\text{F}$ -FDG and  $^{124}\text{I}$  PET studies. The  $^{99\text{m}}\text{Tc}$  SPECT cardiac static phantom study was

performed on the Siemens E.CAM dual-head variable-angle gamma camera system (Siemens Medical Systems, USA).

### **5.2.1 Siemens E.CAM Dual-Head Variable-Angle Gamma Camera System**

The E.CAM gamma camera offers optimized imaging capabilities at all energies. The proprietary, energy-independent HD<sup>3</sup> digital detectors deliver consistent, high performance for single isotopes, dual isotopes and multipeak isotopes. The variable-angle gamma camera used in this study allows for 180°, 90° and 76° detector positions to optimize system sensitivity and throughput for every acquisition type. The system's full range of motion, including caudal/cephalic tilt, offers full clinical utility for general purpose, neurology, cardiology and oncology studies.

The FOV is 53.3 × 38.7 cm and the non-segmented crystal size is 59.1 × 44.5 cm. There are 59 (bialkali high-efficiency box-type dynodes) photomultiplier tubes (PMT) in total. 53 PMTs have a diameter of 3 inches while the remaining have a diameter of 2 inches. The E.CAM's motorized patient bed has low attenuation characteristics and the close proximity of the detector to the patient optimizes the study resolution. The ECG connector and power outlet are located at the base of the patient bed where an external ECG monitor is connected.

The default data acquisition matrix is 64 × 64 and the sampling size is 4.8 mm/pixel. The supported emission isotopes are <sup>99m</sup>Tc and <sup>201</sup>Tl. The acquisition type can be either 180° SPECT or Gated SPECT.

### 5.2.2 Cardiac Static Phantom Study

SPECT and PET studies were performed using a commercially available elliptical lung-spine body phantom (216 mm wide and 186 mm thick) with simulated bone/spine and lung, and cardiac insert (model ECT/LUNG/P; Data Spectrum Corporation (DSC), NC, USA), as shown below (Figure 27). The lung inserts were filled with Styrofoam beads to simulate lung tissue density. The body phantom simulates anatomical structures and radioactivity distributions in upper torso of human. The main applications of this phantom model are:

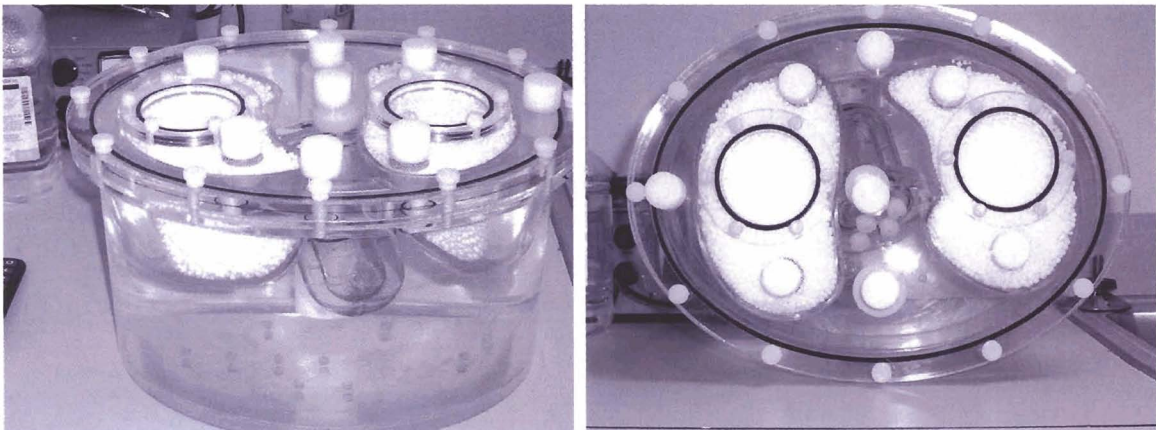
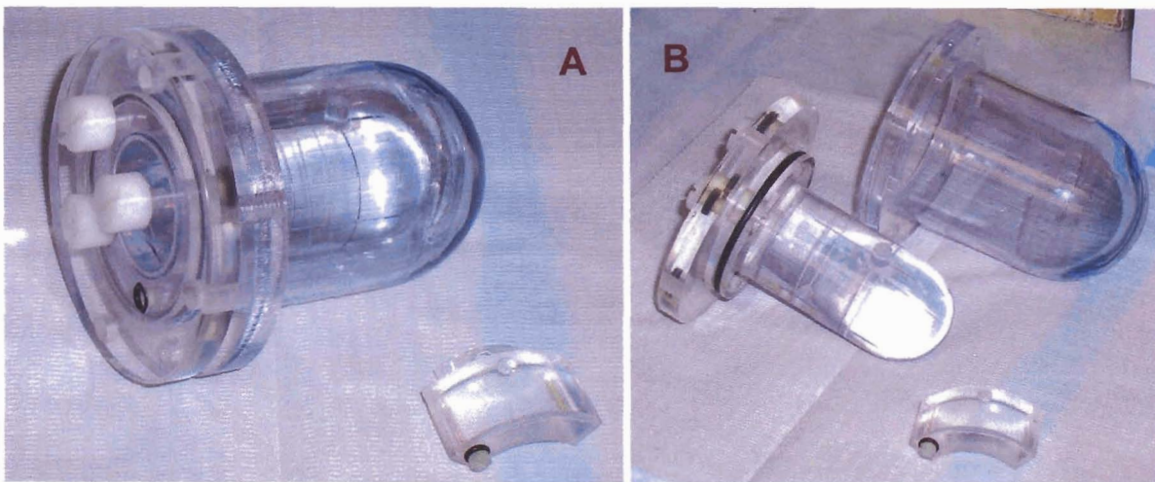


Figure 27. Anterior and upper views of elliptical lung-spine body phantom used in this study. Phantom consists of various components such as simulated lungs, spine, and heart.

- a) Evaluation of acquisition and reconstruction methods for cardiac studies and,
- b) Evaluation of non-uniform attenuation and scatter compensation methods.

The Cardiac Insert (model: ECT/CAR/I; Spectrum Corporation (DSC), NC, USA) consisted of left ventricle and the myocardium, as shown in Figure 15. It simulates normal and abnormal myocardial uptake and radioactivity in the left ventricular chamber. Fillable inserts can be used to simulate transmural and non-transmural cold and hot abnormalities.

In this particular study one defect/fillable insert was present (Figure 28). The volume of the fillable insert was 5.54 mL. The fillable insert was filled with water to match the density of the rest of the phantom. The defect area represented a myocardial perfusion defect, whereas the area without defect represented well perfused myocardium. The volume of the simulated left ventricular myocardium was 110 mL.  $^{18}\text{F}$  solution, to simulate PET clinical studies using  $^{18}\text{F}$  FDG, and  $^{124}\text{I}$ , were instilled into the left ventricular myocardium ( $\sim 1.3$  mCi) and chest ( $\sim 1$  mCi).  $^{99\text{m}}\text{Tc}$  solution, to simulate SPECT clinical studies, was administered into the left ventricular myocardium (0.5 mCi) and chest (1 mCi). A single plastic insert, which was 5% of the myocardium, was used to simulate transmural myocardial perfusion defect.



**Figure 28. A. Cardiac insert with fillable defect insert, B. Cardiac insert components (top to bottom): Myocardium, LV, and Cardiac Defect Fillable Insert.**

Data were acquired twice with each radioisotope, once with the fillable defect insert inside the myocardium and once without the defect in order to estimate and compare the true and measured defect sizes.

### 5.2.2.1 SPECT Phantom Data Acquisition (Non-Gated)

The LV was filled with water and sealed tightly after determining that no air bubbles were left in the chamber. The defect, filled with water, is attached to the LV before inserting it into the water-filled myocardium chamber. A dose of 0.5 mCi was infused in to the myocardium. 20 mL saline solution was used to flush out any dose left inside the syringe and the myocardium was immediately sealed. The cardiac insert was shaken well to evenly distribute the radioisotope inside the myocardium. The cardiac insert was attached to the elliptical phantom's lid. After filling the elliptical tub (chest) with water, the lid (attached with the spine, lungs and cardiac insert) was tightly shut. A dose of 1 mCi  $^{99m}\text{Tc}$  was injected into the tub through a re-sealable opening on top of the lid. The dose was flushed with 20 mL saline solution and the tub was checked for air pockets which were promptly removed to provide more accurate results. After resealing the lid opening, the whole phantom was shaken thoroughly for 1 minute to evenly distribute the radioisotope inside. Images were recorded over 180° from 90° right anterior oblique to 90° left posterior oblique in 32 images/head (total of 64 images) with an acquisition time of 20 seconds per projection (Figure 29).



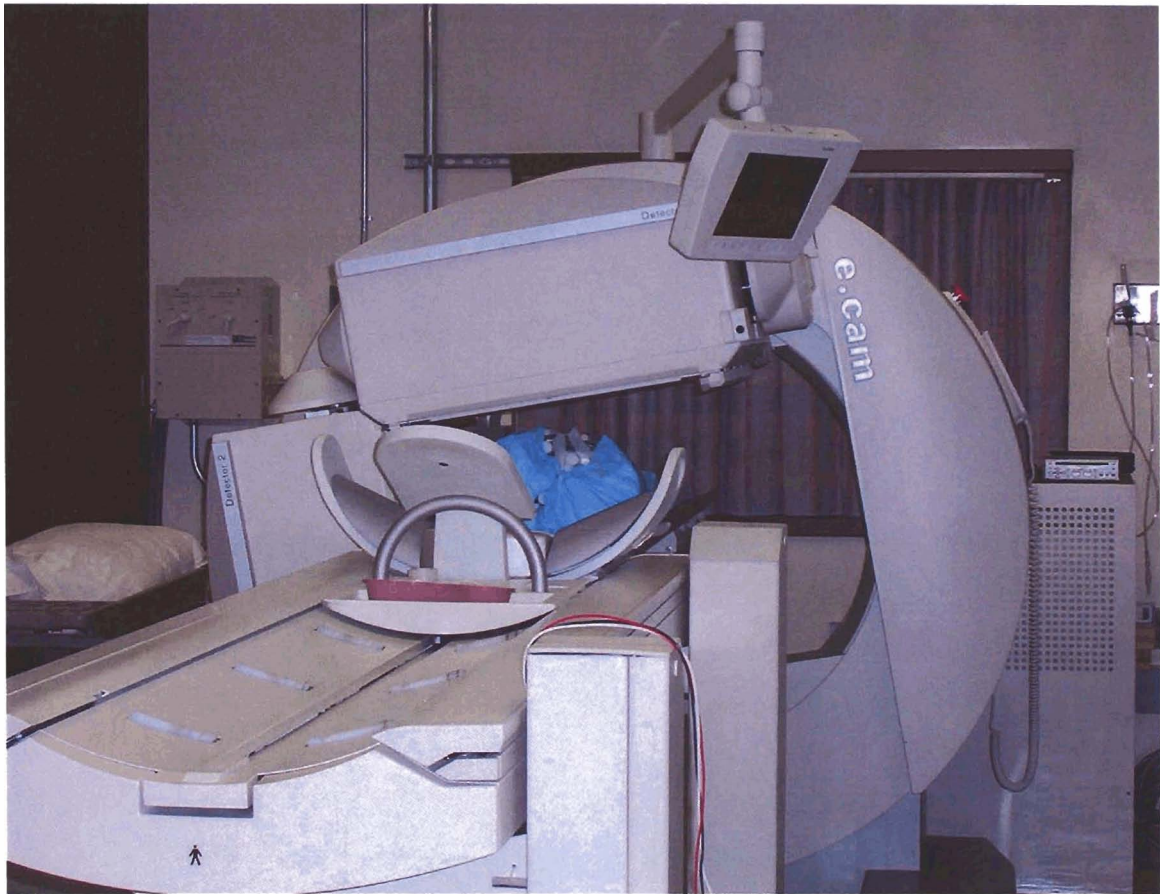


**Figure 29. Double-Headed Siemens Gamma Camera, E.Cam, during the Non-Gated  $Tc^{99m}$  Cardiac Phantom study.**

The acquired images were automatically transferred to the esoftp (Siemens) Windows XP PC via the network for data processing. The images were initially reconstructed using a Butterworth filter with a cut-off frequency of 0.55 and an order of 7 which is the standard clinical protocol for VCUHS. The image data matrix was  $64 \times 64$ , with a pixel size of 6.59 mm and a slice thickness of 6.59 mm. No scatter or attenuation correction was performed. Similarly, data was acquired without the 5% defect to calculate the measured %defect of the LV. The data-acquisition-procedure including the infused doses was similar to those for the phantom study with defect.

### 5.2.2.2 PET Data Acquisition (Non-Gated)

The study was similar to the above-mentioned SPECT study, as far as the cardiac phantom preparation procedures were concerned. The myocardium was injected with 1.289 mCi of  $^{18}\text{F}$  and the chest received a 1 mCi dose. The infused dose was an average of all the activity infused in actual patients. After the phantom was positioned in the scanner, a CT scan (transmission scan for attenuation correction) was performed on the phantom for 120 s. Then static emission data were acquired for 600 s. The acquired PET data were initially processed on an Octane workstation (Silicon Graphics, Mountain View, CA). Images were reconstructed using OSEM iterative method (subsets = 28, iterations = 2). The FOV was set to 500 mm. The image data matrix was  $128 \times 128$ ; with a pixel size of 3.91 mm and a slice thickness of 3.91 mm. Attenuation correction was performed during image reconstruction using a low energy transmission CT acquired in the same imaging session as the  $^{82}\text{Rb}$  PET emission data. Then the data were transferred to the Siemens' ESOFTE PC to determine the filtering parameters. A second  $^{18}\text{F}$  study was done two days later without the defect.

The above mentioned PET (non-gated) study procedure was repeated with  $^{124}\text{I}$  instead of  $^{18}\text{F}$ .  $^{124}\text{I}$  has a rather extended half-life (4.18 days). So the  $^{124}\text{I}$  no-defect study was performed after a gap of 10 days, to allow sufficient time for decay prior to refilling the phantom. The acquired data, like the  $^{18}\text{F}$ -FDG data, were sent to the Siemens machine through the network to determine the optimal filtering parameters.

### 5.2.3 Data Analysis

Both SPECT and eventually PET data were transferred to the Siemens machine to determine the filtering parameters. The QPS software on Siemens machine was developed to process and interpret  $^{99m}\text{Tc}$  SPECT data and compare the patient data to an existing  $^{99m}\text{Tc}$  sestamibi database. So, the SPECT data were first processed according to the standard protocol at VCUHS (Butterworth filter: Cut-off = .55 cycles/pixel, Order = 7). The data were reformatted and masked in short axis. A code was developed in IDL 6.1 to read the SPECT/PET data (with and without defect) and quantify the defect size at various cutoff thresholds ranging from 5% to 95% of peak activity with 5% increments. The true defect size used for the phantom study was 5%. The measured percent defect size by SPECT or PET was then determined through the IDL code using this formula:

$$\text{Measured Defect Size (\%)} = \frac{(VnD - VD)}{VnD} \times 100$$

$VnD$  = Volume with No Defect

$VD$  = Volume with Defect

Initially, the SPECT phantom data were processed through IDL 6.1. It was observed that the true defect size (5%) was closest to the measured defect size (5.22%) at a 45% of the maximum pixel value threshold.

So, the next goal was to determine the optimal filtering parameters for the  $^{18}\text{F}$  and  $^{124}\text{I}$  PET data which resulted in the measured defect size equivalent to the true defect size, keeping the 0.45 threshold of maximum pixel value constant. For this purpose, Butterworth filter with cut-offs ranging from .10 to .90 were applied in increments of .10 with the order

varying from 5 to 7. The volume and defect sizes were subject to change depending on the level of smoothing/filtering applied to the data. The PET data were filtered on the Siemens PC and then exported in DICOM format for calculation of percent defect size.

#### **5.2.4 REGION\_GROW Procedure in IDL**

The REGION\_GROW function performs region growing for a given region within an N-dimensional array by finding all pixels within the image array that are connected neighbors to the region pixels and that fall within provided constraints. The constraints are specified as a threshold range (a minimum and maximum pixel value). When the threshold is used, the region is grown to include all connected neighboring pixels that fall within the given threshold range.

However, REGION\_GROW function does not work efficiently in finding pixels within the image array that are not connected neighbors to the region pixels but that fall within provided constraints. This limitation leads to underestimation of defect sizes in IDL code. So we used the technique of masking instead of REGION\_GROW function. Masks are used to isolate specific features. A mask is a binary image, made by using relational operators. A binary mask is multiplied by the original image to omit specific areas. We used logical operations to make masks which masked out every pixel within the image array that did not fall within the specified threshold range regardless of whether the neighboring pixels were connected with each other or not. This operation allowed us to calculate the volumes of LV with and without defect accurately, and their difference provided us with the percent defect size at any specified threshold of the maximum pixel.

### **5.2.5 Maximum Pixel Value Threshold of an Image in IDL**

Thresholding is an image processing technique for converting a grayscale or color image to a binary image based upon a threshold value. If a pixel in the image has an intensity value less than the threshold value, the corresponding pixel in the resultant image is set to black. Otherwise, if the pixel intensity value is greater than or equal to the threshold intensity, the resulting pixel is set to white. Thus, creating a binary image, or mask with only 2 colors, black (0) and white (255). Image thresholding is very useful for keeping the significant part of an image and getting rid of the unimportant part or noise. This holds true under the assumption that a reasonable threshold value is chosen. Thresholding is the most common method of segmenting images into particle regions and background regions. A typical processing procedure would start with filtering or other enhancements to sharpen the boundaries between objects and their background. Then, the objects are separated from the background using thresholding.

In the IDL code (appendix D) developed to estimate the %defect size of the cardiac phantom, we used the thresholding technique to programmatically trace region outlines over pixels in the myocardium which fell in the specified range by creating binary masks. There was an upper limit and lower limit value used to implement thresholding. The maximum pixel value or the upper limit was calculated by determining the maximum pixel value in each DICOM image and thereby determining the largest pixel value amongst all the images. The lower limit was the percentage of maximum pixel value, which is manually specified. The threshold in our program was the percentage of set pixels (which

satisfied the range eligibility criteria) that must be present in a "block" of the original image to set the pixels of the block in the output image.

### 5.2.6 Butterworth Filter

The flexibility and ease of design of Butterworth filters have made them the filters of choice in most nuclear medicine procedures<sup>40, 76</sup>. Butterworth filter has a low frequency plateau which passes low frequencies unaltered but progressively attenuates higher frequencies. As well as a cut-off, it has an order which controls the slope of the transition. This defines how quickly the plateau changes to cut-off, the slope increasing as the order increases. Although a higher order produces a higher spatial resolution images, its effect is much less severe than the cut-off<sup>40, 41, 77</sup>. It is due to these characteristics that we chose to apply Butterworth filters to smooth the PET images in this study.

### 5.2.7 Statistical Analysis

Data are presented as mean value  $\pm$  1SD. Linear regression analysis and determination of the standard error of estimation (SEE) were used to compare the data. Paired Student *t* test was used to determine significant difference, defined as  $P < 0.05$ .

## 5.3 Results

A defect size vs. Butterworth filter cutoff graph (Figure 30) was plotted in order to determine the optimal filter cutoff value at 45% maximum pixel threshold value where the measured defect size mostly closely matched the true defect size. According to the graph, it was determined that the optimal filtering/smoothing parameter for <sup>124</sup>I PET data was Butterworth filter (cut-off = 0.80 cycles/pixel, order = 5), which resulted in a measured defect size of 5.46% (true defect size 5%). The <sup>18</sup>F PET data were analyzed using the same

approach, with filtering/smoothing parameters at Butterworth filter, cut-off = 0.70 cycles/pixel, order = 5 resulting in a measured defect size of 5.57%.

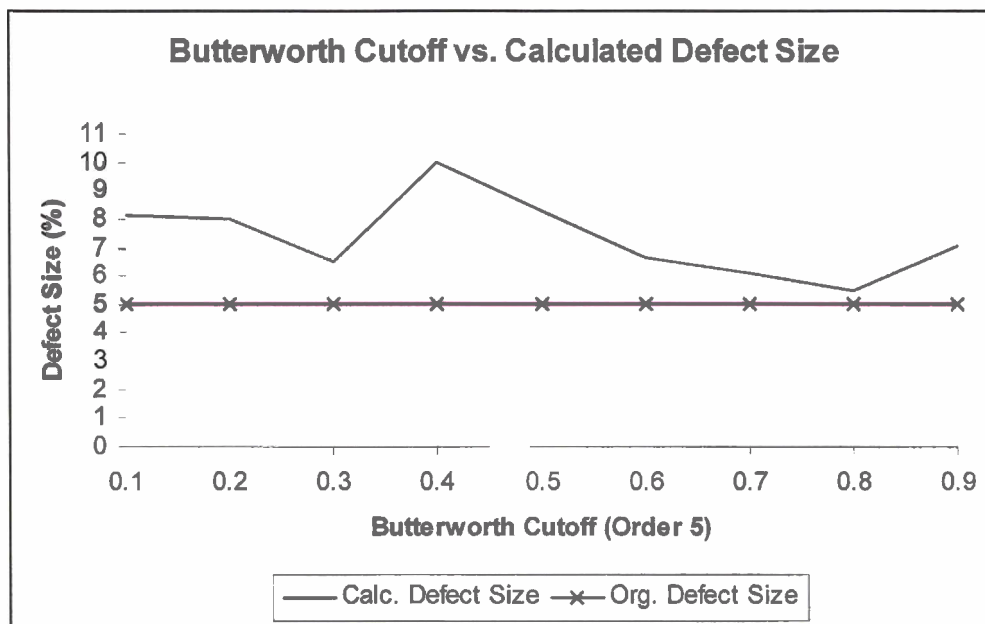


Figure 30. I-124 Static Cardiac Phantom plot (Butterworth cutoff vs. defect size)

The calculated  $^{124}\text{I}$  parameters were applied to the  $^{82}\text{Rb}$  patient data to determine the changes, if any. Table 5.1 lists a comparison of the percent change in defect size between rest and post Persantine images in patients, pre- and post- application of the new filtering parameters, the results ( $\geq 5\%$  change in defect size between rest and stress being considered clinically significant) and the actual clinical interpretation.

Table 5.1: Comparison of  $^{82}\text{Rb}$  Patient Defect Size at 45% Threshold before and after application of Optimal Filtering Parameters (Butterworth Cut-off 0.80, Order 5)

Patient	Pre-Filtered Defect Change (%)	Post-Filtered Defect Change (%)	Defect Size Difference $\geq$ 5% (%)	Results
1	13.85	2.14	N-11.71	True Negative
2	-8.77	15.78	Y24.55	True Positive
3	-2.13	-8	N-5.87	True Negative
4	-1.62	5.8	Y7.42	True Positive
5	1.82	9.38	Y7.56	True Positive
6	23.4	23.84	Y0.44	True Positive
7	-25.42	25.48	Y50.9	True Positive
8	13.43	12.27	Y-1.16	True Positive

Patient 7 had high background activity in the pre-filtered images which were included in the region growth procedure (Appendix D) which was probably the cause of the underestimation of defect size. Upon applying the optimal filtering parameters, the data did not have the extracardiac activity and we were able to estimate the true defect size (Figure 31).

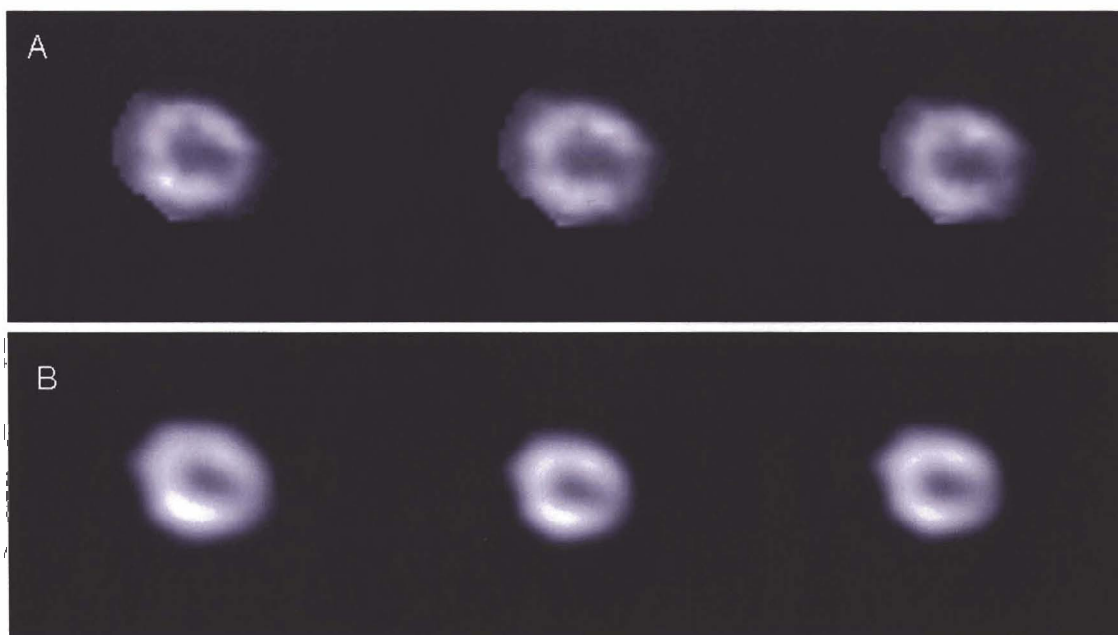


Figure 31. Comparison of Rb-82 dynamic PET data before (A) and after (B) application of optimal filtering parameters (Butterworth Filter cutoff = 0.80 cycles/pixel, order = 5)



### 5.3.1 Relationship between SPECT and PET Measurements and Percent Maximum Pixel Threshold Values

The PET and SPECT measured defect sizes, varying the percent maximum pixel value threshold from 30% to 75% for both types of imaging, did not have a positive linear relationship ( $r = -0.18$ ,  $P = 0.63$ ,  $SEE = 6.87$ ). The SPECT percent defect size varied greatly with % threshold values (defect size range: -12% to 9.1%). A paired t-test demonstrated that the mean defect size for the SPECT data ( $0.34 \pm 6.58$ ) was significantly lower ( $t = 2.21$ ,  $df = 10$ ,  $P < 0.05$ ) than the mean defect size for the PET data ( $5.71 \pm 3.00$ ) which demonstrates the underestimation of defect size by SPECT at lower cutoffs.

Table 5.2: Comparison of  $^{124}\text{I}$  (Butterworth Cut-off 0.80, Order 5) and  $^{99\text{m}}\text{Tc}$  (Butterworth Cut-off 0.55, Order 7) defect sizes at thresholds ranging from 30% to 75% after application of respective optimal filtering parameter

Threshold (%)	$^{99\text{m}}\text{Tc}$ SPECT Defect Size (%)	$^{124}\text{I}$ PET Defect Size (%)
30	1.72	-0.46
35	0.68	1.96
40	1.5	4.78
45	5.3	5.57
50	9.1	6.35
55	6.5	6.94
60	2.29	8.69
65	-3.18	9.46
70	-8.23	6.98
75	-12.2	6.87

## 5.4 Discussion

The study directly compared  $^{99\text{m}}\text{Tc}$  SPECT with  $^{18}\text{F}$ -FDG and  $^{124}\text{I}$  PET for the estimation of myocardial defect size using a cardiac phantom with a simulated myocardial perfusion defect. The major findings were, first, that the measured SPECT defect size varied greatly (table 5.2) depending on the thresholds used to define a defect, whereas PET

defect size was relatively constant over the range of cutoffs tested<sup>7</sup>; and second, that the SPECT and PET measurements nevertheless closely correlated with the true defect size if appropriate threshold of maximum pixel value and optimal filtering parameters are applied.

The hardware and software used in the acquisition and analysis of <sup>82</sup>Rb PET data is different than that of commonly used SPECT perfusion agents. <sup>82</sup>Rb PET images can have relatively low myocardial to background activity values, and suffer from low count statistics. These differences can result in an image that is not necessarily immediately representative of the underlying biological tracer distribution. We showed that by applying a tracer specific standardized filtering percent change in defect size can be accurately measured, for <sup>99m</sup>Tc, <sup>18</sup>F, and <sup>124</sup>I (a high energy positron emitter surrogate for <sup>82</sup>Rb).

The considerable change in SPECT measurements observed in this study when percent thresholds were changed may at least partially be explained by lack of attenuation and scatter correction. The underestimation of defect size by SPECT at low thresholds, likely stems from lack of scatter correction. This lack increases background activity on the image<sup>7, 78</sup> and thus reduces image contrast. In contrast to SPECT measurement, PET measurement showed excellent correlation with wide range of thresholds when the optimal filtering parameters were applied to the data, indicating that, PET can accurately quantify defect size. However, the SPECT and PET measurements closely correlated with the true defect size if appropriate threshold cutoffs and optimal filtering parameters are applied.

<sup>99m</sup>Tc SPECT is widely used in myocardial perfusion imaging, as it offers the advantages of higher photon energy and a higher injectable dose compared with <sup>201</sup>Tl. Since <sup>99m</sup>Tc SPECT is considered a gold standard for myocardial perfusion imaging, it is

safe to assume that the imaging quality falls in the satisfactory range. Smoothing the  $^{82}\text{Rb}$  PET data compromises the advantage of higher image resolution/quality over  $^{99\text{m}}\text{Tc}$  SPECT data. However,  $^{82}\text{Rb}$  PET still has the advantage of attenuation correction which results in much more accurate clinical diagnosis by reducing the number of false-positive SPECT scans.

The results of the present study raise several issues that need to be considered, foremost among them the limitations and clinical relevance of the study. The choice of phantom may affect the outcome of the filter cutoff study. Patient anatomy, as well as defect size and extent, vary considerably in a clinical environment and affect detectability<sup>79</sup>. Recalling that a filter cutoff value of 0.80 cycles/pixel was superior to 0.10, 0.20, or 0.90 cycles/pixel (table 5.1), detectability was higher for filter cutoff frequency values towards the end of the range studied for the PET data. At lower filter cutoff frequency values, the images were smooth and blurry, making regions of higher or lower intensity more difficult to detect and making the defect sizes vary inconsistently.

A previous study indicated that the optimal filter cutoff frequency was dependent on the size and extent of the defect<sup>80</sup>. In a clinical setting, filter cutoff values are in the range of 0.55 cycles/pixel for the SPECT data, which is significantly lower than the optimal value found by the current study for the PET data. Since the simulated defects were small and few in number, the question remains as to whether lower filter cutoff values provide greater detectability in a clinical situation. The answer requires clinical or phantom studies that include a range of defect sizes and clinically realistic noise levels.

## 5.5 Conclusion

An optimal filter cutoff frequency was found for the PET data within the range of values studied, and this frequency was higher than the clinical norm for SPECT data. The optimal cutoff may depend on defect size, patient variability, and noise level. When assessing myocardial defect size, physical properties need to be taken into consideration, particularly when comparing images obtained using different nuclides (i.e.  $^{82}\text{Rb}$  or  $^{99\text{m}}\text{Tc}$  agent perfusion and  $^{18}\text{F}$  FDG viability).

## **Literature Cited**

### Literature Cited

1. Go RT, Marwick TH, MacIntyre WJ, Saha GB, Neumann DR, Underwood DA, et al. A prospective comparison of rubidium-82 PET and thallium-201 SPECT myocardial perfusion imaging utilizing a single dipyridamole stress in the diagnosis of coronary artery disease. *J Nucl Med* 1990;31(12):1899-1905.
2. Stewart R, Schwaiger M, Molina E, Popma J, Gacioch G, Kalus M, et al. Comparison of rubidium-82 positron emission tomography and thallium-201 SPECT imaging for detection of coronary artery disease. *The American Journal of Cardiology* 1991;67(16):1303-1310.
3. Pagnanelli RA, Hanson MW, Turkington T, Coleman RE, Borges-Neto S. Gated <sup>99m</sup>Tc-Tetrofosmin and <sup>18</sup>F-FDG Studies: A Comparison of Single-Acquisition and Separate-Acquisition Protocols. *J Nucl Med Technol* 2002;30(4):175-178.
4. Manrique A, Faraggi M, Vera P, Vilain D, Lebtahi R, Cribier A, et al. <sup>201</sup>Tl and <sup>99m</sup>Tc-MIBI gated SPECT in patients with large perfusion defects and left ventricular dysfunction: comparison with equilibrium radionuclide angiography. *J Nucl Med* 1999;40(5):805-809.
5. Vera P, Manrique A, Pontvianne V, Hitzel A, Koning R, Cribier A. Thallium-gated SPECT in patients with major myocardial infarction: effect of filtering and zooming in comparison with equilibrium radionuclide imaging and left ventriculography. *J Nucl Med* 1999;40(4):513-521.
6. Brogssitter C, Gruning T, Weise R, Wielepp P, Lindner O, Korfer R, et al. <sup>18</sup>F-FDG PET for Detecting Myocardial Viability: Validation of 3D Data Acquisition. *J Nucl Med* 2005;46(1):19-24.
7. Matsunari I, Yoneyama T, Kanayama S, Matsudaira M, Nakajima K, Taki J, et al. Phantom Studies for Estimation of Defect Size on Cardiac <sup>18</sup>F SPECT and PET: Implications for Myocardial Viability Assessment. *J Nucl Med* 2001;42(10):1579-1585.
8. Gibbons RJ. IMAGING TECHNIQUES: Myocardial perfusion imaging. *Heart* 2000;83(3):355-360.
9. Machac J, Taillefer R, Bateman T, al. e. Program and abstracts of the Society of Nuclear Medicine 48th Annual Meeting. In: 48th Annual Meeting of the Society of Nuclear Medicine; 2001 June 23, 2001; Toronto; 2001.
10. Gould KL. PET perfusion imaging and nuclear cardiology. *J Nucl Med* 1991;32(4):579-606.

11. Machac J. Cardiac positron emission tomography imaging. *Seminars in Nuclear Medicine* 2005;35(1):17.
12. Positron Emission Tomography: Procedure Code 78810. Health Care Finance Administration National Policy 1995.
13. Yoshida K, Mullani N, Gould KL. Coronary flow and flow reserve by PET simplified for clinical applications using rubidium-82 or nitrogen-13-ammonia. *J Nucl Med* 1996;37(10):1701-1712.
14. Jadvar H, Strauss HW, Segall GM. SPECT and PET in the Evaluation of Coronary Artery Disease. *Radiographics* 1999;19(4):915-926.
15. Phelps ME, Hoffman EJ, Huang SC, Ter-Pogossian MM. Effect of positron range on spatial resolution. *J Nucl Med* 1975;16:649-652.
16. Links J. Physics and instrumentation of positron emission tomography. In: Frost JJ, Wagner HN, eds. *Quantitative imaging: neuroreceptors, neurotransmitters, and enzymes*. New York. 1990:37-50.
17. Jaszczak RJ. SPECT: state-of-the-art scanners and reconstruction strategies. In: Diksic M, Reba RC, editors. *Radiopharmaceuticals and brain pathology studied with PET and SPECT*. Boca Raton: CRC Press; 1991. p. 93-118.
18. Budinger T. Physical attributes of single-photon tomography. *J Nucl Med* 1980;21:579-592.
19. Bartlett ML, Bacharach SL, Voipio-Pulkki LM, Dilsizian V. Artifactual inhomogeneities in myocardial PET and SPECT scans in normal subjects. *J Nucl Med* 1995;36(2):188-195.
20. Hendel R, Berman D, Cullom S, et al. Multicenter clinical trial to evaluate the efficacy of correction for photon attenuation and scatter in SPECT myocardial perfusion imaging. *Circulation* 1999;99:2742-2749.
21. Links J, Becker L, Rigo P, et al. Combined corrections for attenuation, depth-dependent blur, and motion in cardiac SPECT: A multicenter trial. *J Nucl Cardiol* 2000;7:414-425.
22. DePuey EG, Garcia EV. Optimal specificity of thallium-201 SPECT through recognition of imaging artifacts. *J Nucl Med* 1989;30(4):441-449.
23. DePuey EG, 3rd. How to detect and avoid myocardial perfusion SPECT artifacts. *J Nucl Med* 1994;35(4):699-702.
24. Wackers F. Artifacts in planar and SPCT myocardial perfusion imaging. *Am J Cardiac Imaging* 1992;6:42-58.
25. Wackers FJ. Attenuation correction, or the emperor's new clothes? *J Nucl Med* 1999;40(8):1310-1312.
26. Knesaurek K, King MA, Glick SJ, Penney BC. Investigation of causes of geometric distortion in 180 degrees and 360 degrees angular sampling in SPECT. *J Nucl Med* 1989;30(10):1666-1675.
27. Go RT, MacIntyre WJ, Houser TS, Pantoja M, O'Donnell JK, Feiglin DH, et al. Clinical evaluation of 360 degrees and 180 degrees data sampling techniques for transaxial SPECT thallium-201 myocardial perfusion imaging. *J Nucl Med* 1985;26(7):695-706.

28. MacIntyre WJ, Go RT, King JL, Cook SA, Neumann DR, Saha GB, et al. Clinical outcome of cardiac patients with negative thallium-201 SPECT and positive rubidium-82 PET myocardial perfusion imaging. *J Nucl Med* 1993;34(3):400-404.
29. Patterson RE, Eisner RL, Horowitz SF. Comparison of Cost-Effectiveness and Utility of Exercise ECG, Single Photon Emission Computed Tomography, Positron Emission Tomography, and Coronary Angiography for Diagnosis of Coronary Artery Disease. *Circulation* 1995;91(1):54-65.
30. Yamashita K, Tamaki N, Yonekura Y, Ohtani H, Saji H, Mukai T, et al. Quantitative analysis of regional wall motion by gated myocardial positron emission tomography: validation and comparison with left ventriculography. *J Nucl Med* 1989;30(11):1775-1786.
31. Stewart RE, Schwaiger M, Molina E, Popma J, Gacioch GM, Kalus M, et al. Comparison of rubidium-82 positron emission tomography and thallium-201 SPECT imaging for detection of coronary artery disease. *Am J Cardiol* 1991;67(16):1303.
32. Tamaki N, Yonekura Y, Senda M, Yamashita K, Koide H, Saji H, et al. Value and limitation of stress thallium-201 single photon emission computed tomography: comparison with nitrogen-13 ammonia positron tomography. *J Nucl Med* 1988;29(7):1181-1188.
33. Garza D, Tosh AV, Roberti R, Dalal P, Reimers C, Ongseng F, et al. Detection of coronary collaterals using dipyridamole PET myocardial perfusion imaging with rubidium-82. *J Nucl Med* 1997;38(1):39-43.
34. Cherry SR, Sorenson JA, Phelps ME. *Physics in Nuclear Medicine*, 3rd ed. In: *Physics in Nuclear Medicine*, 3rd ed. 3 ed. Philadelphia: Saunders/Elsevier Science; 2003.
35. Turkington TG. Introduction to PET Instrumentation. *J Nucl Med Technol* 2001;29(1):4-11.
36. Kalman S, Turkington T. Introduction to PET Instrumentation. *J Nucl Med Technol* 2002;30(2):63-.
37. Phelps M, Mazziotta J, Schelbert H. In: *Positron emission tomography and autoradiography - principles and applications for the brain and heart*: Raven Press; 1986.
38. Casey M. *An Analysis of Counting Losses in Positron Emission Tomography*. Knoxville: University of Tennessee; 1992.
39. Bailey DL. Transmission scanning in emission tomography. *European Journal of Nuclear Medicine and Molecular Imaging* 1998;25(7):774 - 787.
40. Hamilton D. Factors Determining Image Quality and Affecting Lesion Detectability. In: *Diagnostic Nuclear Medicine: A Physics Perspective.*: Springer-Verlag; 2004. p. 295 - 300.
41. Hansen C. Digital image processing for clinicians, part 2:filtering. *Journal of Nuclear Cardiology* 2002;9:429-437.
42. Taylor D. Filter Choice for reconstruction tomography. *Nucl Med Commun* 1994;15:857-859.



43. DePuey EG, Garcia EV. Updated imaging guidelines for nuclear cardiology procedures, part 1. *Journal of Nuclear Cardiology* 2001;8:G1-G58.
44. Lodge MA, Braess H, Mahmoud F, Suh J, Englar N, Geysler-Stoops S, et al. Developments in Nuclear Cardiology: Transition from Single Photon Emission Computed Tomography to Positron Emission Tomography/Computed Tomography. *The Journal of Invasive Cardiology* 2005;17(9):491 - 496.
45. Hendel R. Attenuation correction: Eternal dilemma or real improvement? *Q J Nucl Med Mol Imaging* 2005;49:30-42.
46. COSTA DC, VISVIKIS D, CROSDALE I, PIGDEN I, TOWNSEND C, BOMANJI J, et al. Positron emission and computed X-ray tomography: a coming together. *Nuclear Medicine Communications* 2003:351-358.
47. Fleming JS. A technique for using CT images in attenuation correction and quantification in SPECT. *Nucl Med Commun* 1989;10:83-97.
48. Kamel E, Hany TF, Burger C, al. e. CT vs 68Ge attenuation correction in a combined PET/CT system: evaluation of the effect of lowering the CT tube current. *Eur J Nucl Med* 2002;29:346-350.
49. Degrado TR, Turkington TG, Williams JJ, Stearns CW, Hoffman JM, Coleman RE. Performance Characteristics of a Whole-Body PET Scanner. *Journal of Nuclear Medicine* 1994;35:1398-1406.
50. Lin JW, Sciacca RR, Chou RL, Laine AF, Bergmann SR. Quantification of myocardial perfusion in human subjects using 82Rb and wavelet-based noise reduction. *J. Nucl. Med* 2001;42(2).
51. Epstein NJ, Benelfassi A, Beanlands RS, deKemp RA. A 82Rb infusion system for quantitative perfusion imaging in 3D PET. *App. Radiat. Isot* 2004.
52. Alvarez-Diez TM, deKemp RA, Beanlands RS, Vincent J. Manufacture of strontium-82/rubidium-82 generators and quality control of rubidium-82 chloride for myocardial perfusion imaging in patients using positron emission tomography. *Appl. Radiat. Isot.* 1999;50:1015-1023.
53. Yano Y. Essentials of a Rubidium-82 generator for nuclear medicine. *Appl. Radiat. Isot.* 1987;38:205-211.
54. Diagnostics B. CardioGen-82 (Rubidium Rb 82 Generator) Package Insert. In. Princeton, NJ; 2000.
55. DePuey EG. Quantitative Perfusion SPECT. In: DePuey EG, Garcia EV, Berman DS, editors. *Cardiac SPECT Imaging, Second Edition*. 2nd ed. Philadelphia: Lippincott Williams & Wilkins.; 2001. p. 61-62.
56. Thie JA. Understanding the Standardized Uptake Value, Its Methods, and Implications for Usage. *J Nucl Med* 2004;45(9):1431-1434.
57. Strauss H, Zaret B, Hurley P, Natarajan T, Pitt B. A scintiphotographic method for measuring left ventricular ejection fraction in man without cardiac catheterization. *American Journal of Cardiology* 1971;28:575-580.
58. DePuey E, Nichols K, Dobrinsky C. Left ventricular ejection fraction assessed from gated technetium-99m-sestamibi SPECT. *Journal of Nuclear Medicine* 1993;34(11):1871-1876.

59. ISIS GMD, EMMA CMD, FERNANDO BMD, DONALD PMD. Factors Affecting Left Ventricular Ejection Fraction Using Automated Quantitative Gated SPECT. *Clinical Nuclear Medicine* 2003;28(4):290-295.
60. Nichols K, DePuey E, Rozanski A. Automation of gated tomographic left ventricular ejection fraction. *Journal of Nuclear Cardiology* 1996;3:475-482.
61. Germano G, Kiat H, Kavanagh P, Moriel M, Mazzanti M, Su H, et al. Automated quantification of ejection fraction from gated myocardial perfusion SPECT. *J Nucl Med* 1995;36:2138-2147.
62. Iskandrian A, Germano G, VanDecker W, Ogilby J, Wolf N, Mintz R, et al. Validation of left ventricular volume. measurements by gated SPECT. 99m. Tc-labeled sestamibi imaging. *Journal of Nuclear Cardiology* 1998;5:574-578.
63. Schaefer WM, Lipke CSA, Standke D, Kuhl HP, Nowak B, Kaiser H-J, et al. Quantification of Left Ventricular Volumes and Ejection Fraction from Gated 99mTc-MIBI SPECT: MRI Validation and Comparison of the Emory Cardiac Tool Box with QGS and 4D-MSPECT. *J Nucl Med* 2005;46(8):1256-1263.
64. Vallejo E, Dione DP, Sinusas AJ, Wackers FJT. Assessment of left ventricular ejection fraction with quantitative gated SPECT: Accuracy and correlation with first-pass radionuclide angiography. *Journal of Nuclear Cardiology* 2000;7(5):461.
65. Yoshioka J, Hasegawa S, Yamaguchi H, Tokita N, Paul AK, Xiuli M, et al. Left ventricular volumes and ejection fraction calculated from quantitative electrocardiographic-gated 99mTc-tetrofosmin myocardial SPECT. *J Nucl Med* 1999;40(10):1693-1698.
66. Slart RHJA, Bax JJ, de Jong RM, de Boer J, Lamb HJ, Mook PH, et al. Comparison of Gated PET with MRI for Evaluation of Left Ventricular Function in Patients with Coronary Artery Disease. *J Nucl Med* 2004;45(2):176-182.
67. Proportional Technologies Inc. Frequently Asked Questions (FAQ). In. Houston; 2000.
68. Takahashi N TN, Tadamura E, Kawamoto M, Torizuka T, Yonekura Y, Okuda K, Nohara R, Sasayama S, Konishi J. Combined assessment of regional perfusion and wall motion in patients with coronary artery disease with technetium 99m tetrofosmin. *J Nucl Cardiol* 1994;1(1):29-38.
69. Germano G, Kavanagh P, Berman D. An automatic approach to the analysis, quantification and review of perfusion and function from myocardial perfusion SPECT images. *Int J Card Img* 1997;13:337-346.
70. Germano G, Kavanagh P, Chen J, Waechter P, Su H, Kiat H, et al. Operator less processing of myocardial perfusion SPECT studies. *J Nucl Med* 1995;36:2127-2132.
71. Germano G, Berman DS. On the accuracy and reproducibility of quantitative gated myocardial perfusion SPECT. *J Nucl Med* 1998;40:810-813.
72. Ford PV, Chatziioannou SN, Moore WH, Dhekne RD. Overestimation of the LVEF by Quantitative Gated SPECT in Simulated Left Ventricles. *J Nucl Med* 2001;42(3):454-459.

73. Achtert A, King MA, Dahlberg S, Hendrick P, LaCroix K, Tsui B. An Investigation of the estimation of ejection fractions and cardiac volumes by quantitative gated SPECT software package in simulated gated SPECT images. *Journal of Nuclear Cardiology* 1998;5:144-152.
74. Pretorius PH, Xia W, King MA, Tsui BM, Pan TS, Villegas BJ. Evaluation of right and left ventricular volume and ejection fraction using a mathematical cardiac torso phantom. *J Nucl Med* 1997;38(10):1528-1535.
75. Rosenthal MS, Cullom J, Hawkins W, Moore SC, Tsui BM, Yester M. Quantitative SPECT imaging: a review and recommendations by the Focus Committee of the Society of Nuclear Medicine Computer and Instrumentation Council. *J Nucl Med* 1995;36(8):1489-1513.
76. Gilland D, Tsui B, McCartney W, Perry J, Berg J. Determination of the optimum filter function for SPECT imaging. *Journal of Nuclear Medicine* 1988;29:643 - 650.
77. Germano G. Technical aspects of myocardial SPECT imaging. *Journal of Nuclear Medicine* 2001;42:1499-1507.
78. O'Connor MK, Caiati C, Christian TF, Gibbons RJ. Effects of scatter correction on the measurement of infarct size from SPECT cardiac phantom studies. *J Nucl Med* 1995;36(11):2080-2086.
79. Sankaran S, Frey EC, Gilland KL, Tsui BMW. Optimum Compensation Method and Filter Cutoff Frequency in Myocardial SPECT: A Human Observer Study. *J Nucl Med* 2002;43(3):432-438.
80. Gilland DR, Tsui BM, McCartney WH, Perry JR, Berg J. Determination of the optimum filter function for SPECT imaging. *J Nucl Med* 1988;29(5):643-650.

## APPENDIX A

### **IDL Code to Sort DICOM PET Data, Extract Image Statistics (Maximum Pixel Value) and Write to an External Text File**

This code was developed to read dynamic DICOM PET Cardiac data in order to apply various ROI vertices information and extract maximum pixel value from within the specified ROI of 3 consecutive slices where the blood pool activity was least visible. This operation allowed us to calculate the maximum pixel values of LV cavity, myocardium and lungs at all the 74 time-points (frames). This information was written to an external text file.

#### **PRO Maximum\_Pixel\_Derivation**

**; Read and sort all the reconstructed DICOM files by their instance numbers**

```
; Select one or more DICOM files, hold ctrl key while selecting multiple files
sortFile1 = DIALOG_PICKFILE( $
PATH=FILEPATH("SUBDIRECTORY=['examples','Patient','Patient 1']"), $
TITLE='Select DICOM Patient File', FILTER='*.dcm', $
GET_PATH=path, /MULTIPLE_FILES)
```

```
;Determining the number of elements in the array
n1=N_ELEMENTS(sortFile1)
```

```
sFile=STRARR(n1)
```

```
;Loop to sort the images by their instance numbers
```

```
FOR i=0, n1-1 DO BEGIN
```

```
    ; Create a clone (aImgClone.dcm) of the selected file (sfile).
    oImg=OBJ_NEW('IDLffDicomEx',path+'aImgClone.dcm', $
CLONE=sortFile1(i))
```

```
    ; Get image attributes.
```

```
    oImg-> GETPROPERTY, INSTANCE_NUMBER=instNum
```

```

; Converts a given expression to an integer type
vIN=FIX(instNum)
b=vIN-1

```

```

; Store DICOM files sorted by the instance numbers in another array
sFile(b)=sortFile1(i)

```

**ENDFOR**

```

;Total number of files stored in the array
n=N_ELEMENTS(sFile)

```

```

;number of slices
slices=35

```

```

;number of frames
f=(n/slices)

```

```

;Create a string array, vertArr, to store the ROI path information
vertArr=STRARR(15)

```

**;Storing the computer path, leading to the saved ROI vertices information (for LV cavity, upper and lower wall of myocardium, and right and left lungs) files, in a string array**

```

vertArr(0)='C:\RSNDL61\Patient ROIs\Patient_new\LVCAV_Ten_15.sav'
vertArr(1)='C:\RSNDL61\Patient ROIs\Patient_new\LVCAV_Ten_16.sav'
vertArr(2)='C:\RSNDL61\Patient ROIs\Patient_new\LVCAV_Ten_17.sav'
vertArr(3)='C:\RSNDL61\Patient ROIs\Patient_new\LVTOP_Ten_15.sav'
vertArr(4)='C:\RSNDL61\Patient ROIs\Patient_new\LVTOP_Ten_16.sav'
vertArr(5)='C:\RSNDL61\Patient ROIs\Patient_new\LVTOP_Ten_17.sav'
vertArr(6)='C:\RSNDL61\Patient ROIs\Patient_new\LVBOT_Ten_15.sav'
vertArr(7)='C:\RSNDL61\Patient ROIs\Patient_new\LVBOT_Ten_16.sav'
vertArr(8)='C:\RSNDL61\Patient ROIs\Patient_new\LVBOT_Ten_17.sav'
vertArr(9)='C:\RSNDL61\Patient ROIs\Patient_new\LLUNG_Ten_15.sav'
vertArr(10)='C:\RSNDL61\Patient ROIs\Patient_new\LLUNG_Ten_16.sav'
vertArr(11)='C:\RSNDL61\Patient ROIs\Patient_new\LLUNG_Ten_17.sav'
vertArr(12)='C:\RSNDL61\Patient ROIs\Patient_new\RLUNG_Ten_15.sav'
vertArr(13)='C:\RSNDL61\Patient ROIs\Patient_new\RLUNG_Ten_16.sav'
vertArr(14)='C:\RSNDL61\Patient ROIs\Patient_new\RLUNG_Ten_17.sav'

```

**FOR J=0, 14 DO BEGIN**

```

;Creating a double array to contain image pixel info

```

```
pixelArr= DBLARR(f)
```

```
;Create an array, orgImgArr, to contain the original images
orgImgArr=STRARR(f)
```

```
;Assign a filename to variable t
filevar=vertArr(J)
```

```
;Use FILE_BASENAME property to extract filename
base=FILE_BASENAME(filevar,'.sav')
```

```
;Use STRMID property to extract Instance Number from filename
Num=STRMID(base,10,2)
```

```
;frame/Instance number is always one less than actual number
fr=FIX(Num)-1
```

**; Loop to read the sorted DICOM files in order and verify whether each image has more than one frame**

```
FOR i=0, f-1 DO BEGIN
```

```
; Create a clone (aImgClone.dcm) of the selected file (sfile).
oImg=OBJ_NEW('IDLffDicomEx',path+'aImgClone.dcm', $
CLONE=sFile(fr+(i*slices)))
```

```
; Get image attributes.
oImg-> GETPROPERTY, ROWS=rows, COLUMNS=cols,
INSTANCE_NUMBER=instNum1
vIN1=fix(instNum1)
```

```
; Get the image data
vPixelData = oImg->GETPIXELDATA(ORDER=order, COUNT=cnt)
```

```
; Get the image dimensions info
imgDIMS=SIZE(vPixelData, /DIMENSIONS)
```

```
; Check to see if the image has multiple frames.
frameTest = oImg->QUERYVALUE('0028,0008')
IF FrameTest EQ 2 THEN BEGIN
oImg->GETPROPERTY, NUMBER_OF_FRAMES=frames
frames = frames - 1
ENDIF ELSE BEGIN
```

```

frames = 0
ENDELSE

;Restoring the roi from the binary file
RESTORE, vertArr(J)

;Creating a new object using the vertices information
roi=OBJ_NEW('IDLanROI', DATA=ROIVertices)

ROI -> GETPROPERTY, DATA = ROIdata
x = ROIdata[0,*]
y = ROIdata[1,*]

;Create a mask from the user defined ROI
roi_mask=roi->IDLanROI::computemask(DIMENSIONS=imgDIMS)

; Extracting the image statistics (maximum pixel value information per slice) from
the sorted DICOM files and writing them to an external text file

; Print area of the maximum pixel value
IMAGE_STATISTICS, vPixelData,MASK=roi_mask , MINIMUM=minPixel,
MAXIMUM = MaxPixel, MEAN = ImgAvg, STDDEV = ImgDev

;write information to an external file
outfile='Patient_out.txt'

file_exists=FILE_TEST(outfile)

IF (file_exists) THEN BEGIN
    OPENU, unit, outfile, /APPEND, /GET_LUN
ENDIF ELSE BEGIN
    OPENW, unit, outfile, /GET_LUN
ENDELSE
    PRINTF, unit, MaxPixel, ImgAvg, ImgDev, minPixel
    FREE_LUN, unit
    CLOSE, unit

;End For Loop to determine new masked images
ENDFOR

;END of FOR loop for the f times loop
ENDFOR

```

; Note: the following line allows you to run the program multiple times without having to manually delete the file.

**FILE\_DELETE**, path + 'aImgClone.dcm', /**ALLOW\_NONEXISTENT**

; Clean up references.

**OBJ\_DESTROY**,oImg

**END**



## **APPENDIX B**

### **Steps for First Pass Radionuclide Angiography Data Processing**

- The raw patient data is located, selected and loaded into the software.
- The raw data is processed using predefined setups/templates. Since this is a rest study, a rest template is selected and the processed data is viewed.
- The first step is to identify and draw a region of interest (ROI) over the left lung region making sure not to include LV or Aorta in the ROI. A histogram is generated with the computer extrapolating only data within the ROI and displaying it in an XY, histogram.
- After the histogram has been created, the Curve analysis program can be entered to perform exponential or gamma-variate calculations on the data. The sample time is changed from the default regroup factor of 25 ms to 20 ms.
- The display shows a raw curve and the updated curve beneath. It is recommended to smooth the curve. Hence, the curve is smoothed thrice or until it looks smooth and an exponential analysis is done to determine the *pulmonary mean transit time* (PMTT). The PMTT (at rest) is shown and recorded at this point. Hit Escape to return to the main menu.

- The next step is to draw an ROI over the left ventricle (LV) by choosing the best LV frame, one where the entire LV can be seen while all the activity is in the LV. Another histogram is plotted using the ROI information.
- There are 3 points (in form of green, red and yellow vertical lines) which are used to limit the histogram. The yellow vertical line is moved to the lowest valley before the LV phase. The green line is moved to a systole frame, one which can be the next frame after lung background, to select the first desired LV phase frame. The red line is used to select the last desired frame of the LV phase and this should also be a systole.
- The computer will draw in the stroke/net volume (SV) on both the End Diastolic (D) image and the End Systolic (ES) image. The net is dependent upon the ROI previously drawn and the count rates within the boundaries of the LV phase.
- The ED/ES list can be viewed at this time to determine if any peaks were missed. It is recommended that the standard deviation in the Raw EF be less than 5 and the standard deviation in the Peak-Peak interval be less than 50. The heart rate should be the same as on the monitoring equipment during the study.
- Approximately 20% to 30% of the total activity is background during the LV phase. Background can be identified with a region of interest defined immediately outside the apical perimeter of the left ventricle, quantified for each frame, and subtracted from total counts before calculation of absolute or relative volumes. Alternatively, the cycle immediately preceding the identifiable entry of isotope into the left ventricle can be selected from the time-activity curve and subtracted from

subsequent frames used to define left ventricular volume variations. Finally, a standard background subtraction constant can be determined by a variety of algorithms. It should be ascertained that the background is not over subtracted in the LV image. The background subtraction is a crucial step in the processing, since variation in the background frame can substantially alter the calculated EF, volumes and apparent wall motion. The frame used to determine the background should be the one in which the bolus appears in the LV, but should not itself show any activity in the LV and no residual activity in the right ventricle (RV). If a suitable frame is not available, background subtraction should not be taken.

- A region is manually drawn to mark the end diastole and end systole of the LV.
- The LVEF is generated and shown at this point. Hit “Escape” key to return to the main menu.
- After LV phase processing, a ROI is drawn over the right ventricle (RV) by choosing the best RV frame and a histogram is generated. This time the green line is placed at the beginning of the histogram (first frame that can be selected), the red line is placed at the frame which immediately follows the RV phase and the blue line is placed under the first identifiable heart beat in RV phase. Zero background is selected when processing the RV.
- A Prompt pops up saying: “Ventricular Processing – Do you wish the processing to pause at each significant stage in the remainder of the analysis?” Hit YES.
- Next, draw ROIs over the RV end diastole and the RV end systole. The RVEF (Right Ventricular Ejection Fraction) shows up at this point.

The results are reviewed and the snapshots of both LV and RV volume pages, systolic LV information page and the LV histogram are taken. All the four snapshots come out in one page and this sheet is reviewed by the physicians for clinical diagnosis (Figure 32).

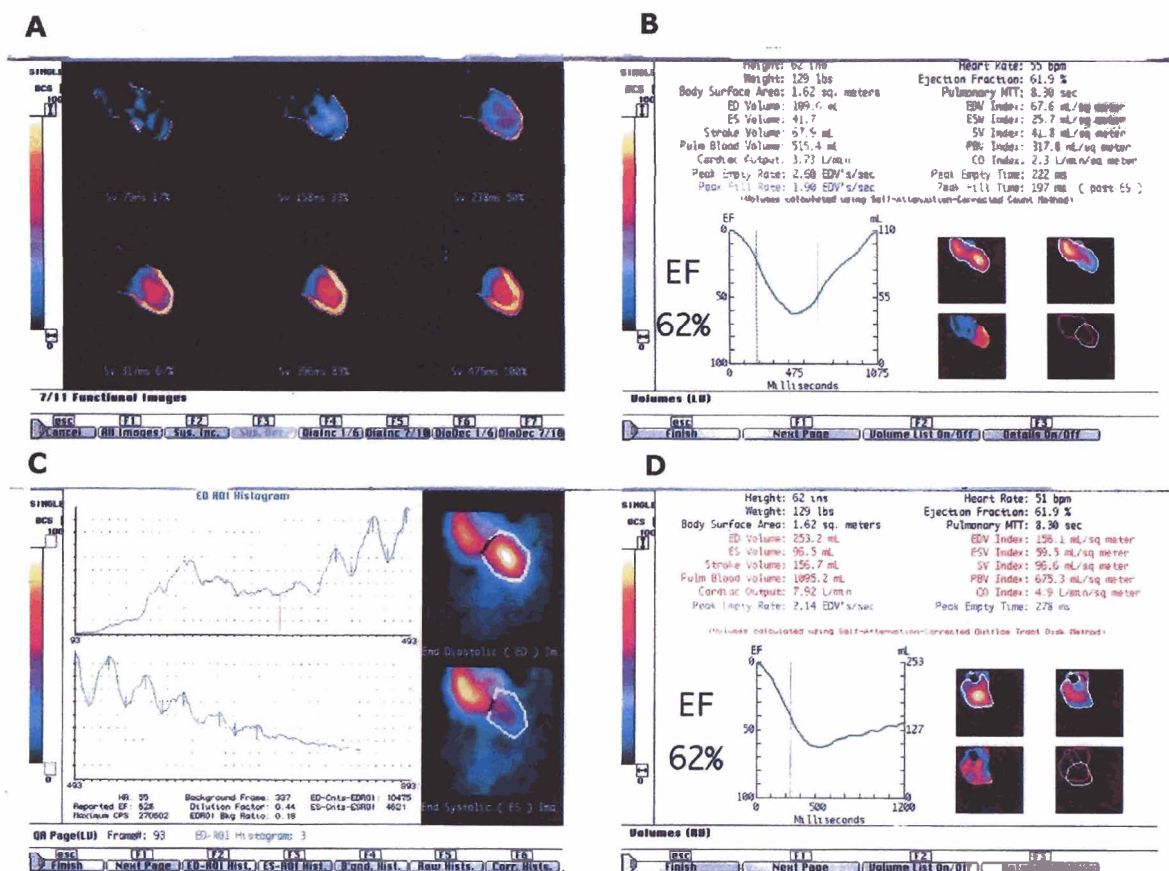
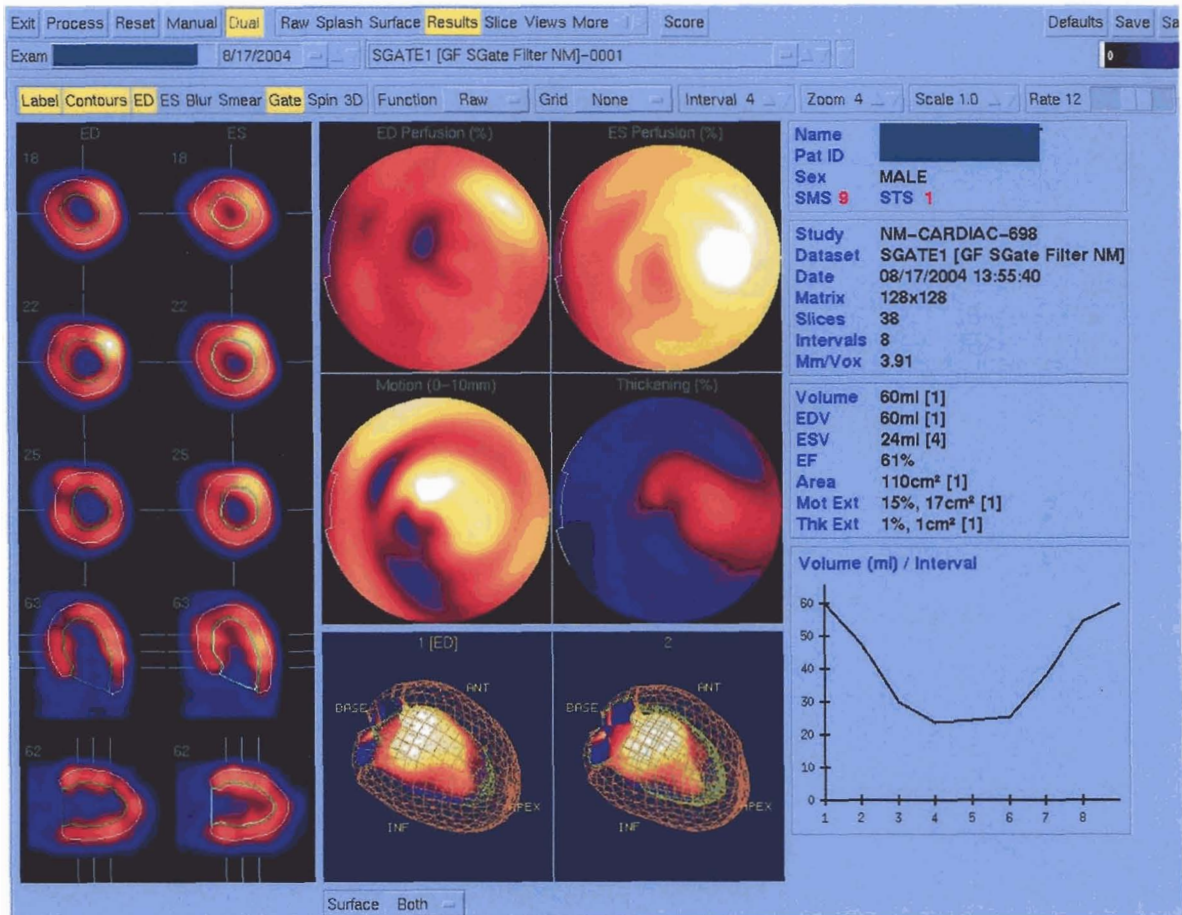


Figure 32. First Pass Radionuclide Angiography Processing Screenshot: A) Functional Images, B) LVEF, C) LV ED ROI Histogram and D) RVEF screenshots.

## APPENDIX C

### **Steps for Quantitative Gated SPECT (QGS 3.0) Data Analysis of $^{82}\text{Rb}$ Gated-PET Data for estimation of Left Ventricular Ejection Fraction**

- The gated PET data are acquired (8 bins\* with 35 frames/bin) using the GE Discovery LS scanner and stored on the Octane workstation.
- The data are reconstructed using OSEM 2D method with 28 iterations and 2 subsets. Attenuation correction via transmission scan is applied to the data during reconstruction. The reconstructed data are summed and the images are transferred via network to the ESOFTP (Siemens) machine.
- Two workflows, Cardiac Gated Processing and Cardiac Display, are used to process the gated data.
- Cardiac Gated Processing converts the rest and stress gated data from PET modality to Nuclear medicine before filtering and reorienting them. A Butterworth filter (cutoff = 0.25 cycles/pixel, order = 5) is used according to the standard protocol.
- The processed data is then analyzed using the QGS program (Figure 33) to calculate left ventricular ejection fraction (LVEF), left ventricular end-diastolic volume (LVEDV) and left ventricular end-systolic volume (LVESV).



**Figure 33. Quantitative Gated SPECT (QGS) analysis of gated Rb-82 PET data. The left ventricular ejection fraction is 61 %.**

- The automatic algorithm identifies the endocardial and epicardial contours for each of the eight sets of short axis slices in the cardiac cycle to calculate volume changes.
- The largest and the smallest left ventricular volumes correspond to the LVEDV and LVESV.

## APPENDIX D

### IDL Code to Estimate Percent Defect Size of Cardiac Phantom PET Data

This code was developed to read DICOM PET phantom LV data with and without defect in order to estimate the %defect size of the data at various %thresholds of maximum pixel. Masks are used to isolate specific features. A mask is a binary image, made by using relational operators. A binary mask is multiplied by the original image to omit specific areas. We used logical operations to make masks which masked out every pixel within the array that did not fall within the specified threshold range. This operation allowed us to calculate the volumes of LV with and without defect, and their difference provided us the %defect size at any specified threshold of the maximum pixel.

#### PRO Defect\_Size\_Estimation\_PET\_Rb82

```

;Create an 4 X 100 Double array, volArr1, to contain the
;volume info for the PET data with defect in first column
;volume info for the PET data without defect in second column
;Defect size % in the third column and
;Threshold values in the fourth column
volArr1=DBLARR(4,19)

```

#### FOR T=0, 1 DO BEGIN

```

; Select one or more DICOM files, hold ctrl key while selecting multiple files
; Select PET data with defect first and then select the PET data with no defect

```

```

sortFile = DIALOG_PICKFILE( $
PATH=FILEPATH("", SUBDIRECTORY='RB82_NO_FILTER_DATA_1015'), $
TITLE='Select DICOM Patient File', FILTER='*', $
GET_PATH=path, /MULTIPLE_FILES)

```

```

; Create a clone (aImgClone.dcm) of the selected file (sfile).
oRdImg=OBJ_NEW('IDLffDicomEx',sortFile(0))

```

```

; Check to see if the image has multiple frames.

```

```
frameTest = oRdImg->QUERYVALUE('0028,0008')
```

```
IF FrameTest EQ 2 THEN BEGIN
```

```
    oRdImg->GETPROPERTY, NUMBER_OF_FRAMES=frames
```

```
    frames = frames - 1
```

```
    n=frames+1
```

```
ENDIF ELSE BEGIN
```

```
    frames = 0
```

```
    n=frames+1
```

```
ENDELSE
```

```
FinCnt=0
```

```
;For loop to run program at various thresholds with 5 point increments
```

```
FOR U=5, 95, 5 DO Begin
```

```
    ;Setting Threshold Value
```

```
    threshold1 = DOUBLE (DOUBLE (U)/100)
```

```
    ;Creating a double array to contain image pixel info
```

```
    pixelArr= DBLARR(n)
```

```
    ;Create an array, orgImgArr, to contain the original images
```

```
    orgImgArr=STRARR(n)
```

```
;Looping 35 times
```

```
FOR i=0, frames DO BEGIN
```

```
    ; Get image attributes.
```

```
    oRdImg-> GETPROPERTY, ROWS=rows, COLUMNS=cols,;
```

```
    PIXEL_ASPECT_RATIO=par
```

```
    ; Get the image data
```

```
    vPixelData = oRdImg->GETPIXELDATA (ORDER=order, COUNT=cnt)
```

```
    ; Get the image dimensions info
```

```
    imgDIMS=SIZE(vPixelData, /DIMENSIONS)
```

```
    ; Create a mask that identifies the darkest pixels,
```

```
    ; whose values are greater than 0.
```

```
    pix=vPixelData[*,*,i]
```

```
    IMAGE_STATISTICS, pix, MINIMUM=minPixel, MAXIMUM = MaxPixel
```



```
; convert loop number to text
s=STRING(i)

;Create save filename
orgResult='orgResult'+s+'.sav'

;remove whitespaces in filename
orgImgResult=STRCOMPRESS(orgResult, /REMOVE_ALL)

;Create IDL sav file containing Original Image Result variable (sav filename)
SAVE, pix, FILENAME=orgImgResult

;Saving the Sav file to another array for easy retrieval
orgImgArr(i)=orgImgResult

;Saving maxpixel information for each image in PixelArr
pixelArr(i)=MaxPixel

;End For Loop to determine maximum of max pixels
ENDFOR

;Determining the largest pixel from the array
MaxiPixel=MAX(pixelArr)

;Dimesions info
pixelXSize=3.91
pixelYSize=3.91
pixelZSize=3.91

;Initializing 2 variables to store Total Area and individual area info
AreaSum=0
geomArea=0
Pixelsum=0

;Initializing a counter to keep track of the total
;number of slices on which region_growth was performed
Counter=0

;Determining the lower limit for RegionGrowth
LowerPixel = maxipixel * threshold1

;New Loop for region growing and finding sum of areas
FOR K=0, frames DO BEGIN
```

pixmax=pixelArr(k)

;Break loop if maximum pixel of the current slice <= lowerpixel  
**IF** (pixmax LE lowerpixel) **THEN** Continue

**RESTORE**, orgImgArr(k)

**; Applying a Threshold**

nullArr=pix **GE** lowerPixel

; Print area of the maximum pixel value

**IMAGE\_STATISTICS**, pix,**MASK**=nullArr, **COUNT**=pixcnt

; Use formulae to obtain the geometric area/volume of each region where 1 pixel =  
 3.9 x 3.9 mm.

geomArea=pixcnt \* pixelXSize \* pixelYSize \* pixelZSize  
 pixelArea=pixcnt \* pixelXSize \* pixelYSize

;Total Volume before addition with geomArea=AreaSum

;Total Area before addition with pixelsum=Pixelsum

AreaSum=AreaSum+geomArea

Pixelsum=pixelsum+pixelarea

;Total Volume after addition with geomArea=AreaSum

;Total Area after addition with pixelsum=Pixelsum

;Increment the number-of-slice tracking counter

**Counter++**

**ENDFOR**

mlConvert=AreaSum\*.001

cmConvert=PixelSum\*.01

;Print the sum of areas for each threshold

;Total Volume of grown region =AreaSum "mm cube or"mlConvert"ml

;Total area of grown region =pixelSum "mm square or",cmConvert"cm square"

;Assign the volume info to the array

volArr1(T,FinCnt)=mlConvert

;Counter increment for the Volume Array

FinCnt++

**ENDFOR**

**ENDFOR**

; Save the %defect size information to an array, volArr1

**FOR** V=0,FinCnt-1 **DO BEGIN**

    volArr1(2,V)=((volArr1(1,V)-volArr1(0,V))/(volArr1(1,V)))\*100

    volArr1(3,V)=(V+1)\*5

**ENDFOR**

; Note: the following line allows you to run the program multiple times without having to manually delete the file. You cannot duplicate an existing file when creating or cloning a DICOM file.

**FILE\_DELETE**, path + 'aImgClone.dcm', /**ALLOW\_NONEXISTENT**

;Delete the processed image data to save space

**FILE\_DELETE**, orgImgArr

; Clean up references.

**OBJ\_DESTROY**, [oRdImg]

;write information to an external text file

outfile='PET\_THRESHOLD\_Rb82\_NoFilter.TXT'

file\_exists=**FILE\_TEST**(outfile)

**IF** (file\_exists) **THEN BEGIN**

**OPENU**, unit, outfile, /**APPEND**, /**GET\_LUN**

**ENDIF ELSE BEGIN**

**OPENW**, unit, outfile, /**GET\_LUN**

**ENDELSE**

**PRINTF**, unit, volArr1

**PRINTF**, unit, "\*\*\*\*\*"

**FREE\_LUN**, unit

**CLOSE**, unit

**END**

## VITA

George N. Francis was born on June 5<sup>th</sup>, 1979 in Kottayam, India to Mr. Chirayil Varkey Francis and Mrs. Elsamma Francis. He is a citizen of India. He came to United States of America to pursue his higher education in August 1998. He received his Bachelor of Arts degree in Computer Science from Rutgers, The State University of New Jersey in May 2003. He later attended Virginia Commonwealth University in Richmond, Virginia where he obtained his Master of Science degree in Biomedical Engineering in December 2005.